Felix Wald

Asynchronous Grid Connections as Distribution Grid Interfaces: Control, Services, and Economic Viability

Energy Lab – Scientific Reports

2

Karlsruhe Institute of Technology

Asynchronous Grid Connections as Distribution Grid Interfaces: Control, Services, and Economic Viability

Zur Erlangung des akademischen Grades eines

Doktors der Ingenieurwissenschaften (Dr.-Ing.)

von der KIT-Fakultät für
Elektrotechnik und Informationstechnik
des Karlsruher Instituts für Technologie (KIT)

angenommene

DISSERTATION

von

M.Sc. Felix Wald
geb. in Stuttgart

Tag der mündlichen Prüfung:	18.03.2026
Hauptreferent:	Prof. Dr.-Ing. Giovanni De Carne
Korreferent:	Prof. Oriol Gomis-Bellmunt

Acknowledgments

I am incredibly thankful to everyone who accompanied me on my journey to completing this dissertation, including my advisors, colleagues, friends, and family. This would not have been possible without your support and encouragement.

First, I would like to express my heartfelt gratitude to my supervisor, Prof. Giovanni De Carne, who always believed in my abilities and encouraged me to explore my own ideas. Thank you for your unwavering support, dedication, and valuable guidance in shaping the direction of my research. I am also deeply grateful for your unconditional support and generosity in funding my participation in conferences and my research collaboration at the National Renewable Energy Laboratory (NREL).

Thank you to the researchers at NREL for providing me with valuable insights, specifically Barry Mather for hosting me in his group and connecting me with Amir Sajadi. Amir's support and guidance in the pursuit of economic frameworks and power system level analysis was invaluable. Special thanks to Prof. Oriol Gomis-Bellmunt for his insights on power system architectures, reviewing my dissertation and taking the time to be my co-supervisor.

None of the work would have been possible without the team at ITEP. Thanks to Christian, Dieter, Frank, and Uwe for always supporting my experimental tests. Thank you to all the colleagues, friends, and members of the RTSET group, you made the journey so much more enjoyable, in particular, Ali, Anne, Danilo, Dustin, Fargah, Honeymol, Jonghun, Karthik, Maeva, Mahshid, Malik, Massi, Michael, Nils, Nima, Sarah, Shahab, Roberto and Qiucen.

Finally, a big thank you to all my loved ones, in particular my parents for unconditionally supporting me in all my decisions and Alina for trusting me, having my back, cheering me up and celebrating the good times with me.

Karlsruhe, February 2026

Felix Wald

Kurzfassung

Die Energiewende stellt derzeit eine der größten ingenieurtechnischen Herausforderungen dar. Asynchrone Netzkopplungen—leistungselektronische Systeme, die zwei Netze koppeln und eine Regelung der übertragenen Leistung und der angeschlossenen Netze ermöglichen—sind eine vielversprechende Technologie für eine erfolgreiche Transformation des Energiesystems. Ihre Fähigkeit, den Leistungsfluss anzupassen und Netzunterstützung je nach aktuellem Netzzustand bereitzustellen, kann sie zu einem Schlüsselelement für ein widerstandsfähiges und nachhaltiges Energiesystem machen. Für eine erfolgreiche Anwendung der Technologie muss sich der Forschungsschwerpunkt der letzten Jahre jedoch vom Hardware-Design hin zu einer zuverlässigen und zweckdienlichen Regelung und Integration in das Energiesystem verlagern.

Das Hauptziel dieser Arbeit ist es, die bestehende Lücke zwischen der Bewertung leistungselektronischer Hardware und der Analyse des Energiesystems zu schließen. Um einen fundierten Hintergrund zu schaffen, werden Regelungskonzepte für asynchrone Netzkopplungen und ihr Potenzial zur Netzunterstützung analysiert. Darauf aufbauend wird ein neues Regelungskonzept vorgestellt, das *Frequency Propagation*-Konzept, welches die Frequenz des Primärnetzes nutzt, um die Regelungsziele des leistungselektronischen Systems, insbesondere den Wirkleistungsfluss, zu beeinflussen. Dieses Konzept nutzt frequenz- und spannungsabhängige Ressourcen im Verteilnetz, um deren Wirkleistungssollwerte zu steuern und Netzfrequenzstörungen zu mindern. Die Fähigkeit zur Bereitstellung von Frequenzregelungsdiensten und deren Auswirkungen auf das Energiesystem werden mittels Power Hardware-in-the-Loop experimentell validiert und bewertet. Auf Basis dieser Validierung wird eine wirtschaftliche Bewertung einer asynchronen Netzkopplung durchgeführt, die an einem Frequenzregelungsmarkt in Nordamerika teilnimmt. Die wirtschaftliche Machbarkeit wird unter Verwendung gängiger Kennzahlen für Einnahmen und zukünftigen Cashflow, die auf Langzeit-Netzsimulationen basieren und mit realen Marktdaten verknüpft sind, demonstriert.

Die vorliegende Arbeit demonstriert asynchrone Netzkopplungen, welche dynamische Netzschnittstellen und damit neue Betriebsparadigmen für nachhaltige Energiesysteme ermöglichen. Mit der Kombination aus Systemanalyse, experimenteller Validierung, und wirtschaftlicher Analyse, wird ein umfassender Rahmen für die zukünftige Forschung zu leistungselektronischen Systemen in dezentralen und asynchronen Netzarchitekturen geschaffen.

Abstract

The power system transition is currently one of the major challenges in engineering. Asynchronous grid connections—power electronics based systems that couple two grids and enable advanced control of the transferred power and connected grids—are a promising technology to enable a smooth power system transition. Their ability to adapt the power flow and offer advanced grid control features based on real-time grid conditions makes them a key enabler for a resilient and sustainable power system. However, for a successful deployment of technology the research focus of recent years on hardware design and control needs to shift toward the reliable and purposeful integration into the power system.

Bridging the existing gap between power electronic hardware assessment and power system analysis is the primary objective of this thesis. To provide a sound background, control concepts for asynchronous grid connections and their potential to be offered as grid services are analyzed. Building upon that analysis, a new control concept is proposed, the *Frequency Propagation* concept, which uses the frequency of the primary grid to influence the control objectives of the power electronic system, specifically the active power flow. This concept leverages frequency and voltage dependent resources in the distribution grid to control their active power set points and mitigate grid frequency disturbances. The capability to offer frequency response services and its power system level impact is experimentally validated and assessed using Power Hardware-in-the-Loop. Based on that validation, a case study for the economic assessment of an asynchronous grid connection participating in a frequency response market in North America is conducted. The economic viability is demonstrated using state-of-the-art metrics for revenue and future cash flow based on long-term power system simulations paired with real market data.

This work demonstrates the ability of asynchronous grid connections operating as dynamic grid interfaces enabling new operational paradigms for sustainable power systems. The combination of experimental validation, power system impact assessment, and robust economic analysis establishes a comprehensive framework for future system analysis and research on power electronic systems enabling clustered and decentralized grid architectures. Such sophisticated concepts and grid architectures can enable the resilient, flexible, and sustainable power system of the future.

Contents

Acknowledgments . . . . . **i**

Kurzfassung . . . . . **iii**

Abstract . . . . . **v**

Acronyms and Symbols . . . . . **xi**
Acronyms xi
Variables and Symbols xiii
Subscripts xiv

1 Introduction, Motivation, and Scope of Work **1**
1.1 Power System Transformation Challenges 2
1.1.1 Renewable Energy Integration and Supply Reliability 2
1.1.2 Limited Integration of New Resources 3
1.1.3 Low Inertia Power Systems 4
1.1.4 Markets and Regulatory Frameworks 5
1.2 Research Questions and Contributions 6
1.3 Scope of Work and Structure 10

2 Control of an Asynchronous Grid Connection **13**
2.1 Power Electronic Topologies to establish Asynchronous Grid Connections 14
2.1.1 The Solid-State Transformer 15
2.1.2 The Back-to-Back Converter 19
2.2 The two-level Voltage-Source Converter 20
2.2.1 The Power Electronic Topology 21
2.2.2 Modulation 23
2.3 Control Strategy for the Back-to-Back Converter 24
2.3.1 Three Phase System Modeling 24
2.3.2 Grid-following - Active Front End 26
2.3.3 Grid-forming - Virtual Synchronous Machine 33

3 Models and Testbenches to test Asynchronous Grid Connections 41
3.1 Power Electronic Modeling 41
3.1.1 Switching Modeling 41
3.1.2 Average Modeling 43
3.2 Power System Modeling 47
3.2.1 Single Machine Model 47
3.2.2 CIGRE LV Benchmark Network 50
3.3 Validation Setups 51
3.3.1 Controller Hardware-In-the-Loop Setup 51
3.3.2 1 MVA Power Hardware-in-the-Loop (PHIL) Setup at EnergyLab 55

4 Scenarios and Services enabled by Asynchronous Grid Connections . . . 63
4.1 The Asynchronous Grid Connection Scenario 63
4.1.1 Enabling Concept 64
4.1.2 Scenarios 64
4.1.3 Project - FlexNet-EkO 66
4.2 DC Connectivity for Load and Generator Integration 66
4.2.1 Enabling Concept 66
4.2.2 Scenarios 67
4.2.3 Project - LVDC Grid Interface by EATON 70
4.3 Active Power Flow Control 70
4.3.1 Enabling Concept 71
4.3.2 Services 72
4.4 Reactive Power Compensation 73
4.4.1 Enabling Concept 73
4.4.2 Services 74
4.5 Projects and Demonstrators 74

5 Asynchronous Grid Connections for Frequency Response Services 77
5.1 Frequency Response Services 77
5.1.1 Inertial Frequency Response 79
5.1.2 Primary Frequency Control 80
5.2 The Asynchronous Grid Connection for Frequency Response 81
5.2.1 Load Sensitivity 81
5.2.2 Frequency Propagation Concept 84
5.3 Open-loop Frequency Response Testing of Asynchronous Grid Connections in PHIL 86
5.3.1 Active Power Flow Control exploiting Frequency Droop in Active Resources 87
5.3.2 Active Power Flow Control exploiting Voltage Dependencies 94

5.3.3 Active Power Flow Control exploiting combined Frequency Droop and Voltage Dependencies . . . 96
5.3.4 Active Power Flow control Comparison between Frequency Droop, Voltage Dependency and the combined Method . . . 97
5.4 Closed-loop Frequency Response Testing of the Asynchronous Grid Connection in PHIL . . . 99
5.4.1 Closed-loop Frequency Response Testing exploiting Frequency Droop in Active Resources . . . 100
5.4.2 Closed-loop Frequency Response Testing exploiting Voltage Dependencies . 105
5.4.3 Closed-loop Frequency Response Testing exploiting combined Frequency Droop and Voltage Dependencies . . . 109
5.4.4 Active Power Flow Control Comparison between Frequency Droop, Voltage Dependency and the combined Method - Closed-loop . . . 111
5.5 Conclusion of the Active Power Control and Frequency Response Capability Testing . . . 113
5.5.1 Key Experimental Findings . . . 113
5.5.2 Critical Barriers and Implementation Challenges . . . 114
5.5.3 Concluding Remarks . . . 114

6 Economic Analysis of Asynchronous Grid Connections offering FFR Services . . . 117
6.1 PJM FFR Regulation Market - RegA/D . . . 118
6.1.1 PJM RegD Revenue Calculation . . . 119
6.2 Asynchronous Grid Implementation in PJM . . . 120
6.2.1 VSM Enhancement to Exploit the Frequency Droop . . . 121
6.2.2 Average RMS Model of an Asynchronous Grid Connection . . . 122
6.3 Revenue Calculation . . . 124
6.3.1 Performance Score Impact . . . 126
6.4 Economic Projection . . . 127
6.4.1 Net Present Value Calculation . . . 129
6.4.2 Internal Rate of Return Calculation . . . 130
6.4.3 Cashflow Analysis . . . 131
6.5 Conclusion and Summary of the Economic Analysis . . . 132
6.5.1 Key Technical and Economic Findings . . . 132
6.5.2 Challenges and Limitations . . . 133
6.5.3 Concluding Remarks . . . 135

7 Conclusion and Vision . . . 137
7.1 Conclusion . . . 137
7.2 Remaining Challenges . . . 138

7.3 The Vision 140

A Appendix 141
A.1 Rate of Change of Frequency (RoCoF) Calculation Methodology 141
A.1.1 Definition and Significance 141
A.1.2 Challenges in Discrete RoCoF Measurement 141
A.1.3 Sliding Window Averaging Method 142
A.1.4 Implementation Parameters 143
A.1.5 Justification and Validation 144
A.1.6 Limitations and Considerations 144
A.1.7 Summary 145

Publications 157
Journal articles 157
Conference contributions 157
Co-authored articles 158

Bibliography 159

Acronyms and Symbols

Acronyms

ACE	Area Control Error
ADC	Analog Digital Conversion
ADN	Active Distribution Network
AFE	Active Front End
aFRR	Automatic Frequency Restoration Reserve
AGC	Automatic Generation Control
ASG	Asynchronous Grid Connection
B2B	Back-to-Back Converter
BESS	Battery Energy Storage System
CHB	Cascaded H-Bridge
CHIL	Controller Hardware-in-the-Loop
CO_2	Carbon dioxide
DAB	Dual Active Bridge
DAC	Digital Analog Conversion
DER	Distributed Energy Resource
DG	Distributed Generation
ENTSO-E	European Network of Transmission System Operators for Electricity
ESS	Energy Storage System
EV	Electric Vehicle
FCR	Frequency Containment Reserve
FFR	Fast-Frequency Response
GFL	Grid-Following
GFM	Grid-Forming
HOI	Hardware of Interest

IGBT	Insulated Gate Bipolar Transistor
IRENA	International Renewable Energy Agency
IRR	Internal Rate of Return
ITM	Ideal Transformer Method
KCL	Kirchhoff's Current Law
KVL	Kirchhoff's Voltage Law
LCOE	Levelized Cost of Energy
LFT	Line-frequency Transformer
mFRR	Manual Frequency Restoration Reserve
MMC	Modular Multi-level Converter
MOI	Model of Interest
NPV	Net Present Value
PCC	Point of Common Coupling
PHIL	Power Hardware-in-the-Loop
PI	Proportional Integral
PJM	Pennsylvania New Jersey Maryland
PLL	Phase-Locked Loop
p.u.	Per Unit
PV	Photovoltaic
PWM	Pulse Width Modulation
RMS	Root-Means-Square
RoCoF	Rate of Change of Frequency
RR	Restoration Reserve
RTO	Regional Transmission Organization
SFP	Small Form-Factor Pluggable
SiC-MOSFET	Silicon Carbide MOSFET
SMM	Single Machine Model
SOI	System of Interest
SST	Solid-State Transformer
STATCOM	Static Synchronous Compensator
TSO	Transmission System Operator
VSC	Voltage-Source Converter
VSM	Virtual Synchronous Machine
VVC	Volt-Var Control

Variables and Symbols

Cf	Cash Flow
c	Cost
C	Credit
D	Damping Coefficient
f	Frequency
τ	Theoretical Frequency Dependence Variable
F	Fraction
L	Inductance
r	Interest Rate
I	Investment Cost
J	Moment of Inertia
K	Gain
λ	Regulation Clearing Price
κ	Load Composition Factor
M	System Inertia Constant
$\beta_{\mathrm{t}}^{\mathrm{M}}$	Mileage Ratio between RegD and RegA
M	Mileage
ω	Angular Velocity
P	Active Power
ϕ	Phase Margin
Q	Reactive Power
RegA	PJM Area Control Error (ACE) Regulation Signal - Slow
RegD	PJM Area Control Error (ACE) Regulation Signal - Fast
R	Electrical Resistance
S	Apparent Power
α	Scaling Factor
T	Time Constant
σ	Theoretical Voltage Dependence Variable

Subscripts

0	Initial value
ac	AC value
C	Capability
CC	Current Control
CH	Main inlet volumes and steam chest
dc	DC value
dc1	MVDC value
dc2	LVDC value
dist	Disturbance
el	Electrical
f	Filter
g	Grid value
gov	Governor
HP	High pressure
i	Integral control gain
k	Current sample index
k-1	Previous sample index
m	Mechanical
max	Maximum
off	Off-state
OM	Operation and maintenance
on	On-state
P	Performance
p	Proportional control gain
pen	Penetration scaling
pf	Active power-to-frequency sensitivity parameter
fp	MV to LV Frequency Propagation
vp	MV Frequency to LV Voltage Propagation
pv	Active power-to-voltage sensitivity
q	Q-axis (dq-frame)
qf	Reactive power-to-frequency sensitivity parameter
qv	Reactive power-to-voltage sensitivity

RH	Reheater
sup	Support
th	Threshold
VC	Voltage Control

1 Introduction, Motivation, and Scope of Work

The task to mitigate the global climate crisis, challenges the way energy systems have been operated and conceptualized throughout the last century. Historically, the primary energy carriers and sources to supply the energy system have been predominantly fossil fuels. These fossil fuels were reliable sources of energy that could be scheduled and stored with ease. Nevertheless, scientists since the 70s of the last century have made it clear that the continuous use of fossil fuels pollutes and erodes our environment. This is most notably reflected in the concentration of greenhouse gases in the atmosphere, caused by the relentless emission of Carbon dioxide (CO_2) and other greenhouse gases. This increase in greenhouse gas concentration in the atmosphere is the main driver for global warming and the climate crisis [1]. The crisis is most prominently reflected in the increase of extreme weather events, rising sea levels, the loss of biodiversity and inhabitable areas around the globe [2]. To mitigate these impacts, the global energy system needs to cut the usage of fossil fuels as fast as possible, i.e., decarbonize.

In the grand scope of the global energy demand the following levers have been identified to allow the most efficient decarbonization of energy intensive sectors. First the accelerating technological advancements in the renewable energy generation pave the way for a relatively straightforward path to decarbonize current electrical processes and sectors, e.g., home appliances or industrial automation in manufacturing plants. That pathway seems straightforward but still needs immense financial and political investments to achieve the transformation of the existing infrastructure. The second lever introduces the real challenge, that is the electrification of large energy intensive sectors, mainly transportation, heating and chemical industry that are not yet electrified [3]. Eventually this means that not only the current electrical energy supply needs to be ensured and decarbonized with renewable energy resources but also the additional energy demand from the electrification of the aforementioned sectors. As an example, the International Renewable Energy Agency (IRENA) estimates for the hypothetical "1.5 °C scenario", that the share of electricity consumption relative to total global energy consumed must approximately double from 23% in 2022 to around 50% by 2050, even assuming a slight overall reduction in total energy consumption [4, 5].

The pathways to a carbon-neutral power system are multilayered. Even though the cost to generate electricity often referred to as Levelized Cost of Energy (LCOE) for Photovoltaic (PV) and wind (offshore and onshore) dropped below the LCOE of all other fossil fuel based technologies years ago, their integration into the existing energy networks remains challenging [6]. The reasons for that range from the weather dependent generation, geographical mismatch of generation and consumption, incompatible infrastructure, societal acceptance and political ideologies.

1.1 Power System Transformation Challenges

To provide the reader a sound background and before delving into the specific research questions and the key contributions of this work, this section provides an overview of challenges in the transition toward more sustainable power systems.

1.1.1 Renewable Energy Integration and Supply Reliability

One of the fundamental challenges modern power systems are facing is the reliable and affordable energy supply while transitioning to high shares of renewable energy resources. This transformation away from the traditional primary energy carriers like lignite, coal, and gas, manifests a paradigm shift that requires the integration of intermittent and non-dispatchable renewable generation while maintaining a high system reliability [7, 8].

In addition to the already challenging and accelerating climate crises, recent changes in the geopolitical landscape have further complicated this transition. Namely, the invasion of Russia into Ukraine and other hostile actions toward EU countries made the previously cheap and reliable fossil fuel carriers in particular gas more expensive, and the supply less reliable [9, 10]. This has accelerated the need for energy independence through renewable resources, but also highlights the complexity of the transformation ahead [11, 12].

The technical challenge of increasing renewable shares in power generation spreads across multiple domains and timescales. Daily operational challenges include managing the intermittency of PV and wind generation, requiring sophisticated weather and demand forecasting and flexible backup resources. The backup is achievable with Battery Energy Storage System (BESS) or fossil solutions like gas, the latter however, does not reduce the geopolitical dependencies nor achieve the zero-emission target [11]. More critical than the daily variability of solar irradiation and wind are seasonal variations and extended periods of low renewable output, known as "Dunkelflaute", where wind and solar production can simultaneously drop by 10–30% for periods extending from 24 hours to several days. To make things even more complex a recent study by Qu et al. in

2025 found that prolonged low-wind events, also known as wind droughts are likely to increase their duration until the end of the century by 20 - 40 % depending on the global temperature increase [13].

This intermittency and fluctuation of renewable resources requires advanced forecasting capabilities to anticipate generation availability, while reliably predicting the power demand with a high resolution. Plant-specific forecasting remains an active research field to achieve optimal results for system operators, to maintain the balance between production and demand in local areas and across large regions simultaneously. The challenge in accurate forecasts lies on many levels, from accurate weather models and reduced computational burdens to the correct modeling of the distribution system, where many factors influence the correct estimation of resource adequacy [14]. Inaccurate forecasts may directly impact customers, since mitigation of forecast errors can result in high dispatch costs for short-term power compensation with gas turbines or, in worst-case scenarios, load shedding.

Long-term challenges include meeting capacity targets for new renewable generation units paired with sufficient energy storage capacity to cover generation fluctuations. The replacement capacity must significantly exceed retiring fossil fuel capacity due to lower capacity factors of renewable resources. This necessitates robust forecasting models for high granularity levels and plant-specific data, accompanied by flexible and cost-effective power system equipment to enable generation re-dispatch and demand response actions to mitigate unavoidable forecast errors.

1.1.2 Limited Integration of New Resources

To accommodate the increasing amount of renewable energy sources needed to achieve the decarbonization goals, a transformed, reinforced and efficient power grid is required. The electrification of loads that were traditionally fuel-based, such as heating and transportation might not increase the primary energy demand, but will increase the electric energy demand. Their electrification leads to new high-power loads in the tens of kW range within the distribution system [8]. This creates the need for reinforced distribution systems with the capacity to accommodate high amounts of electric heat pumps and Electric Vehicle (EV)-charging infrastructure, avoiding transformer and line overloading as well as line congestion due to the increased bi-directional power flow [15]. In addition to the integration of renewable resources in distribution systems the transmission of large amounts of power between distant regions remains a challenge. Industry-heavy regions may not be located in areas with an abundance of wind and sunlight which requires a power transmission over long distances. A potential solution to that challenge are large HVDC systems, e.g., connecting the industry in the south of Germany with the wind parks in the north. Unfortunately, newly build HVDC systems as well as the reinforcement of existing structures require a

long planning and construction time and may be very expensive. Therefore, alternative solutions to traditional substations, and line reinforcements might be worth exploring, to achieve a cost-effective, fast and reliable power system transformation. Alternative solutions may include novel control concepts and new hardware, e.g., power electronic-based technologies such as PV, Energy Storage Systems (ESSs) or Solid-State Transformers (SSTs). Novel control concepts have the advantage to allow fast implementation without major physical changes and include the intelligent exploitation and management of the existing power flexibility or the adjustment of connection rules for new generation units.

1.1.3 Low Inertia Power Systems

Historically, large synchronous generators have been the backbone of the electrical power system. These generators inherently provide a stabilizing function through their large rotating masses, which store substantial amounts of kinetic energy that is instantaneously accessible to the power system. This stored energy enables the machines to respond immediately to power imbalances, buffering disturbances and maintaining system stability. The increasing penetration of Distributed Generation (DG) units, predominantly based on power electronics, fundamentally changes this dynamic. Unlike synchronous generators, these power electronics-based resources do not inherently provide inertia to the power system. Without additional measures, e.g., specific synthetic inertia provision, the overall system inertia will decrease as renewable energy sources progressively replace conventional power plants. To understand this phenomenon more rigorously, the dynamics of inertia can be described mathematically using Newton's first law of motion [16].

The simplified dynamics of a generator can subsequently be described with the following equation, commonly known as the *Swing Equation*:

$$J\frac{\mathrm{d}\omega}{\mathrm{d}t} = T_{\mathrm{m}} - T_{\mathrm{el}} \tag{1.1}$$

where J is the moment of inertia, ω is the angular velocity of the rotor and T_{m} and T_{el} represent the mechanical and electrical torques of the generator. Alternatively, the equation can also be expressed with respect to the power using the following relation between torque and active power.

$$P = \omega \cdot T \tag{1.2}$$

Leading to Eq. (1.3), which highlights the relation between power and rotational speed.

$$J\frac{\mathrm{d}\omega}{\mathrm{d}t}\omega = P_{\mathrm{m}} - P_{\mathrm{el}} \tag{1.3}$$

Now, because the power system dynamics are still dominated by large rotating masses, some power system dynamics can be described with the dynamics of large synchronous machines. One can see in Eq. (1.3) that an increase of electrical power P_{el} leads to a negative power balance, due to the resulting mismatch between electrical and mechanical power ($P_{\mathrm{m}} \neq P_{\mathrm{el}}$). This mismatch in turn leads to a negative $\frac{\mathrm{d}\omega}{\mathrm{d}t}$ and a reduced frequency $f = 2\pi\omega$. The resulting change in frequency is also experienced by other generators in the system which subsequently leads to a reverse reaction. Meaning, for a given P_{m} and a change of ω ($\frac{\mathrm{d}\omega}{\mathrm{d}t} \neq 0$) the electrical power P_{el} has to be changed accordingly to maintain the equilibrium between mechanical and electrical power.

This interaction between synchronous generators which balance each other through their inherent design and the stability they bring to the power system is no longer granted with the rise of renewable energy generation from PV and wind turbines. A reduced number of synchronous generators in itself is not directly an issue, the challenge is the transition between two very radical versions of the power system. The existing one that mostly relies on synchronous generators with significant amounts of inertia and one based on distributed generation that has close to no inherent inertia. What the equations above only implicitly expressed, is the fact that most large synchronous generators are not designed to endure high deviations of the nominal frequency. Increasing the penetration of renewables in the power system might do exactly this. The decreased inertia, can be seen as a reduction of J which causes higher $\frac{\mathrm{d}\omega}{\mathrm{d}t}$ and larger overall fluctuation of ω. During the transition period the amount of large synchronous generators is not negligible which means that simply turning them off in case of a large frequency deviation leads to a decrease of available mechanical power P_{m}. This could trigger a chain reaction resulting in generators tripping and eventually leading to a large blackout. Thus, it is of utmost importance to compensate the lack of inertia in some way, to limit the frequency deviation within the allowed frequency band and avoid cascaded failures. With respect to Eq. (1.3), the straight forward way to achieve this is by providing other active power compensation mechanisms reacting to frequency deviations.

1.1.4 Markets and Regulatory Frameworks

The previously mentioned technical challenges of renewable integration, electrification of new sectors, and inertia provision necessitate the development of new and overhauled regulatory frameworks and market mechanisms. However, this need also presents an opportunity to conceptualize these frameworks in a way that incentivizes participation in the energy transition and addresses the technical challenges in a structured and orderly manner. The overhaul of old and introduction of new frameworks is necessary because the historically grown power systems and their respective energy markets have been developed in times when the large majority of generation capacity was provided by a comparably small number of large power plants. That power system architecture lead to market frameworks optimized for large and slow power plants, with day-ahead trading,

in which the shortest trading window for services that are not simple transaction of energy, are 4-hours long, e.g, Frequency Containment Reserve (FCR) in Central Europe [17]. Even though system operators of smaller or weaker systems, e.g., Australia, ERCOT in Texas or, PJM on the North American East Coast, are expanding their frameworks, to allow participation of small and distributed systems in service related markets, that scenario is still far away in the European Network of Transmission System Operators for Electricity (ENTSO-E) controlled Central European system [18–20]. The main reason for that lack of innovation is the fact that the Central European system was considered strong and reliable and the margins before serious contingencies occur seemed quite big. This assumption changed considerably with the Iberian black out on 28th of April 2025, where large parts of the Iberian Peninsula were without power for more than 10 hours, due to large generators tripping and the failure of voltage controllers in multiple large power plants [21]. That example shows that even strong systems can experience significant difficulties and contingencies. The mitigation of such contingencies can be addressed not only by reinforcing the infrastructure but also by incentivizing distributed resources to participate in power system stabilization and strengthening mechanisms.

The mentioned challenges define the power system research landscape of today and are the foundation of the research questions to be answered in this dissertation.

1.2 Research Questions and Contributions

The technology under investigation in this thesis is the Asynchronous Grid Connection (ASG), a power electronic system, e.g., a SST, that establishes a connection between two AC grids, with the ability to transfer power while remaining decoupled in phase, frequency, and voltage magnitude. Control of the ASG converters is achieved by combining a grid-following control on the upstream grid side with a grid-forming control on the downstream side, to supply the interfaced distribution grid with a stable voltage and frequency reference. The research questions and key contributions below revolve around the ASG and bridge the gap between the power system analysis and power electronic controls. In the following each research question [RQ1 – RQ4] is explained in detail accompanied by small paragraphs laying out the key contributions [KC1 – KC9] of the present work to answer facets of these questions.

Research Question 1 [RQ1]: *What are potential grid services and scenarios that can be enabled by an ASG?*

The capabilities of power electronic devices are generally well explored due their widespread application in industrial processes and in recent years also in the power conversion within renewable energy sources. Such applications have been designed to work unidirectional, either absorbing

or injecting power from/into the power system. The interfaced devices, such as drives or PV systems had an underlying process that solely defined the power flow and allowed little to no flexibility, to maximize the owners economic interest. With the introduction of more intelligent interfaces, e.g., power electronic systems operating as an ASG, system operators can introduce increased controllability in essential routing points of the distribution grid. The question is how can the new flexibility of these systems really be utilized to benefit the power system operation, e.g., increasing economic efficiency by offering additional services to the power system. These services include, e.g., active power flow control to support the frequency in contingency events or boosting the voltage to increase hosting capacity of renewable energy sources.

[KC1] Power system perspective on grid services provided by power electronic systems. A foundational contribution of this thesis is the collection and assessment of existing control strategies for power electronic systems capable of establishing an ASG and identifying their potential to offer grid services. The main contribution here is the particular focus on active distribution networks and the potential exploitation of DG units.

[KC2] Identify and analyze possible ASG operation scenarios. An ASG can be utilized not only for local control goals, but also to enable certain grid configurations and scenarios in the larger vicinity of the connection. This contribution is mostly on the level of literature review and identifies technical features of the power electronic systems that enable certain grid configurations, such as soft-open point connections, partitioning of grid sections to allow autonomous operation, shared DC-Link control, and more.

Research Question 2 [RQ2]: *How can the performance and power system impact of an ASG be experimentally validated?*

A big concern in the power systems research community is the availability of accurate and valid models. Thus, the second research question concerns the testing methodology of ASGs for power system impact analysis. The research on power electronic systems is quite extensive and offers a wide range of models to simulate their behavior. Unfortunately, computational burden is a big issue in that regard, since a detailed power electronic simulation increases the burden to an extent where long-term simulations, in time scales of minutes, hours, or days, become quite a big endeavor. This is why simplified models are needed to provide sufficiently accurate models while reducing the computational burden and enabling the simulation of power systems and test cases over periods of multiple hours, days, or even years. One big challenge in this regard is the verification of the model accuracy, which is best realized by conducting experiments with real hardware. First, building and operating a power electronic system requires extensive know-how. Secondly, even more challenging, is the availability of infrastructure that allows the investigation of power electronic system interacting with a power system, such as a Power Hardware-in-the-Loop (PHIL) setup.

[KC3] Development of a Controller Hardware-in-the-Loop (CHIL) setup for ASG testing. The testing of real hardware in a PHIL environment requires a lot of know-how, workforce, and for the ASG testing it requires the occupation of two power amplifiers at once to interface both sides of the ASG to an emulated grid. Thus, a key contribution of this thesis, to allow faster and close to reality controller prototyping is the development of a CHIL test setup. The setup allows the emulation of the power electronic components of the ASG while using the same grid models and controllers as in the PHIL setup.

[KC4] Development of a double PHIL setup for ASG testing. To facilitate the execution of hardware testing, a testbench for ASGs using real power electronic hardware in a PHIL environment has been developed. A significant challenge that was successfully surmounted was the establishment of a double PHIL configuration. Two power amplifiers are needed because both sides of the system need to be interfaced to an emulated grid using a real-time simulation paired with an amplifier to convert the calculated voltages and currents.

Research Question 3 [RQ3]: *How can an ASG achieve a Fast-Frequency Response?*

As mentioned before, one of the major challenges in modern power systems evolving to high penetration levels of renewable energy sources is the loss of inertia and the increase in frequency fluctuations. On an abstract level, the frequency is a representation of the active power balance in the grid, and as such, a high fluctuation of the frequency is caused by bigger and longer active power imbalances in the grid paired with a reduced overall system inertia to damp and mitigate those imbalances. Inverter-based resources may not inherently provide inertia to damp the frequency volatility of the power system, but they can provide mitigating measures such as a Fast-Frequency Response (FFR). I.e., they can change their active power operating point with respect to the frequency at their grid connection point and thus mitigate the power imbalance causing the frequency deviation in the first place. With respect to the ASG concept the question is, whether an ASG is capable of offering a FFR as a services, i.e., adjusting the active power flow through the connection when necessary. This functionality implies that the ASG is capable of adjusting the active power flow of the downstream connected resources, without causing major disturbances to the connected systems. Subsequently, the question arises how this active power adjustment impacts the upstream grid and whether it can mitigate frequency disturbances effectively?

[KC5] Implementation of a FFR control concept for an ASG. The primary challenge in providing frequency response capabilities is the flexibility to adjust the active power flow. Additionally, it is imperative to ensure that the interfaced system can accommodate the active power flow adjustment. To achieve an active power adjustment in the connected downstream distribution system, this work proposes a new control concept for ASGs called *Frequency Propagation* method. The general idea is based on the exploitation of existing grid standards and device characteristics, aggregating

voltage and frequency sensitive DG units and loads. Specifically, the ASG control adjusts the voltage and frequency set point of the connected active distribution network and triggers active power adjustments due to the aforementioned sensitivity of the loads and generators. The proposed control enables the active power flow control without causing major interruptions to connected systems and customers, and without the need of an additional communication infrastructure.

[KC6] System impact assessment of the ASG FFR concept using double PHIL. After showing the capability to adjust the active power flow exploiting frequency and voltage sensitivity, the question remained, how this active power flow adjustment impacts the upstream power system? Thus, a simplified upstream power system model is implemented to quantify the impact of the active power adjustment on the actual power balance which caused the mentioned frequency disturbances. The developed ASG controller is therefore tested in a double PHIL environment in which the live active power adjustments are fed into a power system model to emulate the resulting impact on frequency disturbances.

Research Question 4 [RQ4]: *How can the economic viability of an ASG be evaluated?*

A major bottleneck for the introduction of new technologies and operating concepts is the question of economic viability, in this case the question: Can an ASG yield an economic benefit to a system operator or a private investor? The challenging part in answering this question is the fact that transmission and distribution system operators are usually quite slow in evolving their frameworks and introducing new market schemes and standards for new and niche technologies. This is not necessarily a bad thing, since the operators bear a big responsibility to provide safe and uninterrupted power to all connected entities. Nevertheless, market frameworks in which new, small, decentralized, and dynamic devices, can participate are hardly available or do not exist at all which prevents them from receiving sufficient remuneration. Thus, a framework is needed to evaluate the economic viability of an ASG and potentially other power electronic systems in the future.

[KC7] Identification of FFR service markets for dynamic resources. With the above question and challenge in mind, a contribution of this thesis is the identification of existing market frameworks with remuneration schemes for dynamic services. After identifying existing frameworks and markets, a basic case study was designed to demonstrate how the ASG could operate within the chosen framework. This concrete case study was conducted within the market framework of Pennsylvania New Jersey Maryland (PJM), a North American regional transmission operator.

[KC8] Developing a model of an ASG for long-term simulations. An economic analysis requires a long-term assessment of the technology. A contribution to the research question at hand was the development of a sufficiently accurate Root-Means-Square (RMS) capable model that allows a computationally inexpensive execution and, as such, enables simulation over long time scales.

[KC9] Performance of the ASG in a long-term simulation in the PJM frequency response market. With a compatible market framework identified, and a long-term simulation model available, a case study is conducted by running simulations over a time frame of an entire year. The resulting data is subsequently used to estimate the possible revenue generated by participating in the frequency response market of PJM. This allows a long-term economic analysis, using standard financial metrics such as net-present value, internal rate of return or the cumulated cashflow over a 15-year investment horizon.

1.3 Scope of Work and Structure

With the research questions defined and the key contributions explained, the scope of work for this thesis can be summarized as follows:

- Review and assessment of possible services and scenarios that can be offered by an ASG.
- Proposal of the novel *Frequency Propagation* method exploiting and aggregating DG units to provide a FFR.
- Design and implementation of an ASG with real hardware, applying the proposed control method.
- Development of a PHIL setup that allows the testing of an ASG with valid power system models on both ends of the connection.
- Experimental testing of the proposed control within the developed PHIL setup to emulate its system integration and subsequently analyze its system impact and disturbance mitigation potential.
- Development of an average model representing the ASG and enabling long-term power system simulations.
- Identify and calculate potential revenue streams in a concrete case study, deploying the ASG model.
- Economic projection over a 15-year investment horizon using financial investment metrics to estimate the ASG's economic viability.

The four research questions [RQ1 – RQ4], their respective contributions [KC1 – KC9], and the summarized scope of work establish the framework for this thesis. The resulting structure is illustrated in Fig. 1.1. Each chapter is associated with one of the focus areas of the thesis, either the power system control and services or the power electronic control, highlighted with the blue

and green shaded background, respectively. Additionally, the underlying research questions X and publications Y are paired with the corresponding chapter in the form, [RQX] – [Publication Key (CY, JY)], where C and J represent conference and journal publications, respectively. In detail the thesis and chapters are organized as follows.

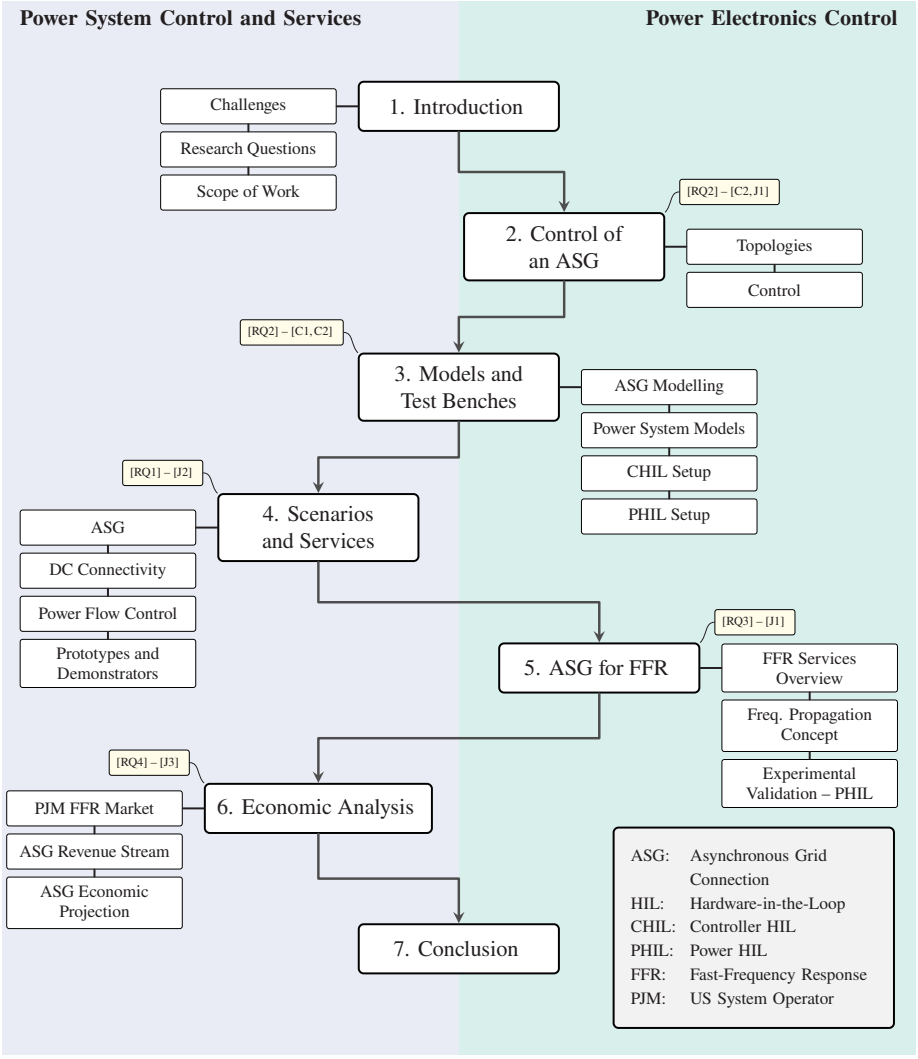

Figure 1.1: Flowchart of the thesis structure aligned with the overall research field and paired with the respective research questions and publications.

The first and current chapter (Chapter 1) introduces the reader to the current state of the power system. This includes challenges in the transition of modern power systems resulting in the motivation for this thesis and the definition of research questions. Each research question is paired with the key contributions of this work with respect to the questions and the overall structure of the thesis.

Following the introduction, Chapter 2 presents the technical description of the ASG concept. Providing a brief overview of topologies to establish an ASG and subsequently a deep description of a Back-to-Back Converter (B2B) system as the core hardware this thesis revolves around. The chapter also covers the basic and advanced control of ASGs including Grid-Forming (GFM) and Grid-Following (GFL) control of grid-connected Voltage-Source Converters (VSCs).

Chapter 3 derives and describes models to simulate and test the ASG. This includes average models of the B2B system as well as the interfaced power system models. These models are subsequently used to establish the validation setups, CHIL and double PHIL, which is the key contribution of this chapter to answer [RQ2].

Potential scenarios and services enabled by the ASG are reviewed and assessed in Chapter 4. This assessment is paired with simulation examples to showcase certain features and provide the key contributions to [RQ1]. Chapter 4 concludes with an overview of projects, demonstrators, and companies currently pursuing the development and research on ASGs, with SSTs in particular.

The experimental test of the previously introduced active power flow controller with the developed models and implemented experimental setups are presented in Chapter 5. These tests results demonstrate the performance of the control concept and follow up with the power system impact assessment on frequency disturbance mitigation, as questioned in [RQ3].

The last research question [RQ4] is covered in Chapter 6, in which the identified active power flow flexibility is used to investigate potential revenue streams and scenarios that allow a reliable economic assessment. Leading to a long-term economic analysis of an ASG operating in a realistic market framework that identifies the economic viability and robustness of the proposed concept.

Finally, Chapter 7 concludes the thesis with a summary of the key findings and contributions, followed by an outlook on future research directions and a vision for future power systems.

2 Control of an Asynchronous Grid Connection

The introduction highlighted the challenges of net-zero emission power systems, mentioning the fact that a simple replacement of generation capacity is not sufficient to guarantee a resilient and reliable power system. This chapter presents a power electronics-based system with the potential to provide grid supportive services and enable DG units to participate in these services. The power electronic system is referred to as *Asynchronous Grid Connection* and can be realized with a wide variety of power converter topologies and combinations. After a thorough introduction of the general concept, two exemplary topologies to establish such an asynchronous connection are presented. The first is a *Three-Stage Solid-State Transformer* which can act as a distribution grid interface or substation replacement on its own, and secondly a *Back-to-Back Converter* system, that has no MV interface and, as such, can be used to enhance existing substations.

Definition. We define the concept of an Asynchronous Grid Connection (ASG) as the coupling of two grids using a power electronic system, with power transfer capability while maintaining the independence of frequency, phase and voltage magnitude of the connected grids.

A schematic of the concept is displayed in Fig. 2.1, where specific emphasis is put on the frequency (f) and voltage magnitude ($\hat{V}$), which are decoupled in this case. f_1 and $\hat{V}_1$ are dictated by the upstream power system, whereas f_2 and $\hat{V}_2$ can be adjusted and controlled by the GFM converter of the ASG shown as the AC/AC block in the center.

The asynchronous operation of the downstream LV distribution system implicates that the converter feeding the LV system may be required to form the grid, since there is no alternative reference bus or stiff coupling to the main grid. That means a GFM control algorithm is deployed to operate the LV converter to maintain a stable voltage and frequency. Subsequently, the MV connection towards the upstream grid needs to supply as much power to the whole power electronic system as the connected systems, including the LV distribution system, demand.

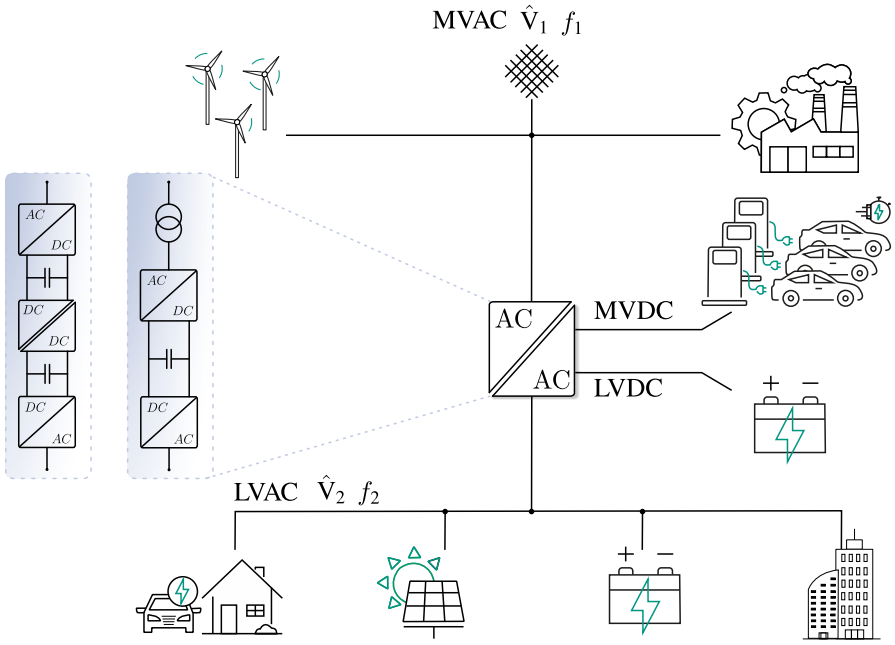

Figure 2.1: ASG concept figure, showing the decoupling between MV (subscript 1) and LV (subscript 2) frequency (f) and voltage magnitude ($\hat{V}$), with the AC/AC block in the center, representing a power electronic system. Two potential topologies to establish the connection, the SST (left) and B2B (right), are displayed on the left side.

2.1 Power Electronic Topologies to establish Asynchronous Grid Connections

An ASG can be established by many combinations of power electronic switches, often a combination of the VSC technology, usually referred to as a *Power Electronic Transformer* or *Solid-State Transformer*. Additionally, the Back-to-Back configuration of two combined low voltage VSCs is considered to offer similar capabilities if connected in series to an existing Line-frequency Transformer (LFT). The following section will introduce one topology for each stage with a focus on controls, specifically on the B2B since this topology will be used in the later experimental validation. As the work primarily concentrates on power system integration and service capabilities, which are evaluated on a millisecond to second timescale where the particular power electronic topology provides limited significance, this approach will provide adequate insights.

2.1.1 The Solid-State Transformer

The SST is based on the original concept of a Power Electronic Transformer, which became possible with the invention of the high-power DC//DC converter by Brook and McMurray in 1970 [22]. At the time, the efficiency of semiconductors was not sufficiently evolved to render the idea a competitive solution, but with the advent of efficient, high-power semiconductors such as the Insulated Gate Bipolar Transistor (IGBT) or the Silicon Carbide MOSFET (SiC-MOSFET), the idea gained traction within the power electronic research landscape. In short, the DC//DC converter is able to transfer power from one DC voltage level to another by establishing a high or medium frequency link between two full-bridge circuits. Combined with the widely known and mature AC/DC converter, it provides a fully power electronic-based solution to connect different voltage levels, commonly referred to as the *Solid-State Transformer*, a three-stage topology example is displayed in Fig. 2.2.

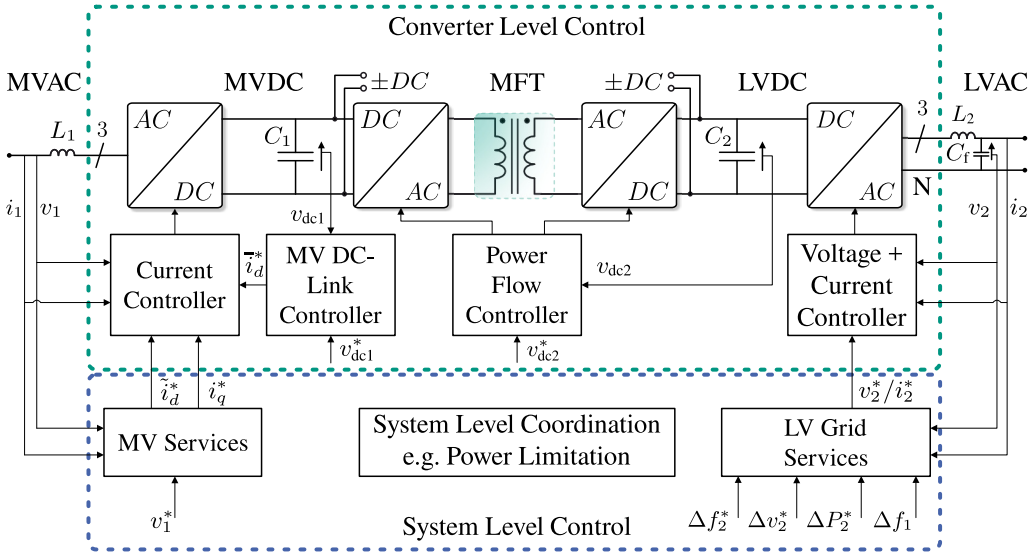

Figure 2.2: Three-stage SST topology, with a generalized high level control structure.

The three-stage SST architecture consists of an input MV AC/DC rectifier stage, a DC//DC conversion stage, and a LV AC/DC inverter stage. This configuration provides maximum control flexibility while maintaining galvanic isolation between input and output.

In the illustration Fig. 2.2 the voltage and current measurements are denoted by v and i with subscript 1 and 2 for the primary (MV) and secondary (LV) side, respectively. The set points are identified by a super script *, e.g. v_1^* as the voltage support set point on the primary side, where

in the *System Level Control* Δf_2^*, Δv_2^* and ΔP_2^* are adaption set points to control the secondary side voltage, frequency or active power to offer certain services. The same can be said for Δf_1^*, although this is a value of the primary side potentially used in services and controllers on the secondary side e.g. to support the primary side frequency. On the *Converter Level Control* the set points such as DC link voltage (v_{dc1}^* or v_{dc2}^*) define the voltage level of each DC link, while i_d^* and i_q^* are set points for the underlying current controller, either for the main component with a straight bar above ($\bar{i}_d^*$) or a tilde ($\tilde{i}_d^*$) for the alteration of the main component, e.g. for active damping or other services. The three stages can be implemented using different topologies of converters for each stage; as an example and for reasons of simplicity, a topology with independent stages is presented as opposed to a cell-based modular SST, which can provide more flexibility, modularity, and scalability, but is more complex.

2.1.1.1 MV Converter Stage

Rectifying the MVAC voltage to provide a stable DC voltage is usually achieved using a variation of one of three power electronic concepts displayed in Fig. 2.3.

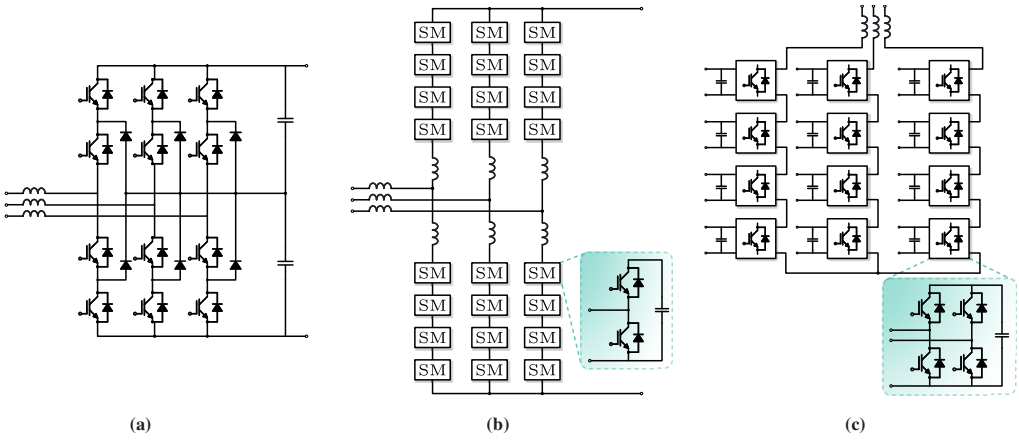

Figure 2.3: Three possible topologies for MV converters, with a three-level neutral point clamped converter displayed in a), a Modular Multi-level Converter (MMC) in b) and a Cascaded H-Bridge (CHB) in c), adopted from [23].

A classic solution is a multi-level converter topology that can be achieved using semiconductors of high blocking voltages, e.g., IGBTs with 3.3 kV blocking voltage. The multi-level converter can be arranged in very different ways, to achieve e.g., up to nine levels or allow active neutral point clamping. Fig. 2.3a illustrates a three-level neutral point clamped converter as proposed by Nabae et al. in 1981 [24]. The MMC displayed in Fig. 2.3b is a more modular approach to a

multi-level solution, which is comprised of in-series connected half-bridge submodules to achieve the necessary MVAC level. One of the big advantages of these converter types is the availability of a MVDC link, that allows direct integration of MVDC loads and generators [25, 26]. As an alternative, the CHB based converter topology (Fig. 2.3c) only relies on low voltage components, without the need for high blocking voltages with the obvious downside of not having a MVDC link [27]. In the CHB topology, each module usually comes with its own DC//DC converter to connect either to a common LVDC link or interface multiple LVDC devices separately. This enables a very modular, scalable and flexible topology.

The main control objective of the MV converter side is usually the reliable supply of a stable DC link voltage, generally referred to as Active Front End (AFE). Active because the above-mentioned topologies all operate with components that need active switching signals, as opposed to a passive rectifier that operates only using passive diodes. The advantages of the active topologies are first and foremost flexibility and the ability to allow bidirectional power flow, paired with improved efficiency. A detailed control scheme of an AFE will be discussed in a later section of the ASG implementation.

2.1.1.2 DC//DC Converter Stage

The DC//DC stage is the core of the SST, because it is the main reason a voltage transformation to different voltage levels is possible at all, and it provides the galvanic isolation that is essential for current system operators. As introduced before, the general idea of a DC//DC converter is not particularly new, but the technological advancements of semiconductors only recently provided high power switches that could realize the concept efficiently. The main challenge was the need for a high switching frequency which caused high losses; with the development of SiC-MOSFET and new generations of IGBT semiconductors, the switching frequencies can be increased while still managing a relatively high efficiency.

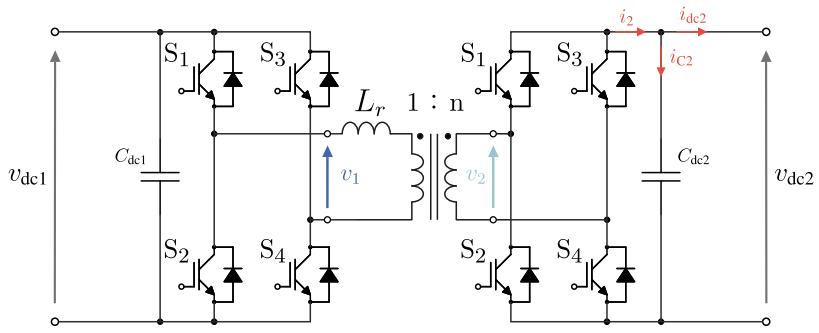

Figure 2.4: Dual Active Bridge (DAB) circuit schematic with magnetic coupling.

Since the DC//DC converter is not part of the final test validation setup, only the general operation concept of one common high power DC//DC converter topology will be discussed, namely the DAB. Low-level hardware implications superfluous for the research findings and validation in this thesis are omitted.

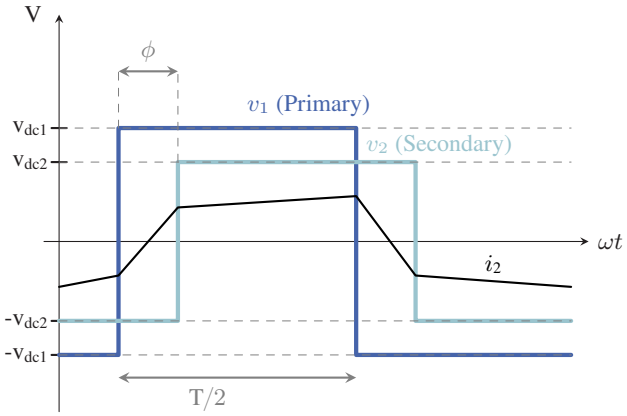

Figure 2.5: Phase shift control of a DAB converter, showing the two voltage levels and the phase shift between the two AC voltages.

The DAB is a medium or high-frequency link using a magnetic coupling to transfer power, as shown by the inductors at the center of Fig. 2.4. Each side is made of a full bridge converter, with 4 switches denoted (S_{1-4}); their switching patterns achieve a square wave voltage v_1/v_2 with a phase shift ϕ, as illustrated in Fig. 2.5. The phase shift is the main variable to control and influence the amount of power transferred between the sides. Assuming an externally provided voltage v_{dc1} supplies the primary side, as is common in a SST, the main objective of the control of the DAB is to regulate the voltage v_{dc2}; this is achieved by adjusting the current i_2. Applying Kirchhoff's current law, the currents are linked as follows:

$$i_2(t) = i_{dc2}(t) + i_{c2}(t) \tag{2.1}$$

where $i_{dc2}(t)$ is the current supplied to the LVDC terminals and $i_{c2}(t)$ is the current flowing into the LVDC link capacitor. Using $i_{c2}(t) = C_{dc2}\frac{dv_{dc2}(t)}{dt}$ the LV DC link voltage dynamics become:

$$\frac{dv_{dc2}(t)}{dt} = \frac{i_{dc2}(t)}{C_{dc2}} - \frac{i_2(t)}{C_{dc2}} \tag{2.2}$$

Further investigations into the circuitry reveal, as discussed by Qin and Kimball in 2013, that the power transfer between the two bridges can be described by the following equation [28]:

$$P_{\mathrm{DAB}} = \frac{v_{\mathrm{dc2}} v_{\mathrm{dc1}}}{2N f_{\mathrm{s}} L_{\mathrm{r}}} \phi(1-\phi) \tag{2.3}$$

where f_{s} is the switching frequency, L_{r} the leakage inductance of the transformer, N the turn ratio of the transformer and ϕ the phase shift ratio between v_1 and v_2.

To avoid a deep dive into low-level power electronics at this time, the following references can provide additional information on functionality, control, and other topologies to achieve the voltage transformation and galvanic isolation with power electronics [29–33].

2.1.1.3 LV Converter Stage

The low-voltage side of the SST can be realized by using conventional low-voltage VSCs in a two or three level configuration, as illustrated in Fig. 2.6a or Fig. 2.6c, respectively. Additionally, four-leg topologies (Fig. 2.6b), as discussed by Zhang et al. in 2002 and Sul and Kim in 2004, can offer enhanced performance for unbalanced or single-phase loads as well as the ability to control the zero-sequence voltage/current [34, 35]. Any further discussion of the LV converter stage will be moved to Section 2.2, which discusses its topology and modulation techniques in detail.

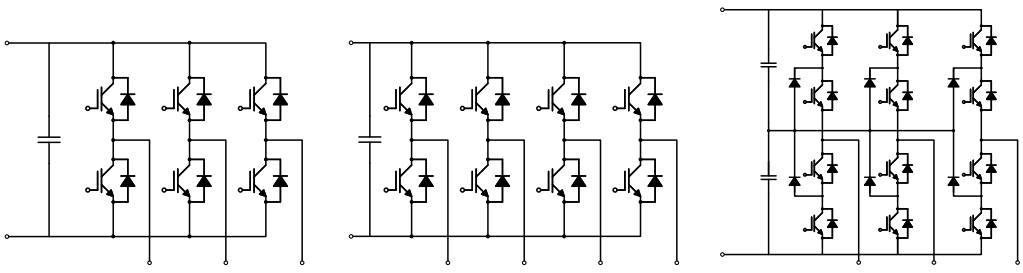

Figure 2.6: Schematics of common LV VSC topologies, with a two-level converter displayed in a), a two-level converter with four legs to connect the neutral conductor in b) and a three-level neutral point clamped converter in c).

2.1.2 The Back-to-Back Converter

The Back-to-Back Converter (B2B) topology represents a mature solution for an ASG, based on well-established technologies such as the above shown VSC (Fig. 2.6a). The basic configuration illustrated in Fig. 2.7, consists of two VSCs sharing a common DC link to exchange power and

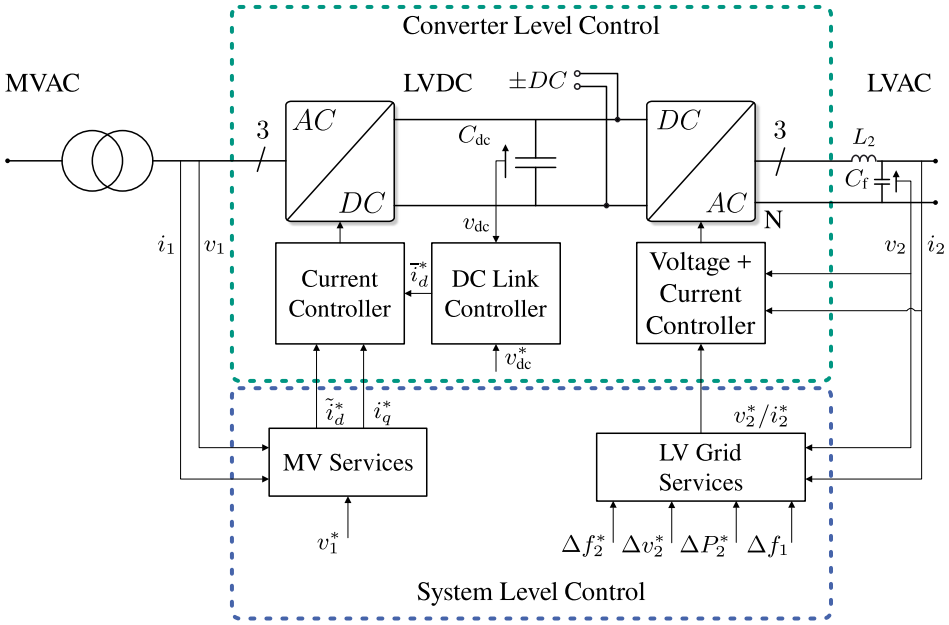

Figure 2.7: B2B topology, with a generalized high level control structure.

connect to a three-phase AC grid on each side of the system. As for the SST the control objectives of the two sides are similar, without the DC//DC converter in-between. A common operation scenario as illustrated in Fig. 2.7 is to operate the converter connected to the upstream grid here on the left side, as an AFE, thus being responsible for the provision of a stable DC link voltage supply, similar to the MV converter of the SST. The other converter can subsequently operate quite flexibly either simply controlling the power flow in and out of the connection, like a soft-open point, or act as a grid-forming node and synthesize a voltage to supply a downstream distribution grid.

This concludes the general introduction to power electronic systems capable of establishing an ASG. The next section provides a detailed discussion on the VSC technology, which is the core power electronic hardware used in the later experimental setups.

2.2 The two-level Voltage-Source Converter

The main power electronic hardware of interest for this work is the B2B system, which is made of two VSC connected via their DC terminals. This technology has a very simple, but currently most important advantage over the SST, the availability of products that can be ordered more or

less off the shelf. The B2B is a frequently deployed power electronic system for various drive and industry applications requiring efficient and bidirectional power supply. The two-level topology is chosen in this work due to its simplicity and well-established control, modulation, and filter design procedures. Since the primary function is to control the active power flow between the two sides, introducing topologies of higher complexity does not yield any significant advantage.

2.2.1 The Power Electronic Topology

Each VSC in the two-level configuration discussed and used in the following, consists of six power semiconductors, two per phase, as shown in Figure 2.8. This topology can turn the switches on/off to create a certain voltage potential between the AC terminals a, b, c and the DC terminals + and - as displayed in the schematic. Based on the potential between those two terminals a certain current will flow between them depending on the direction of the potential. This current flow can subsequently be used to charge the capacitor C_{dc} to maintain a certain voltage v_{dc} or various other applications, such as power control or voltage synthesis.

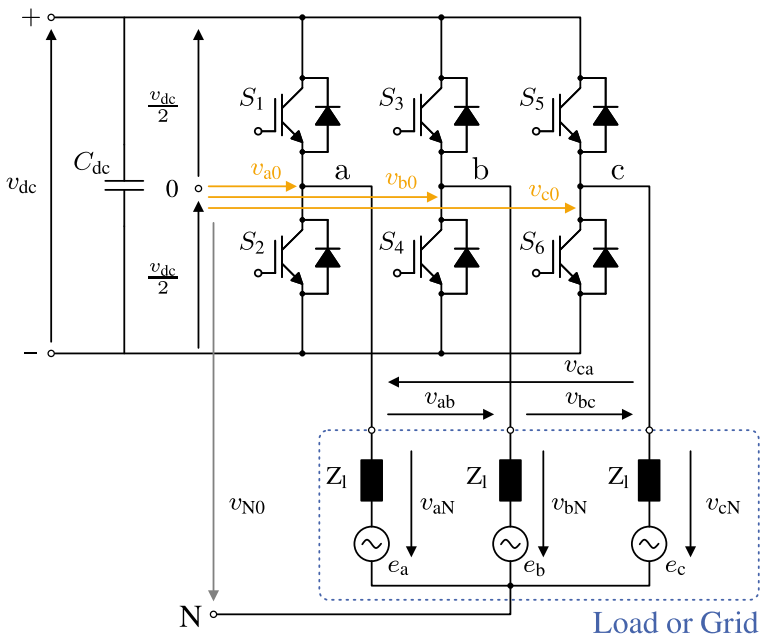

Figure 2.8: Detailed schematic of a two-level VSC.

To simplify things for the sake of modeling and understanding, a set of two semiconductors per phase can be seen as a switch with two states defined as

$$s_{x\in\{\mathrm{a,\ b,c}\}} = \begin{cases} +, & \text{when upper transistor on} \\ -, & \text{when lower transistor on} \end{cases} \tag{2.4}$$

To synthesize a balanced three-phase voltage system, it is necessary to control the phase voltages (v_a, v_b, v_c). Practically this can be realized by clamping of the nodes a, b and c to either positive or negative DC-link potential by activating the respective switch. This results in a line to neutral voltage, e.g. v_a0 of $\pm\frac{v_\mathrm{dc}}{2}$. With an unconnected neutral point, as seen in Fig. 2.8, a common mode voltage v_N0 is generated which can be calculated with the following equation:

$$v_\mathrm{N0} = \frac{1}{3}(v_\mathrm{a0} + v_\mathrm{b0} + v_\mathrm{c0}) \tag{2.5}$$

With Equation (2.5) the phase voltage v_a is derived as follows:

$$v_\mathrm{a} = v_\mathrm{a0} - v_\mathrm{N0} \tag{2.6}$$

An activation of both the upper and lower switch of the leg must be avoided at all times, since this would allow a very high current only limited by the parasitic inductance and the on-state resistance, basically a short circuit. These currents would lead to the thermal destruction of the semiconductor in a very short time [36]. All allowed switching states sum up to $2^3 = 8$ voltage

Table 2.1: Switching states and voltages of a two level VSC.

State No.	Phase			Phase Voltages			$\alpha\beta$ - System	
	a	b	c	$\frac{v_\mathrm{a}}{v_\mathrm{dc}}$	$\frac{v_\mathrm{b}}{v_\mathrm{dc}}$	$\frac{v_\mathrm{c}}{v_\mathrm{dc}}$	$\frac{v_\alpha}{v_\mathrm{dc}}$	$\frac{v_\beta}{v_\mathrm{dc}}$
S0	-	-	-	0	0	0	0	0
S1	+	-	-	$\frac{2}{3}$	$\frac{-1}{3}$	$\frac{-1}{3}$	$\frac{2}{3}$	0
S2	+	+	-	$\frac{1}{3}$	$\frac{1}{3}$	$\frac{-2}{3}$	$\frac{1}{3}$	$\frac{1}{\sqrt{3}}$
S3	-	+	-	$\frac{-1}{3}$	$\frac{2}{3}$	$\frac{-1}{3}$	$\frac{-1}{3}$	$\frac{1}{\sqrt{3}}$
S4	-	+	+	$\frac{-2}{3}$	$\frac{1}{3}$	$\frac{1}{3}$	$\frac{-2}{3}$	0
S5	-	-	+	$\frac{-1}{3}$	$\frac{-1}{3}$	$\frac{2}{3}$	$\frac{-1}{3}$	$\frac{-1}{\sqrt{3}}$
S6	+	-	+	$\frac{1}{3}$	$\frac{-2}{3}$	$\frac{1}{3}$	$\frac{1}{3}$	$\frac{-1}{\sqrt{3}}$
S7	+	+	+	0	0	0	0	0

combinations at the output terminals, all listed in Table 2.1, including two free-wheeling states S0 and S7. The other states form six voltage vectors in the complex plane, of length $\frac{2}{3}v_{\mathrm{dc}}$, which result in different effective phase voltages. The three phase columns a, b and c represent the state of the switches at the respective phase, based on the states defined in Eq. (2.4).

2.2.2 Modulation

To determine the correct switching state for the desired output, a classic carrier-based Pulse Width Modulation (PWM) can be used to generate the switching signals [37]. In the following example, a triangular carrier signal (light blue) is compared with a single phase voltage modulation signal (blue), as shown in the upper part of Fig. 2.9. In this scenario the PWM signal is calculated to *High* if the modulation signal is greater than the triangular carrier signal and thus switch S1 in Fig. 2.8 is turned on, while the switching signal for the lower power semiconductor is *Low*.

In the lower part of Fig. 2.9, it can be seen that the PWM output switches from *Low* to *High* whenever the modulation signal (blue) is greater than the triangular carrier signal (light blue) and vice versa. In this way the output states of the switches synthesize the reference voltage signal at the converter terminal through rapid switching between the two DC terminal voltages.

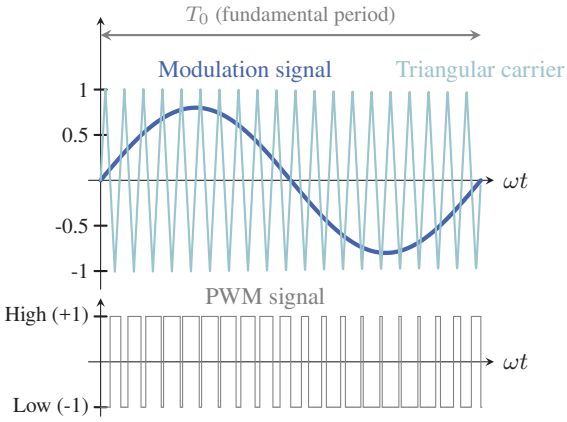

Figure 2.9: Carrier-based PWM modulation showing a sinusoidal modulation signal and triangular carrier (upper subplot) with resulting digital PWM switching output (lower subplot).

2.3 Control Strategy for the Back-to-Back Converter

The previous two sections described general operation principles of ASG systems such as the SST and B2B, paired with a brief introduction to the underlying hardware of the LV two-level VSC. The VSC is commonly used to establish the B2B system, the hardware of interest for this thesis, which is why the following subsections focus on the control methods of the B2B, including some basic fundamentals such as the three-phase system transformation. In the previous subsections subscript 1/2 were used to identify the voltages and currents for each side and/or voltage level of the asynchronous connection respectively. In the following subsections, the voltages and currents are clearly dedicated to a certain voltage level, thus we refrain from highlighting that in the subscript and rather clearly identify the type of signal, e.g., three-phase abc, $\alpha\beta$ or dq.

2.3.1 Three Phase System Modeling

If one tries to control the converter output voltage through each phase a, b or c separately, problems such as the coupling of the phases and their influence on each other may occur. Instead of using a controller to minimize the error of each phase to zero and thereby influence the other phases, a mathematical method in form of the dq-transformation is introduced. This method is widely known as the *Park* transformation, presented in graphical form in Fig. 2.10 [38]. It consists of two transformations, first the *Clark* transformation, converting a three-phase system, e.g., abc into a two-dimensional space vector in the $\alpha\beta$ system, illustrated in Fig. 2.10a and in a second step a rotation of the system by a given angle θ, shown in Fig. 2.10b. In a grid connected system, the angle of the grid voltage is used, usually denoted as θ. In a three-phase voltage system of 50 Hz the d and q components should ideally be constant quantities; however, ripples may occur due to harmonics of different frequencies. According to Yazadni and Iravani (2010) the three phase voltages at the converter terminals can be expressed using the following equations derived from the variables in Figure 2.8 and applying the *Park* transformation [39]. The impedance is specified as $\mathrm{Z_l} = L_\mathrm{l} s + R_\mathrm{l}$. Applying the Kirchhoff's Voltage Law (KVL), the phase voltages v_abc are determined as follows:

$$v_\mathrm{a} = L_\mathrm{l}\frac{\mathrm{d}i_\mathrm{a}}{\mathrm{d}t} + R_\mathrm{l} i_\mathrm{a} + e_\mathrm{a} \tag{2.7}$$

$$v_\mathrm{b} = L_\mathrm{l}\frac{\mathrm{d}i_\mathrm{b}}{\mathrm{d}t} + R_\mathrm{l} i_\mathrm{b} + e_\mathrm{b} \tag{2.8}$$

$$v_\mathrm{c} = L_\mathrm{l}\frac{\mathrm{d}i_\mathrm{c}}{\mathrm{d}t} + R_\mathrm{l} i_\mathrm{c} + e_\mathrm{c} \tag{2.9}$$

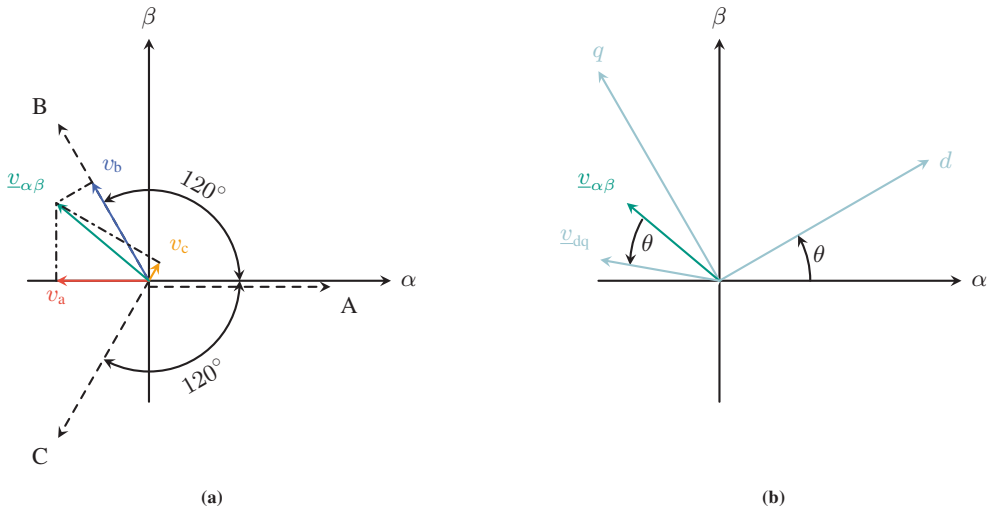

Figure 2.10: The *Park* transformation consisting of (a) the *Clark* transformation and (b) the transformation from the stationary $\alpha\beta$ into the rotating dq system.

This set of equations can then be compressed into one vector in the $\alpha\beta$ system by means of a different vector $a = e^{j\frac{2\pi}{3}}$, resulting in:

$$\underline{v}_{\alpha\beta} = \frac{2}{3}(v_a + a v_b + a^2 v_c) \tag{2.10}$$

$$\underline{v}_{\alpha\beta} = L\frac{\mathrm{d}i_{\alpha\beta}}{\mathrm{d}t} + e_{\alpha\beta} + Ri_{\alpha\beta} \tag{2.11}$$

Transforming these quantities into a system rotating along the reference angle in this case θ, the derivative of the frequency ω, provides the advantage of having not only 2, but also nearly constant values. These represent the real and imaginary parts of the three-phase system, i.e. the active and reactive components. Mathematically, the rotation of the vector is a simple multiplication, which rotates the vector by the angle θ:

$$\underline{v}_{dq} = \underline{v}_{\alpha\beta} \cdot e^{-j\theta} \quad \leftrightarrow \quad \underline{v}_{\alpha\beta} = \underline{v}_{dq} \cdot e^{j\theta} \tag{2.12}$$

$$\underline{e}_{dq} = \underline{e}_{\alpha\beta} \cdot e^{-j\theta} \quad \leftrightarrow \quad \underline{e}_{\alpha\beta} = \underline{e}_{dq} \cdot e^{j\theta} \tag{2.13}$$

$$\underline{i}_{dq} = \underline{i}_{\alpha\beta} \cdot e^{-j\theta} \quad \leftrightarrow \quad \underline{i}_{\alpha\beta} = \underline{i}_{dq} \cdot e^{j\theta} \tag{2.14}$$

Substituting the quantities of Eq. (2.11) with the $\alpha\beta$ vectors of the previous set of Eq. (2.12) and transferring this into the rotating reference frame, yields the following equation for the dq quantities:

$$\underline{v}_{dq} - e_{dq} = L\frac{\mathrm{d}i_{dq}}{\mathrm{d}t} + Ri_{dq} + j\dot{\theta}Li_{dq} \tag{2.15}$$

Such a vector can also be decomposed into the real and imaginary components:

$$\underline{v}_{\mathrm{dq}} = v_{\mathrm{d}} + jv_{\mathrm{q}} \tag{2.16}$$

Applying this decomposition to Eq. (2.15) yields the following two coupled differential equations in the time domain:

$$v_{\mathrm{d}} - e_{\mathrm{d}} = L\frac{\mathrm{d}i_{\mathrm{d}}}{\mathrm{d}t} + Ri_{\mathrm{d}} - \dot{\theta}Li_{\mathrm{q}} \tag{2.17}$$

$$v_{\mathrm{q}} - e_{\mathrm{q}} = L\frac{\mathrm{d}i_{\mathrm{q}}}{\mathrm{d}t} + Ri_{\mathrm{q}} + \dot{\theta}Li_{\mathrm{d}} \tag{2.18}$$

For the subsequent control system design, we transform these time-domain differential equations to the Laplace domain. Applying the Laplace transform to Eq. (2.17) and assuming zero initial conditions, the derivative operator $\frac{d}{dt}$ is replaced by the complex frequency variable s, yielding:

$$v_{\mathrm{d}}(s) - e_{\mathrm{d}}(s) = sLi_{\mathrm{d}}(s) + Ri_{\mathrm{d}}(s) - \dot{\theta}Li_{\mathrm{q}}(s) \tag{2.19}$$

$$v_{\mathrm{q}}(s) - e_{\mathrm{q}}(s) = sLi_{\mathrm{q}}(s) + Ri_{\mathrm{q}}(s) + \dot{\theta}Li_{\mathrm{d}}(s) \tag{2.20}$$

This Laplace-domain representation enables the application of classical control design techniques, including the design of compensators based on transfer functions, frequency-domain analysis via Bode plots, and systematic tuning based on stability margins. The coupling terms $\dot{\theta}Li$ represent the cross-coupling between the d and q axes, which will be addressed through feed-forward decoupling in the controller design.

2.3.2 Grid-following - Active Front End

To successfully control the DC link voltage v_{dc} and keep it at a constant predefined level, the primary side converter facing the upstream grid is operated as an AFE. It is realized by a VSC that operates as an active rectifier and its control algorithm utilizes the advantages of mathematical transformations introduced in Section 2.3.1. Specifically, when introducing the link between AC and DC side, which can be made with the use of the active power transfer function as follows:

$$v_{\mathrm{dc}} \cdot i_{\mathrm{dc}} = \frac{3}{2}(v_{\mathrm{d}} \cdot i_{\mathrm{d}} + v_{\mathrm{q}} \cdot i_{\mathrm{q}}) \tag{2.21}$$

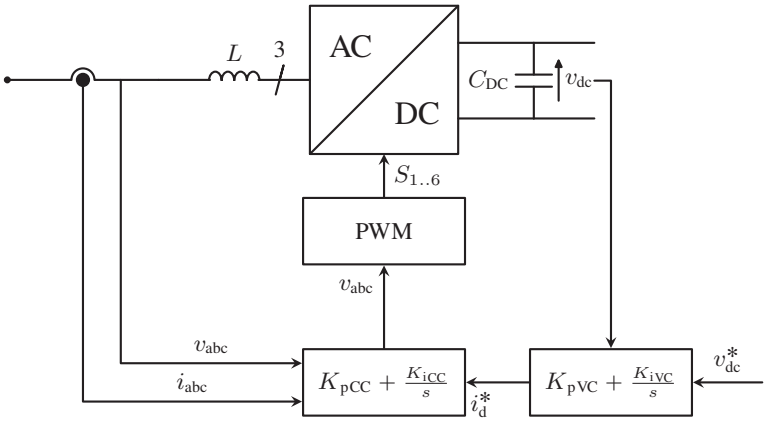

Figure 2.11: Detailed view of the AFE control structure, showing the signal routing and cascaded voltage and current controller.

Since the goal in this application is to transfer active power only, the set point for i_{q} is set to $i_{\mathrm{q}}^* = 0$, making the d-component directly coupled to the active power transfer. This is clearly seen in the equation below, which follows from the assumption $i_{\mathrm{q}} = 0$ and the rearrangement of Eq. (2.21):

$$i_{\mathrm{dc}} = \frac{3}{2} \frac{v_{\mathrm{d}} \cdot i_{\mathrm{d}}}{v_{\mathrm{dc}}} \tag{2.22}$$

Thus, we can now use the derived transfer function of the controlled system to regulate the current, and through this, influence the DC link voltage. The subsequent sections provide a detailed explanation of the control structure and the tuning of the required parameters. According to Teodorescu et al. (2011), a cascaded voltage and current control structure is sufficient and robust enough to regulate the DC-link voltage, by controlling the grid voltage/current as shown in the equations above [40]. A schematic overview of the control structure is given in Fig. 2.11, with a detailed view on the signal routing displayed in Fig. 2.12. The overview clearly shows the cascaded control structure with a current control in the inner loop and the voltage controller as the outer loop. The resulting voltage set points are then used in the PWM to generate the correct switching signals $S_{1..6}$. In the detailed control block diagram in Fig. 2.12 the *Park* transformation and its inverse is illustrated by the abc/dq0 and dq0/abc blocks respectively. The transformation is applied to current and voltage measurement (i_{abc},v_{abc}) as well as the v_{dq0}^* set points, using the estimated angle θ provided by the PLL in the top left. The outer loop of the controller only consists of one voltage controller (PI) for v_{dc}, with the object to minimize the DC link voltage error and calculating the needed current set point i_{d}^*. The inner loop consists of two PI controllers, for d and q currents, respectively. Additionally, it can be seen that the current control loop contains a feed-forward decoupling based on the ωL and respective current set points,

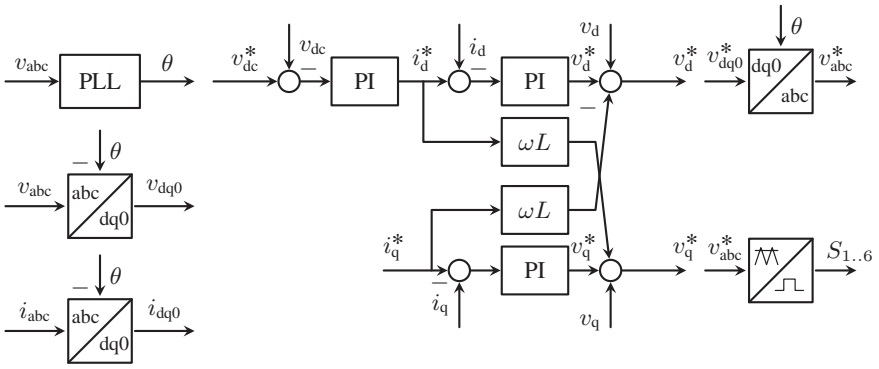

Figure 2.12: Block diagram of the AFE control structure.

where the set point i_q^* is set to 0 by default, unless any reactive power control is desired. This decoupling eliminates the coupling terms created by the *Park* transformation as seen in Eq. (2.17). With the current controller computing the voltage set point v_{dq}^*, the efficiency and speed of it is increased by introducing an additional feed-forward path, which uses the measured voltage v_{dq}. The subsequently transformed voltage set points v_{abc}^* are then used in the PWM to generate the switching signals $S_{1..6}$.

2.3.2.1 Current Control

The current control loop design is performed in the Laplace domain based on the transformed equations in Eq. (2.19). As demonstrated by Yazadni and Iravani (2010), pre-controlling multiple terms of the transfer function can simplify the control structure and most importantly the tuning procedure [39]. In this case the counter voltage e and the coupling terms shown in Eq. (2.19) can be neglected, due to the feed-forward control paths. This yields the following simplified Laplace-domain transfer functions:

$$sLi_d(s) = -Ri_d(s) + v_d(s) \tag{2.23}$$

$$sLi_q(s) = -Ri_q(s) + v_q(s) \tag{2.24}$$

Here, $v_d(s)$ and $v_q(s)$ are the control variables for the voltage at the VSC terminals in the Laplace domain. By decoupling the cross-coupling terms through feed-forward compensation, the plant reduces to a simple first-order system. To compensate this system behavior, a widely used

Proportional Integral (PI) controller designed in the Laplace domain is sufficient. The transfer function of a PI controller is:

$$K_{\mathrm{PI}}(s) = K_{\mathrm{p}} + \frac{K_{\mathrm{i}}}{s} = K_{\mathrm{p}} \cdot \left(1 + \frac{1}{sT_{\mathrm{i}}}\right) \tag{2.25}$$

with K_{p} representing the proportional gain and K_{i} the integral gain. The resulting closed loop block diagram of the d current component is visualized in Fig. 2.13, showing three different blocks. Starting clockwise in the top left corner, the controller is first, next is a delay block representing the delay introduced by the PWM and the converter reaction time, followed by a first order element corresponding to the actual current plant model, based on the connection impedance. i_{d}^*, as the set point for the current, is calculated by the overlaid voltage controller, explained in the next section. The current controller for the q-component has the same structure, with the difference that the current set point i_{q}^* needs no calculation, because no reactive power is transferred and thus the set point is $i_{\mathrm{q}}^* = 0$. In this scenario the q current needs to be kept at zero, but for other applications or services where the reactive power plays an important role the q current loop can be used accordingly.

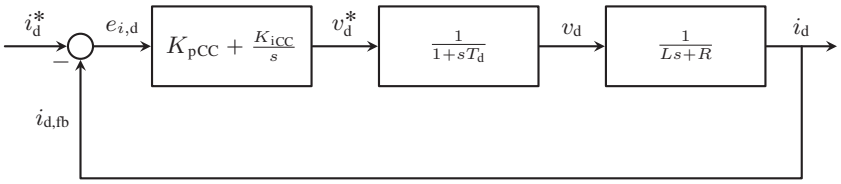

Figure 2.13: Closed-loop current control.

2.3.2.2 Voltage Control

To simplify things, the current control loop as shown in Fig. 2.13 can be approximated by a first order lag element, with the time constant of the current control loop T_0 [39, 41]. The resulting system now consists of the voltage controller, the first order current control transfer function and the integrating behavior of the DC-link capacitor C_{dc}, forming the closed loop shown in Fig. 2.14. Similar to the current controller, the voltage controller is a PI controller with the same mathematical relation, shown in Eq. (2.25).

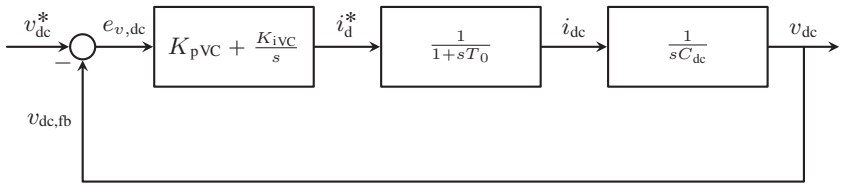

Figure 2.14: Closed-loop voltage control.

2.3.2.3 Control Parameters

In order to have an inner current control loop without a steady-state error, the controller is chosen in such a way that the resulting closed loop behavior has a first order response, as in:

$$\frac{i_{\mathrm{d}}(s)}{i_{\mathrm{d}}^{*}(s)} = \frac{1}{1+sT_0} \tag{2.26}$$

This follows the principal to compensate the plant time constant $T_{\mathrm{p}} = \frac{L}{R}$, with the time constant of a PI controller, as shown in Eq. (2.25) [40, 41]. The type of controller (PI) is chosen using the open-loop transfer function, neglecting the delay and dead time elements. Therefore, the plant model in combination with the controller, can be described as follows:

$$K_{\mathrm{p}} \cdot \left(1 + \frac{1}{sT_{\mathrm{i}}}\right) \cdot \frac{1}{R} \cdot \frac{1}{1+sT_{\mathrm{p}}} \stackrel{!}{=} \frac{1}{sT_0} \tag{2.27}$$

The following desired time constant T_0 is chosen by including the previously ignored delays.

Since the delays are all comparably small they can be lumped together and be approximated with a single first order transfer function, as in Eq. (2.28). The following time constants are considered and expressed with respect to the control period T_{s}:

- $T_{\mathrm{d,ctrl}} = 0.5 \cdot T_{\mathrm{s}}$: representing the control cycle delay.
- $T_{\mathrm{d,PWM}} = 0.5 \cdot T_{\mathrm{s}}$: representing the delay of the PWM (triangular carrier) which is modulating the output switching signals.
- $T_{\mathrm{d,avg}} = 0.5 \cdot T_{\mathrm{s}}$: representing the delay for the measurement averaging the current and voltage values.

The above mentioned delays can be summed up as follows:

$$\frac{1}{1+sT_{\mathrm{d,ctrl}}} \cdot \frac{1}{1+sT_{\mathrm{d,PWM}}} \cdot \frac{1}{1+sT_{\mathrm{d,avg}}} \approx \frac{1}{1+s\left(T_{\mathrm{d,ctrl}} + T_{\mathrm{d,PWM}} + T_{\mathrm{d,avg}}\right)} = \frac{1}{1+sT_{\mathrm{d}}} \tag{2.28}$$

The open loop functions in Eqs. (2.27) and (2.28), with the delays approximated as a first order element, combine to the following second order closed loop current control transfer function:

$$\frac{i_{\mathrm{d}}(s)}{i_{\mathrm{d}}^{*}(s)} = \frac{1}{(sT_0)\cdot(1+sT_{\mathrm{d}})+1} = \frac{1}{1+sT_0+s^2T_0T_{\mathrm{d}}} \tag{2.29}$$

There are multiple ways to determine the right parameters to accomplish a suitable time constant T_0. Some use a coefficient comparison with an optimization of the right damping [41], or one can choose the bandwidth $\omega_0 = 2\pi \cdot f_0$ of the controller by means of Eqs. (2.30) and (2.31), as suggested in [40]. For the following parameter calculation, the commonly applied Betragsoptimum (BO) suggests the choice of $T_0 = 2T_{\mathrm{d}}$ [42]. This leads to the following simplifications, with a summary of all calculated parameters of the current and voltage controller shown in Table 2.2.

$$K_{\mathrm{iCC}} = \frac{1}{T_i} = \frac{1}{T_{\mathrm{p}}} = \frac{R}{L} \tag{2.30}$$

$$K_{\mathrm{pCC}} = \frac{T_i R}{T_0} = \frac{L}{2T_{\mathrm{d}}} \tag{2.31}$$

With the current control parameters derived, one aims to approximate a first order transfer function of the whole current control loop, as seen in Fig. 2.14. The equivalent current controller time constant is denoted as T_0, but can be neglected in the following consideration, since we assume a much smaller bandwidth for the voltage control loop, compared to the current control loop. The open-loop transfer function can subsequently be described as follows:

$$G_{\mathrm{OL}}(s) = (K_{\mathrm{pVC}} + \frac{K_{\mathrm{iVC}}}{s}) \cdot \frac{1}{sC_{\mathrm{dc}}} \tag{2.32}$$

This allows the tuning of the bandwidth ω_{BW}, given $s = j\omega_{\mathrm{BW}}$, to:

$$|G_{\mathrm{OL}}(j\omega_{\mathrm{BW}})| = 1 \tag{2.33}$$

and the phase margin ϕ_{VC} of the voltage control loop, to:

$$\angle G_{\mathrm{OL}}(j\omega_{\mathrm{BW}}) = -180 + \phi_{\mathrm{VC}} \tag{2.34}$$

The missing parameters for the voltage controller can be tuned choosing the phase margin ϕ_{VC} and bandwidth ω_{BW} to allow a sufficiently fast response, while maintaining the stability [40, 41]. The bandwidth is selected as a fraction of the grid frequency to ensure adequate response while maintaining stability:

$$\omega_{BW} = 0.8\pi f_{grid} \tag{2.35}$$

The proportional gain is calculated using the phase margin ϕ_{VC} and the capacitance C_{dc}:

$$K_{\mathrm{pVC}} = \omega_{\mathrm{BW}} \cdot C_{\mathrm{dc}} \cdot \sqrt{\frac{\tan^2(\phi_{\mathrm{VC}})}{1 + \tan^2(\phi_{\mathrm{VC}})}} \tag{2.36}$$

The integral gain is derived from the proportional gain and the phase margin relationship:

$$K_{\mathrm{iVC}} = K_{\mathrm{pVC}} \cdot \frac{\omega_{\mathrm{BW}}}{\tan(\phi_{\mathrm{VC}})} \tag{2.37}$$

A smaller phase margin leads to a faster controller response but may reduce stability margins, while a larger phase margin provides better stability at the cost of slower response. To balance between fast response and adequate stability, the phase margin has been set to $\phi_{\mathrm{VC}} = 60^\circ$ and the bandwidth to $\omega_{\mathrm{BW}} = 0.8\pi \cdot 50\,\mathrm{Hz} = 125.66\,\mathrm{rad/s}$. In Fig. 2.15 an exemplary bode plot for the open loop transfer function of the voltage control, with the specified phase margin and bandwidth, can be seen.

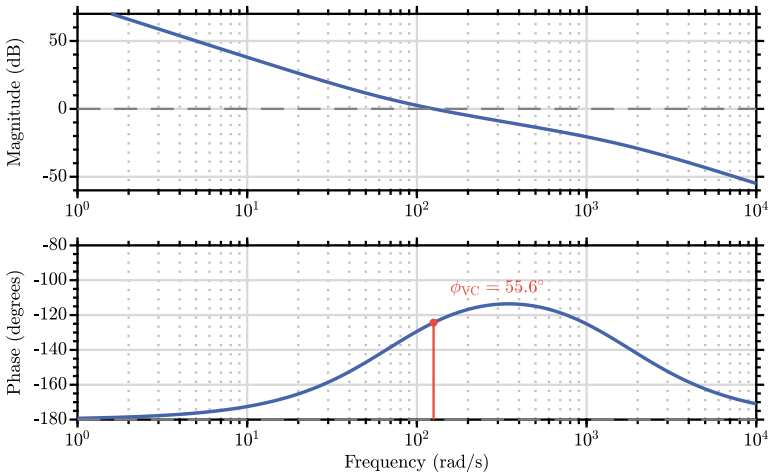

Figure 2.15: Bode plot of the open-loop voltage control transfer function, including the remaining phase margin (ϕ_{VC}).

In the bode plot in Fig. 2.15, a phase margin of effectively 55.6° is achieved, which can still be considered acceptable for a stable operation and fast response. The plant and the calculated control parameters are displayed in Table 2.2, with f_{s} being the switching frequency and T_{s} the computation time step.

Table 2.2: Primary side parameter.

Parameter	Value	Parameter	Value
C_{dc}	3.0 mF	K_{pCC}	16
L	950 μH	K_{iCC}	900
R	54 mΩ	K_{pVC}	0.326
T_{s}	20 μs	K_{iVC}	23.69
f_{s}	50 kHz	ϕ_{VC}	60°

2.3.3 Grid-forming - Virtual Synchronous Machine

In the downstream facing (secondary) converter of the asynchronous connection, a grid-forming control algorithm is deployed to provide a stable and reliable power supply, with additional features such as active power flow control. The controller is based on the general concept of the Virtual Synchronous Machine (VSM) and provides the following features:

- Function as a grid-forming node, providing a stable power supply to the grid.
- Regulate active power consumption/generation based on main grid requirements, without requiring additional communication infrastructure.

The VSM deployed was inspired by the Ise-Lab structure which is a simple swing equation based controller, that was enhanced with an underlying cascaded voltage and current controller, displayed in Fig. 2.16 [43]. This control method was chosen to enable a reliable grid-forming capability paired with the feature to adjust the frequency and voltage set points, without introducing much more complexity.

2.3.3.1 Virtual Synchronous Machine

The general idea of a VSM is to use parts of the mathematical description of a synchronous machine to emulate its behavior [44, 45]. This can be done with different degrees of complexity using n-order models [46]. Complexity, in this case, does not necessarily bring more advantages since a synchronous machine's natural behavior is not always advantageous to a specific application. Therefore, the Ise-Lab structure reduces the synchronous machine model to a second-order model, using mainly the swing equation in Eq. (2.38) [43].

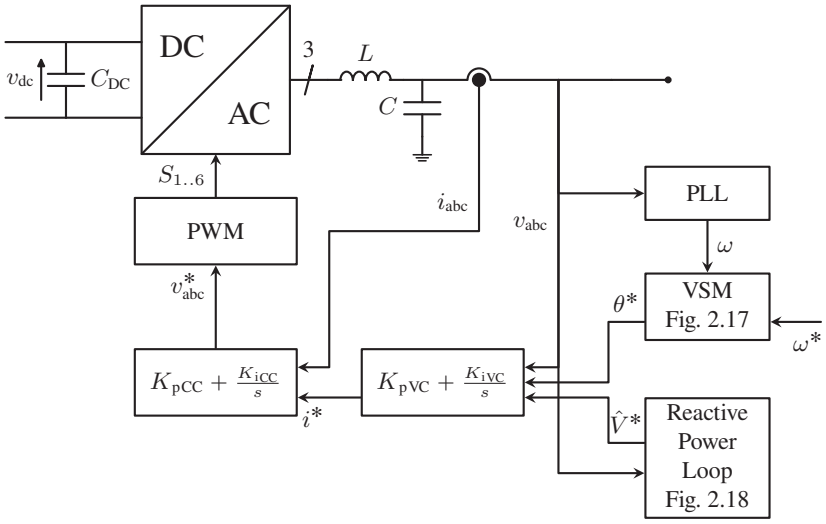

Figure 2.16: Schematic view of a grid-forming control structure, showing the general signal routing using a VSM algorithm.

The swing equation is formulated in the time domain and describes the interaction of a possible power imbalance between the mechanical power P_{m} and the electrical power P_{el}, and the change in angular velocity ω depending on the moment of inertia J and damping coefficient D_{p}. In a real synchronous machine, J is related to the physical nature, such as weight and geometry of the rotor of a synchronous machine. The advantage of a VSM is the shift of physical constraints away from the rotor geometry. Thus, the moment of inertia can be chosen outside the physically possible boundaries. Nevertheless, the control parameters have to be tuned carefully due to other physical constraints of the converter, e.g., the amount of energy stored in the capacitor and its over-current capacity. The damping D_{p} represents the static frequency droop coefficient and has little to no effect during transients. The reduced order model is displayed in the following equation, where nominal angular velocity is represented by ω_0.

$$P^* - P_{\mathrm{el}} = J\omega_0\dot{\omega} + D_{\mathrm{p}}\omega \tag{2.38}$$

This time-domain swing equation is connected with the underlying cascaded voltage and current controllers, which, as described previously, are designed in the Laplace domain. The power calculation P_{el} is performed using instantaneous measurements in the time domain, while the resulting frequency deviation drives the angle generation for the voltage reference in the dq transformation.

The basic VSM block diagram is illustrated in Fig. 2.17. Eq. (2.38) is clearly represented by the inertia and damping variables with subsequent integration of the angular velocity to compute the angle θ. The controller is enhanced with a governor model (here PI), that calculates the power set point for the swing equation to control the frequency to the nominal value of 50 Hz by feeding the frequency from the PLL into a PI controller.

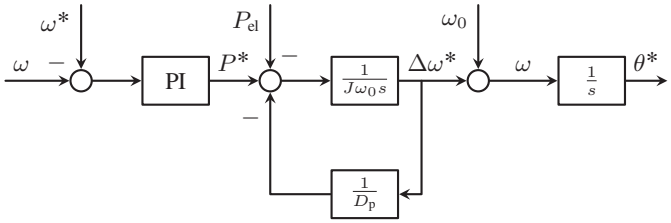

Figure 2.17: Detailed view of the VSM control structure, illustrating the mathematical representation of the active power loop, responsible for the frequency response.

The calculation of the angle θ is generally denoted as the active power loop, since in transmission systems, the frequency is directly related to the active power flow. This is only partly true for low voltage distribution systems, due to higher resistive characteristics of that system. For simplicity and consistency with the literature we will still call this control loop the active power loop, while the following voltage control loop in Fig. 2.18 is denoted the reactive power loop.

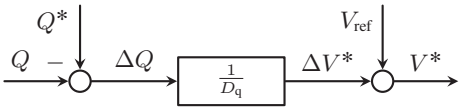

Figure 2.18: Detailed view of the VSM control structure, illustrating the mathematical representation of the reactive power droop.

The reactive power loop is a simple droop controller, adjusting the voltage set point based on the reactive power error.

2.3.3.2 Current Control

In the underlying controller of Fig. 2.16, the current control loop forms the inner part of a cascaded voltage and current control loop. Its primary objective is to regulate the current injected by the converter into the grid, ensuring fast and stable tracking of the reference current provided by the outer voltage control loop. The current controller is typically implemented in the rotating dq reference frame using PI controllers for both d and q axes.

The control structure is identical with the current controller on the primary side, for the AFE controls. As can be seen in Fig. 2.19, which represents one of the two control paths, here the d-axis path is illustrated.

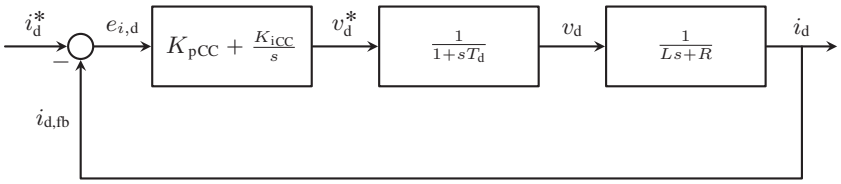

Figure 2.19: Grid-forming current control loop block diagram showing the cascaded PI controller, delays, and plant model.

2.3.3.3 Voltage Control

The voltage control loop forms the outer part of the cascaded control structure. Its main function is to regulate the AC output voltage at the point of common coupling (PCC) to match a given reference, thus enabling the inverter to establish and maintain grid voltage and frequency.

Here the voltage controller is also implemented in the dq reference frame, typically using PI controllers for both d and q axes, but other alternatives exist such as proportional resonant (PR) controllers in $\alpha\beta$ reference frame [40]. The plant model for the voltage control loop is considering the grid connection filter capacitor, where C_{f} is the filter capacitance. The whole block diagram of the voltage loop is illustrated in Fig. 2.20. The inner current control loop can again be approximated by a first order delay with the time constant T_0.

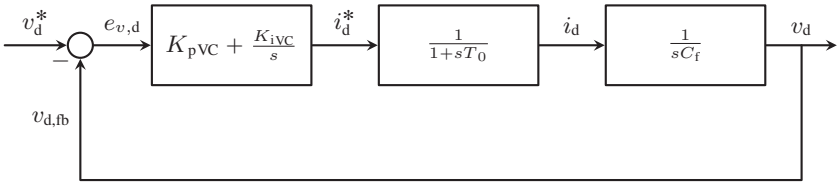

Figure 2.20: Grid-forming voltage control loop block diagram showing the outer voltage controller, equivalent current loop delay, and capacitive plant model.

In practice, the d- and q-axis voltage controllers may include decoupling terms to reduce cross-coupling effects, allowing for more independent control of each axis. The voltage control loop provides the current references for the inner loop, ensuring that the output voltage remains stable and meets the grid-forming requirements, even under varying load conditions.

2.3.3.4 Control parameters

The control parameters for the grid-forming converter are determined through systematic tuning procedures that ensure stable operation and good dynamic performance. The procedure is similar to the tuning of the active-front end controller, but with additional considerations and the active and reactive power control layer for the grid-forming functionality.

The grid current components are controlled by two PI controllers in the grid-synchronous frame (dq) using the same technique as introduced in previous current control section. Therefore the controller parameters are chosen to achieve a first-order response, compensating the plant time constant and accounting for delays. The transfer function of the plant and converter model is given by:

$$G_{plant}(s) = \frac{1}{1 + sT_{\mathrm{d}}} \cdot \frac{1}{R + sL} \tag{2.39}$$

The control parameters K_{pCC} and K_{iCC} are tuned using the same *BO* criterion as in the GFL controller. Considering the plant model above and the parameters L, R and T_{d}, the parameters can be calculated as follows:

$$K_{\mathrm{iCC}} = \frac{R}{2T_{\mathrm{d}}} = \frac{R}{L} \tag{2.40}$$

$$K_{\mathrm{pCC}} = \frac{L}{2T_{\mathrm{d}}} \tag{2.41}$$

The parameter T_{d} again represents the sum of all the small delays in the system, and is approximated with $T_{\mathrm{d}} = 1.5 \cdot T_{\mathrm{s}}$, where T_{s} is the control period of the system.

The voltage controller for the GFM converter is tuned using the *Symmetrical Optimum* method, a widely adopted method to achieve a good trade-off between fast set point tracking and disturbance rejection [42]. The control parameters are defined by the desired bandwidth, which are tuned by the time constant $T_{\mathrm{d,eq}}$ and the pole placement, using parameter a.

$$K_{\mathrm{pVC}} = C_{\mathrm{f}}/(a \cdot T_{\mathrm{d,eq}}) \tag{2.42}$$

$$K_{\mathrm{iVC}} = K_{\mathrm{pVC}}/(a^2 T_{\mathrm{d,eq}}) \tag{2.43}$$

For a sufficiently high disturbance rejection, $T_{\text{d,eq}}$ the equivalent delay of the closed-loop current controller transfer function is defined as:

$$T_{\text{d,eq}} = 10T_{\text{d}} \tag{2.44}$$

The choice of a can lead to a higher overshoot with a faster system response for low values of a, whereas a high value of a can result in better damping, but slower system response. a is typically kept within the range of 2 to 4. A value of $a = 2$ provides an acceptable balance between rapid response and minimal overshoot. The parameter a can be calculated based on the desired phase margin ϕ_{VC} to ensure stability and proper damping characteristics:

$$\phi_{\text{VC}} = \frac{\phi_{\text{VC,deg}}}{360} \cdot 2\pi \tag{2.45}$$

$$a = \frac{1 + \sin(\phi_{\text{VC}})}{\cos(\phi_{\text{VC}})} \tag{2.46}$$

where $\phi_{\text{VC,deg}}$ is the desired phase margin in degrees (typically between 40° to 60°) and ϕ_{VC} is the phase margin in radians. This formulation ensures that the closed-loop system maintains adequate stability margins while providing satisfactory transient response.

Tuning the active and reactive power loops, is less straight forward since there is no established best practice to tune a virtual synchronous machine, yet.

Rathnayake et al. in 2022 proposed a methodology that mathematically combines the damping and inertia parameters displayed in Fig. 2.17 to the following transfer function, which provides a so-called inertial time constant τ_J. This can be used to design the VSM control parameters [47]. The transfer function is given by:

$$G_{\text{vsm}}(s) = \frac{D_{\text{p}}}{\tau_J s + 1} \tag{2.47}$$

where τ_J can be designed using the following metrics:

$$\tau_J = \frac{D_{\text{p}}}{\rho} P_{max} \tag{2.48}$$

The maximum allowed RoCoF is typically imposed by the transmission system operator (TSO) and therefore can change depending on the location. The maximum RoCoF ρ is set to 1 Hz/s for

the maximum active power P_{max}. For a given maximum RoCoF ρ, the value of the corresponding minimum virtual inertia J that complies with the imposed limit can than be derived as:

$$J = \frac{\tau_J}{D_{\text{p}} \cdot \omega_0} = \frac{\frac{D_{\text{p}}}{\rho} \cdot P_{\text{max}}}{D_{\text{p}} \cdot \omega_0} = \frac{0.5}{D_{\text{p}} \cdot \omega_0} = 9.12\ \text{kg} \cdot \text{m}^2 \tag{2.49}$$

The damping coefficient D_{p} is set to 0.5 Per Unit (p.u.) based on the maximum allowed stationary frequency deviation.

Table 2.3: Grid-forming converter control parameters.

Parameter	Value	Parameter	Value
L	950 μH	K_{pCC}	15.83
R	54 mΩ	K_{iCC}	900
C_{f}	12.9 μF	K_{pVC}	0.02
T_{s}	20 μs	K_{iVC}	14.53
f_{s}	50 kHz	ω_0	314 rad/s
ρ	1 Hz/s	P_{max}	18 kW
J	9.12 kgm^2	D_{p}	0.5 p.u.
a	2.14	ϕ_{VC}	45°

3 Models and Testbenches to test Asynchronous Grid Connections

This chapter addresses *Research Question 2 (RQ2)* by developing and validating suitable testing methodologies for the performance and impact of ASG systems. The CHIL and double PHIL configurations presented here, constitute *Key Contributions KC3* and *KC4*, enabling rigorous experimental validation that bridges laboratory testing with real-world grid conditions while managing computational complexity.

3.1 Power Electronic Modeling

The previously introduced power electronic systems can be modeled with different degrees of detail. The degree of detail can range from modelling each semiconductor switch individually, including detailed switching behavior, to the simple representation of the averaged voltage and current output of a converter. This work mainly deploys simplified so-called average models which can mimic the behavior of power electronic systems in specific scenarios and most importantly reduce the needed computational burden significantly. Detailed simulations models were only used for the initial controller testing and as pre-test for the experimental validation, e.g. in a CHIL setup.

3.1.1 Switching Modeling

A detailed converter switching model is usually based on a combination of low-level sub-models representing the switching behavior of each semiconductor module. They are usually represented by switches as illustrated in Fig. 3.1a, where each switch has a mathematical representation. Depending on the degree of detail, a switch can be represented including all of it surrounding circuitry such as diodes and gate drive units, or using a simplified approximation, that considers an off and on resistance (R_{on} and R_{off}) as shown in Fig. 3.1b. The general concept is to have a sufficiently accurate but still computationally light representation of the semiconductor's on

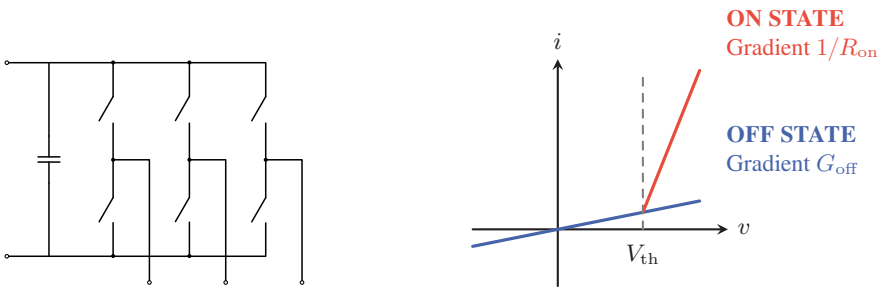

Figure 3.1: Illustration of an ideal converter model with switches is shown in a) and a diagram of the switching behavior of a semiconductor model is displayed in b).

and off state and the transition between them. The computation of the current flow through the conductor for an ideal switching model can be described with the following pseudocode:

```
if (v>Vth) AND (Gate Signal is High)
  i = (v - Vth*(1-Ron*Goff))/Ron
else
  i = v*Goff
end
```

where, V_{th} represents the threshold voltage of the semiconductor module. The typical values for the threshold voltage ranges between 3 and 5 V. $1/R_{\text{on}}$ (red graph) is the on-state resistance, with typical values in the range of 10 to 100mΩ. The off-state conductance (blue graph) G_{off}, is typically very low, in the range of a few μS which results in leakage currents in the low μA range. The switch is turned on or off depending on the gate signal input. In case the voltage across the switch (v) exceeds the threshold voltage and the gate signal is high, the current (i) is calculated using the on-state resistance. Otherwise, the current is calculated using the off-state conductance.

This mimics the general behavior for semiconductor on and off states, but does leave out the detailed modeling of the diode reverse recovery behavior. This behavior is particularly relevant to studies with a focus on transients and losses in the $< \mu$s time range, but due to the following analysis being focused on time scales in the ms-s range, it is not considered here. Nevertheless, the earlier introduced two level converter in a back-to-back configuration, needs 6 of these ideal switches to emulate one full converter stage, which makes 12 switches in total for the whole B2B system.

Knowing this, the modeling of a switching converter is performed along the lines of the system already described in Chapter 2, therefore the focus here is put on the design of average models for converter systems and specifically for the previously introduced B2B system.

3.1.2 Average Modeling

Average models are particularly important for the simulation of power systems and their interaction with power electronics. Particularly simulations with large numbers of power electronic systems, limited computational power available or long time spans to be simulated. An average model is a simplified representation of the converter behavior at the output terminals, with the same average voltage and current relationship (over one switching period) on the AC and DC side as a switching model. It can be executed using larger time steps, while still allowing the assessment of saturation effects or over-modulation. The controller for the average model can be modelled in the exact same way as for switching models, except the gate signal modulation is not required.

The following section will describe the modeling of a B2B using average models, based on the Ideal Transformer Method (ITM). The ITM is used to interface two or more decoupled circuits with each other. Its core functionality is the establishment an interface algorithm enabling the power exchange between the circuits or models. This can be applied to interface physical measurements with simulation models or simulation models of DC and AC domain with each other.

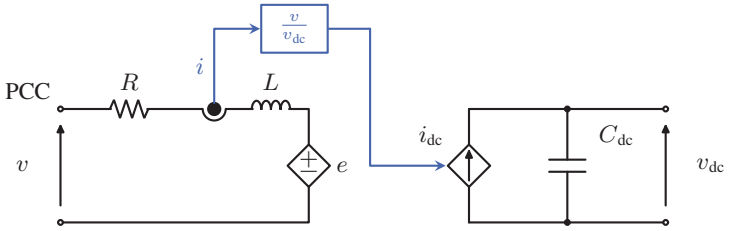

Figure 3.2: Conceptual diagram of the ITM interfacing AC and DC circuit models through instantaneous power balance. The current is measured on the AC side and the voltage ratio between both sides is used to calculate the DC-side current source set point.

The ITM is based on the principle of instantaneous power conservation, where the total power flow between the AC and DC side of a converter is calculated algebraically in the time domain, as illustrated in Fig. 3.2. This algebraic power relationship is then used to determine controlled current or voltage sources that couple the AC and DC circuits. In the example a current type ITM is shown, where the current on the AC side is measured and used to calculate the DC side current source set point (blue path). The calculation is simply preserving the same instantaneous power

on both sides of the ITM, assuming lossless operation ($P_{\text{ac}}(t) = P_{\text{dc}}(t)$) to reduce complexity. Thus, the i_{dc} set point here is calculated as:

$$i_{\text{dc}}(t) = \frac{P_{\text{ac}}(t)}{v_{\text{dc}}(t)} = \frac{v(t) \cdot i(t)}{v_{\text{dc}}(t)} \tag{3.1}$$

3.1.2.1 Average Model Primary Side Converter

The primary side converter is modeled by controlled voltage sources connected to the grid through a series grid impedance. A single phase representation is shown in Fig. 3.3, the circuit consists of the grid voltage v_1 at the point of common coupling (PCC 1). The PCC is connected through the series impedance (R_1, L_1) to the controlled voltage source e_1 representing the converter terminals, where the i_1 represents the current absorbed or injected by the converter.

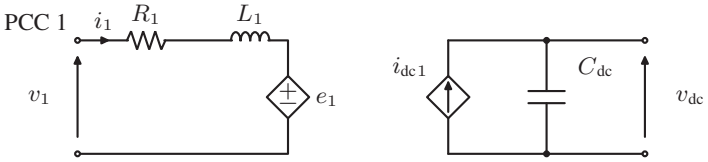

Figure 3.3: Average primary side converter model.

Circuit Description

Applying KVL to the AC circuit in Fig. 3.3, the relationship between the PCC voltage v_1, the average converter voltage e_1, and the current i_1 through the grid impedance is:

$$v_1(t) = e_1(t) + R_1 i_1(t) + L_1 \frac{di_1(t)}{dt} \tag{3.2}$$

Rearranging to express the current dynamics:

$$\frac{di_1(t)}{dt} = \frac{1}{L_1} \left(v_1(t) - e_1(t) - R_1 i_1(t) \right) \tag{3.3}$$

This equation represents the voltage drop across the grid impedance in the time domain, where the converter voltage $e_1(t)$ is determined by the control algorithm and modulation process, averaged over the switching period.

Power Coupling to DC Side

On the right side of Fig. 3.3 the DC coupling between AC and DC is illustrated with a controlled current source which injects a current based on the total three-phase power flow of the AC side circuit.

The instantaneous power per phase is calculated from the measured voltages and currents at the primary converter terminals and subsequently summed to obtain the total three-phase power:

$$P_{\text{ac}1}(t) = \overbrace{v_{1,a}(t) \cdot i_{1,a}(t)}^{p_{1,a}(t)} + \overbrace{v_{1,b}(t) \cdot i_{1,b}(t)}^{p_{1,b}(t)} + \overbrace{v_{1,c}(t) \cdot i_{1,c}(t)}^{p_{1,c}(t)} \tag{3.4}$$

This power calculation is an algebraic operation performed on instantaneous voltage and current values in the time domain. The calculated power flow is subsequently fed to the DC circuit model, where applying Kirchhoff's Current Law (KCL) at the DC link node yields:

$$i_{\text{dc}1}(t) + i_{\text{dc}2}(t) = C_{\text{dc}} \frac{dv_{\text{dc}}(t)}{dt} \tag{3.5}$$

where $i_{\text{dc}1}$ is the current source representing the primary side power flow, $i_{\text{dc}2}$ represents the secondary side, and C_{dc} is the DC link capacitance.

The current $i_{\text{dc}1}$ is determined by dividing the total AC power $P_{\text{ac}1}$ by the DC link voltage (v_{dc}), implementing the instantaneous power balance of the ITM:

$$i_{\text{dc}1}(t) = \frac{P_{\text{ac}1}(t)}{v_{\text{dc}}(t)} \tag{3.6}$$

This algebraic relationship ensures power conservation across the AC-DC interface, with losses neglected in this ideal average model.

3.1.2.2 Average Model Secondary Side Converter

The LV converter is represented by controlled voltage sources for each phase connected to the grid via an LC output filter. As shown in Fig. 3.4, the secondary side circuit consists of a controlled voltage source e_2, series impedance (R_2, L_2), and a parallel LC damping filter (C_{f}, R_{f}) connected to the point of common coupling (PCC 2).

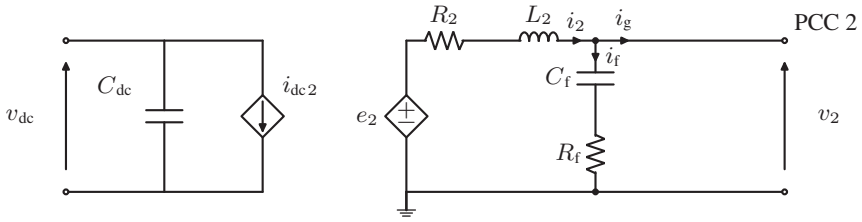

Figure 3.4: Average secondary side converter model.

Circuit Description

Applying KVL to the main loop from the voltage source to the output terminal yields:

$$e_2(t) = R_2 i_2(t) + L_2 \frac{di_2(t)}{dt} + v_2(t) \tag{3.7}$$

where e_2 is the controlled voltage source output, i_2 is the inductor current, and v_2 is the output voltage at PCC 2.

Applying KCL at the filter connection node:

$$i_2(t) = i_f(t) + i_g(t) \tag{3.8}$$

where i_f is the current through the filter capacitor branch and i_g is the output current to the grid.

For the parallel damped capacitor branch, the current-voltage relationship is:

$$i_f(t) = C_f \frac{dv_2(t)}{dt} \tag{3.9}$$

assuming the damping resistor R_f is negligible or sufficiently small compared to the reactance at the frequencies of interest.

Substituting Eq. (3.8) into Eq. (3.9):

$$C_f \frac{dv_2(t)}{dt} = i_2(t) - i_g(t) \tag{3.10}$$

The coupled system can be expressed as a set of first-order differential equations with state variables $x = [i_2, v_2]^T$:

$$\frac{di_2(t)}{dt} = \frac{1}{L_2}\left(e_2(t) - R_2 i_2(t) - v_2(t)\right) \tag{3.11}$$

$$\frac{dv_2(t)}{dt} = \frac{1}{C_\mathrm{f}}\left(i_2(t) - i_\mathrm{g}(t)\right) \tag{3.12}$$

These equations describe the dynamic behavior of the filter and the output voltage across the capacitor, where the controlled voltage source e_2 drives current through the series RL impedance, which is then split between the filter capacitor and the grid current.

Power Coupling to DC Side

The calculated power and resulting current ($i_{\mathrm{dc}2}$) is used as feedback for the DC stage, shown on the left side of Fig. 3.4. The instantaneous three-phase power transferred from the AC side to the DC link is:

$$P_{\mathrm{ac}2}(t) = v_{2,a}(t)i_{2,a}(t) + v_{2,b}(t)i_{2,b}(t) + v_{2,c}(t)i_{2,c}(t) \tag{3.13}$$

The DC-side current source representing this power transfer is:

$$i_{\mathrm{dc}2}(t) = \frac{P_{\mathrm{ac},2}(t)}{v_{\mathrm{dc}}(t)} \tag{3.14}$$

3.2 Power System Modeling

This section describes two power system models used in the process of simulation and validation of the ASG. For fast performance and the emulation of a transmission grid based on large synchronous machines, the Single Machine Model (SMM) of Kundur et al., has been deployed [48]. On the distribution grid level a more detailed model was needed to allow the investigation of new grid-forming and power flexibility algorithms, which is provided by the CIGRE LV benchmark network [49].

3.2.1 Single Machine Model

To investigate the impact of the active power flow control on the main grid, a simplified power system model is used, that mimics the frequency response based on active power imbalances. To

replicate the general behavior of the power system, the model employs s-domain descriptions of a single equivalent machine, incorporating transfer functions for primary droop control, as well as for system inertia and damping.

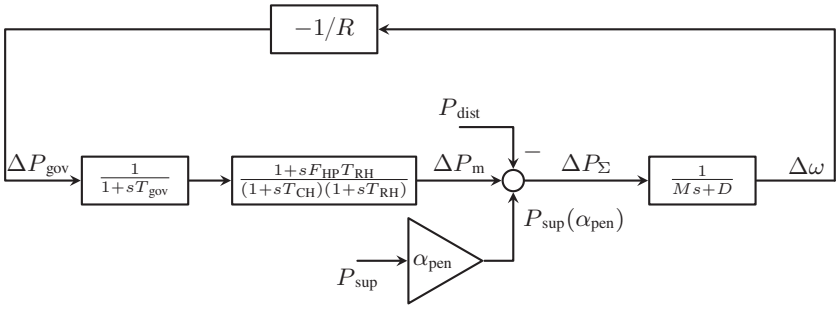

Figure 3.5: Block diagram of the single machine model consisting of speed droop, governor and reheat turbine blocks. The model emulates the frequency response of a large synchronous machine connected to a power system [48].

The complete model, illustrated in Fig. 3.5, is adapted from the single machine framework by Kundur et al. and is composed of a speed droop block in Eq. (3.15), a governor model in Eq. (3.16), and a reheat turbine in Eq. (3.17) [48].

$$\frac{\Delta P_{\text{gov}}}{\Delta\omega} = -\frac{1}{R} \tag{3.15}$$

$$\frac{\Delta Y}{\Delta P_{\text{gov}}} = \frac{1}{1+sT_{\text{gov}}} \tag{3.16}$$

The parameter R establishes the relationship between a variation in angular velocity, $\Delta\omega$, and the subsequent change in power output or valve/gate position, denoted as ΔP_{gov}. Following this, the governor model processes the power deviation ΔP_{gov} to generate a control signal ΔY, which functions as the operational set point for the reheat turbine. The simplified transfer function for the reheat turbine, shown in Eq. (3.17), models this behavior. It incorporates several time constants: T_{CH} for the main inlet volumes and steam chest, and T_{RH} for the reheater. Additionally, it uses F_{HP} to represent the fraction of total power generated by the turbine. This model utilizes the control signal ΔY to produce a corresponding change in the mechanical power output, ΔP_{m}.

$$\frac{\Delta P_{\text{m}}}{\Delta Y} = \frac{1+sF_{\text{HP}}T_{\text{RH}}}{(1+sT_{\text{CH}})(1+sT_{\text{RH}})} \tag{3.17}$$

The central element of the SMM is the summation point, where all power contributions are algebraically combined to determine the net power imbalance ΔP_{Σ}. This summation point

represents the fundamental power balance equation of the system, where the mechanical power input ΔP_{m} from the turbine is balanced against external disturbances and support mechanisms. The total power imbalance is calculated as:

$$\Delta P_{\Sigma} = \Delta P_{\mathrm{m}} - \Delta P_{\mathrm{dist}} + \Delta P_{\mathrm{sup}}(\alpha_{\mathrm{pen}}) \tag{3.18}$$

where ΔP_{dist} represents external power disturbances such as load changes or generation loss, and $\Delta P_{\mathrm{sup}}(\alpha_{\mathrm{pen}})$ represents any frequency support provided by external systems, such as the ASG. The provided power support, can be scaled to account for a specific percentage of support capacity with respect to the total system power. This scaling is defined as:

$$\alpha_{\mathrm{pen}} = \frac{P_{\text{support capacity}}}{P_{\text{total system power}}} = \frac{P_{\text{support capacity}}}{1\,\text{p.u.}} \tag{3.19}$$

representing the penetration percentage with respect to the total system power of the SMM defined as 1 p.u.. I.e., a 5 % penetration value corresponds to a value of α_{pen}=0.05, where a normalized P_{sup} value of e.g., 0.5 p.u. would end up as:

$$\Delta P_{\mathrm{sup}}(\alpha_{\mathrm{pen}}) = 0.5\,\text{p.u.} \cdot 0.05 = 0.025\,\text{p.u.} \tag{3.20}$$

The summation culminates in the overall power imbalance, where a positive power imbalance ($\Delta P_{\Sigma} > 0$) indicates excess generation, leading to a frequency rise, while a negative imbalance ($\Delta P_{\Sigma} < 0$) indicates insufficient generation, resulting in a frequency drop.

A power imbalance induces a variation in the angular velocity, which is equivalent to a frequency deviation, and vice versa. The extent of this deviation is determined by the system's inertia (M) and damping (D) parameters, as represented by the following transfer function:

$$\frac{\Delta\omega}{\Delta P_{\Sigma}} = \frac{1}{Ms + D} \tag{3.21}$$

The resulting frequency deviation $\Delta\omega$ is then fed to the droop block, but can also be used as a variable to evaluate the frequency response impact of supporting systems such as the ASG. The inputs to the central summation point, P_{dist} and P_{sup}, represent external influences on the power imbalance, e.g., a load or generation disturbance injected at P_{dist} or a frequency supporting response e.g., by the ASG at P_{sup}. The preset parameters for the single machine model are summarized in Table 3.1, where particularly the inertia M is up for change to emulate different degree of inertia in a power system.

Table 3.1: Single machine model parameters.

Parameter	Value	Parameter	Value
R (p.u.)	0.05	F_{HP} (p.u.)	0.3
T_{gov} (s)	0.2	M (p.u.)	4
T_{RH} (s)	7	D (p.u.)	1
T_{CH} (s)	0.3	α_{pen}	[0.01 .. 0.1]

3.2.2 CIGRE LV Benchmark Network

On the secondary side of the ASG a distribution system with more details is used to showcase the capabilities of the ASG to establish a LV grid and meanwhile offer active power flow controllability.

For this purpose the well-known CIGRE LV benchmark network was used and slightly simplified, as illustrated in Fig. 3.6 [49]. The simplification only concerned the amount of busses and lines, while keeping the general structure of the feeder being connected to the upstream grid through a transformer. In addition, active systems such as BESS and PV have been added following the recommendations in the connected CIGRE report [49]. The line parameters are kept in line with the recommendations for EU LV distribution grids, as shown in Table 3.2.

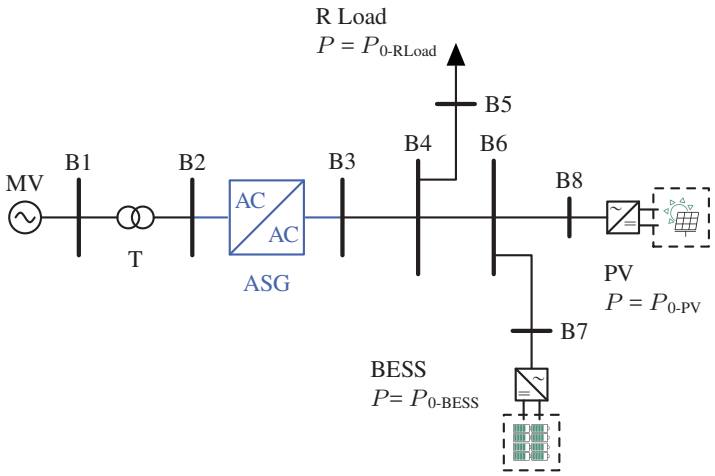

Figure 3.6: A simplified CIGRE LV benchmark network with the ASG as the grid interface to the upstream MV grid. An R Load, a BESS and a PV system are connected to the LV grid. The power set point of these systems can be freely controlled during execution.

The active power set points for the BESS, PV and resistive load can be freely adjusted during simulation to allow the investigation of different operating scenarios. The default values for the active power set points are $P_{0\text{-BESS}}$= 4 kW, $P_{0\text{-PV}}$= 4 kW and $P_{0\text{-RLoad}}$= -12 kW respectively, where a negative sign indicates power consumption.

Table 3.2: Primitive impedance matrix (Ω / km) [49].

Phase	A	B	C
A	0.287+j0.167	0.121+j0.110	0.125+j0.070
B	0.121+j0.110	0.279+j0.203	0.121+j0.110
C	0.125+j0.070	0.121+j0.110	0.287+j0.167

3.3 Validation Setups

The previous chapter described the hardware topologies and control algorithms deployed to establish an ASG. Paired with the models presented in the previous sections the simulation environment to investigate an ASG is fully introduced. To complete the picture, the setups to test and validate the proposed control algorithms and hardware implementation are described in the following.

3.3.1 Controller Hardware-In-the-Loop Setup

For an efficient, safe, fast and accurate verification of the control algorithm and its implementation on the actual controller, a CHIL setup is deployed. The IEEE Standard Association recently approved a new recommended practice (P2004) for Hardware-in-the-loop based testing, which includes the definition for CHIL as follows [50]:

Definition. A Hardware-in-the-loop simulation where one or more Hardware of Interest (HOI) are interfaced at the signal level to a Model of Interest (MOI) where natural coupling is not intended to be preserved.

A generalized CHIL setup is shown in Fig. 3.7. The figure illustrates the connection between the controller, here denoted as HOI and a model to test the control algorithm against. This model runs in real-time on a dedicated real-time simulator, denoted as MOI. In one setup there could be multiple sub-models or sub-hardware to interact with each other. The interaction between

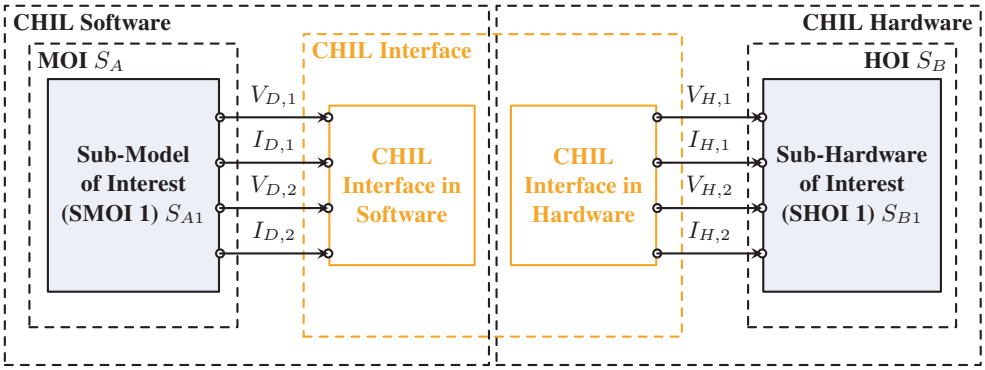

Figure 3.7: Generalized CHIL test architecture showing the interface between software model and hardware controller, adopted from [50].

the HOI and MOI is enabled by an interface, here represented by the yellow dashed box in the center. This interface is usually a combination of Analog Digital Conversion (ADC) and Digital Analog Conversion (DAC) units, e.g., to convert calculated output variables ($V_{D,1}$, $I_{D,1}$, ...) in the real-time simulation (MOI) to an analog signal ($V_{H,1}$, $I_{H,1}$, ...) that can be fed to the sensors and/or inputs of the controller (HOI).

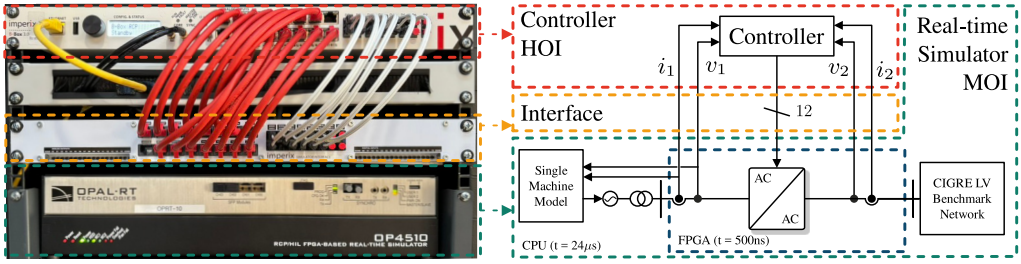

Figure 3.8: CHIL setup at EnergyLab, KIT, showing a real-time simulator (green box) connected to an Imperix BoomBox 3.0 controller hardware (red box) through an IO interface (yellow box).

The actual implementation of the setup is depicted in Fig. 3.8, showing the three main components of the CHIL setup at KIT's EnergyLab. The green and blue box in the bottom center represent the MOI with sub-models in CPU (green) and FPGA (blue) respectively. The red box at the center top represents the HOI, a controller (BoomBox 3.0) from the manufacturer imperix and the yellow box represents the IO interface. All three components are also shown in the real setup on the photo on the left side of the figure.

3.3.1.1 Real-Time Simulation of the B2B Converter

The MOI for the ASG test is running on a real-time simulator from OPAL-RT Technologies, the OP4510. It is based on a co-simulation between a CPU and FPGA model, within the simulator (green and blue box in Fig. 3.8). The FPGA is required to ensure the timely execution of the power electronic switching model, while the CPU runs the connected power system models.

The selection of an appropriate time step for the FPGA-based switching model is critical to ensure accurate representation of both the PWM switching behavior and the resulting AC waveforms. The carrier-based PWM signal generation with a switching frequency of $f_{\text{sw}} = 20\,\text{kHz}$, corresponding to a switching period of $T_{\text{sw}} = 50\,\mu\text{s}$.

To minimize the delay between PWM edge generation and its detection in the real-time simulation, the smallest possible FPGA time step should be selected. The controller hardware (BoomBox 3.0) generates PWM signals with a temporal resolution of 4 ns through its optical fiber outputs. Given this constraint and to ensure minimal detection latency, the implemented time step is chosen as $t_{\text{FPGA}} = 500\,\text{ns}$, which represents the smallest achievable time step on the OP4510 FPGA while maintaining computational feasibility. The OP4510, is designed to only handle a minimum time step of $10\,\mu\text{s}$ in CPU-based models, which necessitates the co-simulation with an FPGA-based model to achieve the required temporal resolution.

This time step provides 100 samples per switching period at 20 kHz:

$$N_{\text{samples}} = \frac{T_{\text{sw}}}{t_{\text{FPGA}}} = \frac{50\,\mu\text{s}}{500\,\text{ns}} = 100 \tag{3.22}$$

This high sampling rate ensures that all switching transitions are captured with minimal latency, which is essential for accurate closed-loop control behavior in the CHIL environment.

Beyond the PWM switching requirements, the selected time step provides excellent resolution for synthesizing the fundamental 50 Hz AC waveforms. With a fundamental period of $T_{\text{fund}} = 20\,\text{ms}$, the number of samples per fundamental period is:

$$N_{\text{fund,FPGA}} = \frac{T_{\text{fund}}}{t_{\text{FPGA}}} = \frac{20\,\text{ms}}{500\,\text{ns}} = 40{,}000 \tag{3.23}$$

This sampling rate ensures that the sinusoidal voltage waveforms after the output filter are represented with high fidelity, enabling accurate analysis of harmonics, power quality metrics, and transient phenomena. The output gate voltages and the resulting filtered AC voltages can thus be computed within the 500 ns time step with sufficiently high temporal and amplitude resolution to represent the physical system behavior accurately.

In the CPU-based model for the power system simulation a time step of $t_{\text{CPU}} = 24\,\mu\text{s}$ is considered sufficient for the accurate representation and capturing of dynamics in the order of milliseconds and higher for the investigation of frequency response and active power control. The 24 μs were needed to accommodate the power system models and the entire control and communication infrastructure to operate the PHIL interface. This led to the following sample number per fundamental frequency cycle:

$$N_{\text{fund,CPU}} = \frac{T_{\text{fund}}}{t_{\text{CPU}}} = \frac{20\,\text{ms}}{24\,\mu\text{s}} \approx 833 \tag{3.24}$$

Of course both time steps need to be chosen in a way that the models running, can be executed within the given time frame, otherwise real-time operation cannot be guaranteed and so-called *overruns* occur.

3.3.1.2 Controller Hardware implementation

The final experimental setup to validate and test the proposed ASG is based on hardware produced by imperix, including power modules, filters, and control hardware. Therefore, the same controller, the BoomBox 3.0 is also deployed in the CHIL setup (top red box in the photo on the left side of Fig. 3.8). The BoomBox 3.0 is a complete Digital Signal Processing unit including ADC, front-panel, communication interfaces and optical fiber output to emit gate signals. It is based on two 1 GHz ARM Cortex-A9 processors and a Kintex 7 125K FPGA to ensure fast and deterministic execution of control algorithms. The programming of the controller can be done by using the *Automated Code Generation* tool including a large Simulink and PLECS library with pre-defined imperix specific blocks or the imperix CPP SDK (C++ Software Development Kit).

The board comes with 16 analog inputs with a 16 bit resolution and a maximum sampling rate of 500 ksps. A set of 16 digital general purpose inputs and outputs respectively and 16 optical fiber outputs (thin black cables on the right side of the Boombox). The optical fiber outputs allow a resolution of up to 4 ns, and are the main interface to emit gate signals to power modules or in the CHIL setup, to the switching model running on the FPGA of the real-time simulator.

3.3.1.3 IO Interface Configuration

There are two reasons that require an additional IO interface (middle yellow box in the photo on the left side of Fig. 3.8) between the real-time simulator and the controller hardware. First, the output voltage and currents of the real-time simulator, which mimic sensor outputs, need to be split and correctly wired to the respective inputs of the controller. The BoomBox 3.0 takes

16 analog signals via RJ45 connectors (red cables in the photo) and the OPAL can emit up to 32 analog output signals via D-SUB connectors. Second, the PWM signals emitted as optical signals from the controller need to be converted to digital signals that can be read by the real-time simulator's digital inputs. For that purpose the dedicated interface panel (in yellow in Fig. 3.8) is offered by imperix to convert the optical signals to digital signals and allow routing them to the real-time simulator with D-SUB connectors.

3.3.2 1 MVA PHIL Setup at EnergyLab

Similar to the CHIL setup, a PHIL setup can be defined along the lines of the recently approved IEEE Standard Association recommended practice (P2004) for Hardware-in-the-loop based testing [50].

Definition. A Hardware-in-the-loop (HIL) simulation where the HOI interacts with the MOI while the natural coupling at the power interfaces that exists in the System of Interest (SOI) is intended to be preserved. The generalized system description of a PHIL setup is shown in Fig. 3.9.

The architecture consist of three main components: the MOI executed within a real-time simulation; the PHIL interface to translate MOI digital variables to the analog domain and vice versa; and the HOI, any kind of hardware that is tested in this setup.

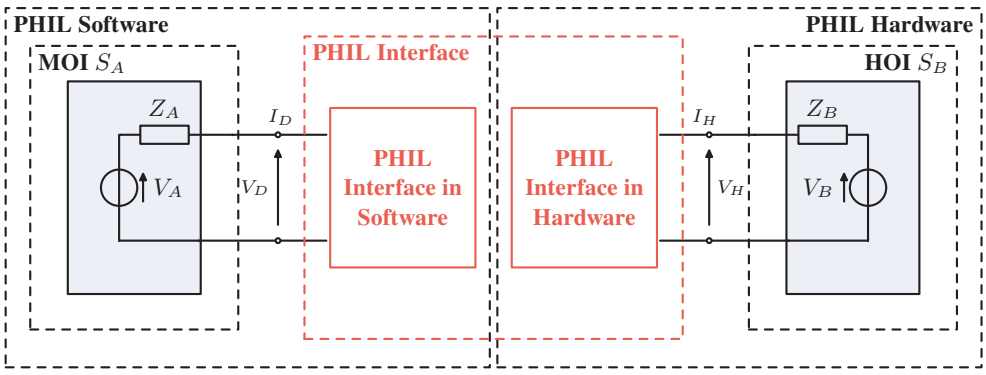

Figure 3.9: Generalized PHIL test architecture showing the interface between software model and hardware under test, adopted from [50].

More specifically the PHIL interface must be able to deliver digital output signals (e.g., V_D in Fig. 3.9) of the MOI as analog signals with sufficient power and convert measured analog values to digital values usable in the MOI (e.g., I_D in Fig. 3.9) to operate in a closed loop.

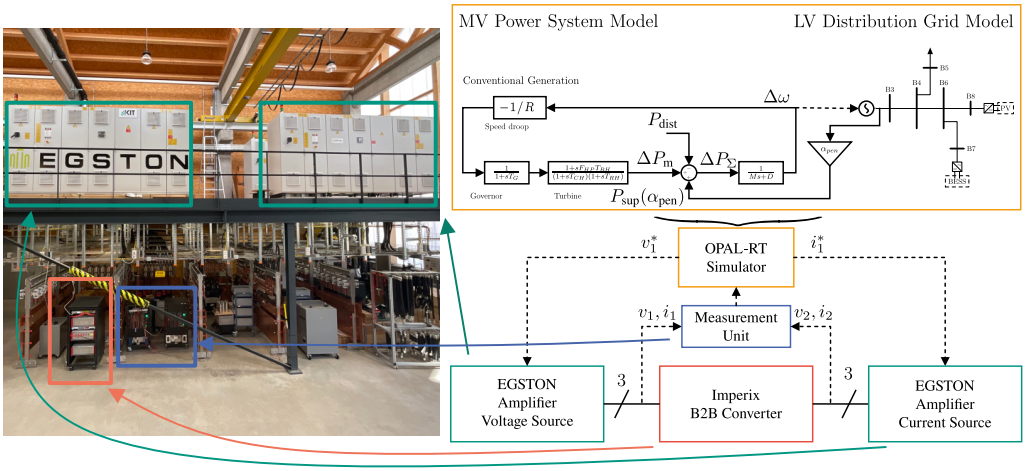

Figure 3.10: Detailed illustration of the 1 MVA PHIL setup at the EnergyLab, KIT, showing the B2B converter interfaced to power amplifiers controlled by the real-time simulator, adopted from [J1].

In detail the PHIL setup in the EnergyLab at KIT is illustrated in Fig. 3.10. The figure displays all major components deployed in the setup shown in the photo on the left side. The right side shows the hardware block diagram. Starting from the bottom right, the power amplifier emulating the LV benchmark grid (right green box) is interfaced as a current source to the B2B hardware in the red box. Subsequently, the B2B is connected to the second power amplifier on the left, which emulates the upstream grid with the SMM and is therefore modeled as a voltage source (left green box). The voltages and currents on both sides of the B2B converter are measured with a central measurement unit (central blue box) and transferred to the real-time simulator (central yellow box) via a Small Form-Factor Pluggable (SFP) optical fiber connection. The real-time simulator uses the measured values to calculate new set points (v_1^*, i_1^*) for both amplifiers in the next time step of the discrete simulation.

3.3.2.1 Real-Time Interface for Power System Models

The PHIL setup requires two power amplifiers to emulate the power system state on both sides of the B2B converter. The systems on both sides of the B2B are simulated in real-time and interfaced with the power amplifiers to establish the physical coupling with the B2B hardware.

The SMM described in Section 3.2.1 is used to emulate the upstream transmission grid. The model calculates the frequency deviation $\Delta\omega$ based on the power imbalance, which is then used to generate a three-phase voltage reference for the power amplifier. The block diagram of the interface is shown in Fig. 3.11.

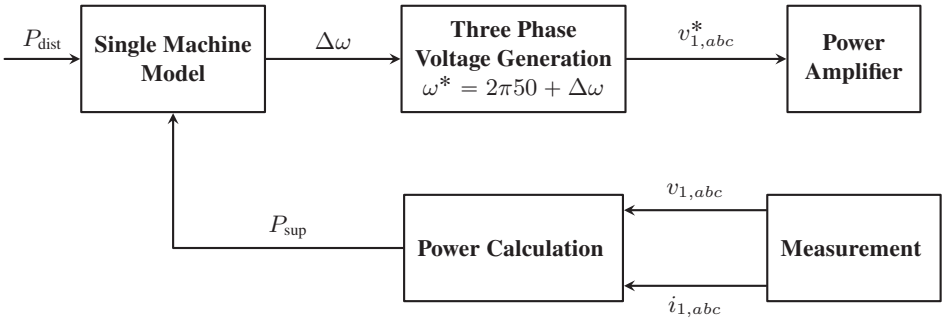

Figure 3.11: Single machine model interface for the PHIL setup. The model uses the measured active power feed back to calculate the frequency deviation $\Delta\omega$ which is used to generate three-phase voltage references $v^*_{1,abc}$ for the power amplifier.

To trigger a frequency disturbance and start a specific scenario the single machine model receives the active power disturbance signal P_{dist}, this results in a power imbalance and a subsequent frequency deviation $\Delta\omega$. The angle deviation is fed to a three-phase voltage generation block that synthesizes the voltage references with the angle $\omega^* = 2\pi 50 + \Delta\omega$. The resulting three-phase voltage reference $v^*_{1,abc}$ is then provided to the power amplifier, which operates as a voltage source interface to the B2B converter hardware. In the feedback loop the measurement unit provides measured voltages and currents ($v_{1,abc}$, $i_{1,abc}$) to the real-time simulator to close the control loop. These measurements can then be used to calculate the active power adjustment used as the active power support signal P_{sup} mitigating the power imbalance and supporting the frequency.

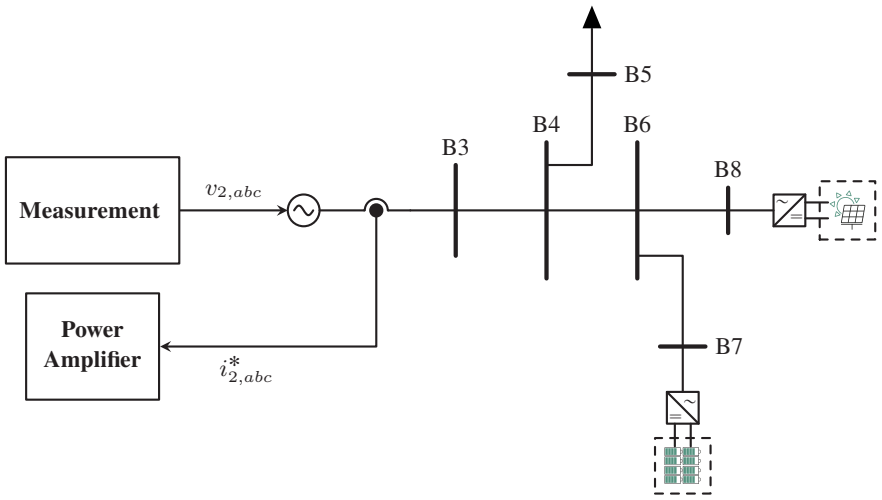

Figure 3.12: CIGRE LV benchmark network interface for PHIL setup. The power amplifier replaces the transformer and upstream voltage source, with current measurements i_{abc} fed back to the real-time simulation.

The CIGRE LV benchmark network described in Section 3.2.2 is used to emulate the downstream distribution grid. The simplified network topology shown in Fig. 3.12 is interfaced to a three-phase controlled voltage source with set points from the measurement of the synthesized B2B LV output voltage ($v_{2,abc}$). This voltage supplies the whole downstream network resulting in a current ($i_{2,abc}$) that is used as a set point for the power amplifier, operating as a current source to interface with the B2B converter hardware.

3.3.2.2 Back-to-Back Converter Implementation

The B2B system is implemented using an imperix power converter with the half-bridge power modules *PEB8038* displayed in Fig. 3.13a, which can be inserted into a modular rack system, here the *4U closed rack - type C* in Fig. 3.13b is used to flexibly build up different converter topologies. Each module is rated for 38 A continuous current and can withstand up to 1200 V which allows a safe operation of a 800 V DC link and an AC side voltage of up to 400 V RMS line-to-line.

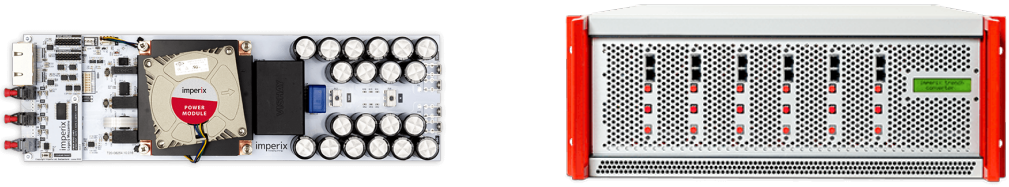

(a) **(b)**

Figure 3.13: The imperix power converter module *PEB3038* in (a) with the closed modular rack in (b), courtesy of Imperix [51].

The rack system displayed can hold up to 6 power modules, which allows the implementation of two full three-phase two-level converters to configure a B2B topology as shown in Fig. 3.14. The DC link is established using the built-in distributed capacitors of each power module, resulting in a total DC link capacitance of $C_{\mathrm{dc}} = 6 \times 5\,\mu\mathrm{F} = 3\,\mathrm{mF}$.

For the grid connection, a passive filter rack from imperix is used. It includes two times an LC filter, plus a third-party EMC filter to mitigate any high-frequency noise generated by the switching behavior of the power modules. Therefore, only one filter rack is used for both sides of the B2B converter. The parameters of the filter and other parameters of the B2B are listed in Table 3.3.

Table 3.3: Back-to-back converter parameters.

Parameter	Value	Parameter	Value
Filter and System			
DC Link Voltage, v_{dc}	800 V	DC Link Capacitance, C_{dc}	3 mF
Switching Frequency, f_{sw}	20 kHz	Rated Power	26 kVA
Filter Inductance, $L_{1/2}$	2.2 mH	Rated AC Voltage (L-L)	400 V_{RMS}
Filter Capacitance, C_{f}	10 μF	Rated AC Current	38 A
Filter Damping Resistor, R_{f}	1 Ω	Pre-Charge Resistors R_{Pre}	47 Ω
PEB3038 Module			
Max. Voltage	1200 V	Max. Continuous Leg Current	38 A
Max. Current	103 A	Number of Modules in total	6
EMC Filter			
Manufacturer	Schaffner EMC	Type	FN3025HP-30-7

In addition to the filter the B2B system is equipped with a grid connection panel that serves as a safe way to put the converter out of operation and to pre-charge the DC link through the passive components.

The general concept of pre-charging follows the idea, that the DC link capacitor is automatically charged up to a certain level through the passive behavior of the power modules, namely the diodes that are conducting current once the AC side voltage is applied (breaker activated by relay S1) and reaches the diode forward voltage. To limit the inrush current during this pre-charging phase, resistors R_{Pre} are connected in series with each phase of the converter. To avoid large power losses during normal operation the resistors are bypassed with breakers activated using relay S3 as illustrated in Fig. 3.14. The natural rectifier peak voltage $\hat{v}_{\text{rec}}$ for a passive (diode-only) three-phase rectifier can be calculated by using the connected line voltage v_{ph}as follows:

$$\hat{v}_{\text{rec}} = \sqrt{2} \cdot \sqrt{3} \cdot v_{\text{ph}} = \sqrt{6} \cdot 230\,V \approx 563\,V \tag{3.25}$$

Fig. 3.14 not only displays the configuration of the filter and precharge circuit, but also the grounding concept that has been used for the PHIL tests. The idea is to avoid completely floating potential, but still honor the fact the both sides of the B2B shall be connected to a different grid. Therefore, the neutral point of both sides is connected with each other but using a high-value resistor R_{N} =1 kΩ to limit any circulating currents that might occur due to potential differences.

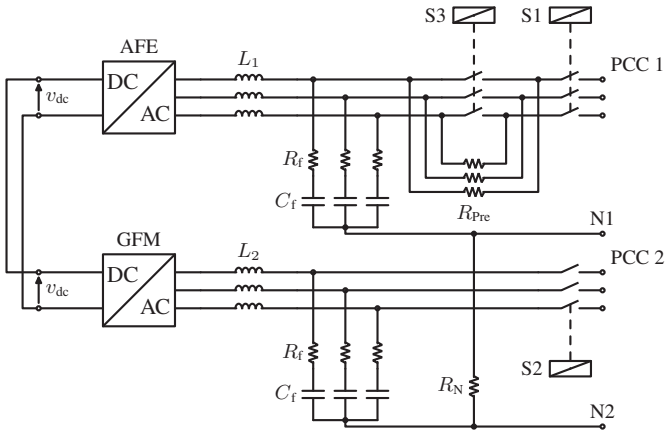

Figure 3.14: B2B grid connection schematic showing both converters, LC filters (L_G, R_f, C_f), and the primary-side connection panel with circuit breakers and pre-charge circuit.

3.3.2.3 Power Interface

For the PHIL setup to be complete, the coupling between the real-time simulation and the HOI is established using so called power amplifiers in the forward path and a measurement unit in the feedback path, as shown in Fig. 3.10. The power amplifiers receive a digital voltage or current signal through an SFP connection and convert it to the real analog value with sufficient power to drive the B2B converter hardware. In the EnergyLab at KIT the power amplifiers for this setup are manufactured by EGSTON and are build in a modular manner, where one amplifier unit is rated for 200 kVA and can be connected in parallel or series to reach higher power or voltage respectively. There are five units located in the upper part of the lab, with two units visible in the left photo in Fig. 3.10, in total a power rating of 1 MVA can be achieved by paralleling five units.

For the testing of the comparably low power B2B system one amplifier is sufficient per side, covering the maximum power of 26 kVA. The amplifier units, called 200 kVA COMPISO System Unit (CSU) GAMP6, for this setup operate independent of each other to emulate the separate grid on either side. Each unit consists of a grid connection cabinet with an isolation transformer, a grid-side AFE converter and six individual COMPISO Digital Amplifiers (CDA), all displayed in Fig. 3.15. The CDA units can be reconfigured internally to achieve different configurations, e.g. 4-wire or 3-wire operation.

A list of parameters and characteristics of the power amplifiers is given in Table 3.4.

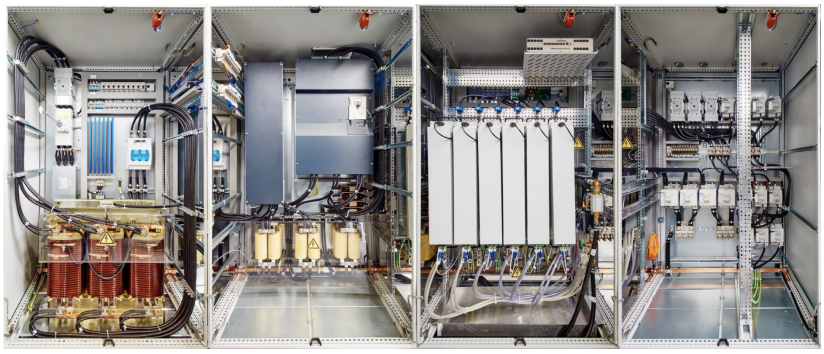

Figure 3.15: View of the interior of the EGSTON 200 kVA CSU. From left to right the photos show, the grid connection and isolation transformer in the first cabinet, the active front-end with filters in cabinet 2, in cabinet 3 the six CDA units and the connection panels and breakers in cabinet 4 [52].

Table 3.4: The characteristics of each Egston 200 kVA CSU.

Characteristics	Value
Nominal apparent power	200 kVA
Maximum AC voltage (phase-to-phase)	450 V_{RMS}
Amplifier bandwidth	5 kHz
Maximum AC current	252 A_{RMS}
Maximum DC voltage	725 V
Maximum DC current (unipolar operation)	900 A
Controller time step	4 μs

4 Scenarios and Services enabled by Asynchronous Grid Connections

After the introduction of possible topologies and control strategies for the ASG system in Chapter 2, and the modeling and testing setups in Chapter 3, this chapter will combine the introduced control concepts and current challenges in modern power systems. The goal is the identification of potential services and scenarios where ASGs can help overcome state-of-the-art challenges and enable further utilization of DG units as *Key Contributions KC1* and *KC2* to address *Research Question 1 (RQ1)*.

ASGs enable a wide range of fundamental grid services that could potentially enhance system stability, control, and overall performance. These services can be provided via system-level control, particularly for the AC/DC interfacing converters. They can also be seen as requirements of future distribution networks to maintain network parameters within the grid-code specified limits. In the first section, the asynchronous concept and its general technical implications and possible applications will be discussed, followed by the presentation of DC operation scenarios and additional services such as active and reactive power flow control.

4.1 The Asynchronous Grid Connection Scenario

Present synchronous power systems are usually operated over wide areas with the use of extensive interconnections to provide sufficient redundancy. The increased share of renewable generators and thus variable generation may introduce high amounts of power fluctuations and stress the existing wide area synchronous networks [53]. A possible workaround to avoid the propagation of fluctuations toward and from the customers could be the partitioning of synchronous networks

Parts of this chapter are reproduced from

F. Wald et al., "Applications and Services of Solid-State Transformers in Active Distribution Networks - A Critical Review," in *IEEE Transactions on Smart Grid*, 2025.

into smaller sections, possibly Active Distribution Networks (ADNs) operating asynchronously, but still exchanging power in a controlled manner.

4.1.1 Enabling Concept

The asynchronous connection is enabled by the capabilities of the power electronic system, e.g., a B2B or SST as introduced in Chapter 2 and illustrated in Fig. 4.1. These systems are capable of synthesizing the LVAC output voltage independent of the MVAC voltage, allowing the LVAC converter to control the voltage magnitude $\hat{V}_2^*$ and frequency f_2^* with a certain flexibility, as long as grid code requirements are met.

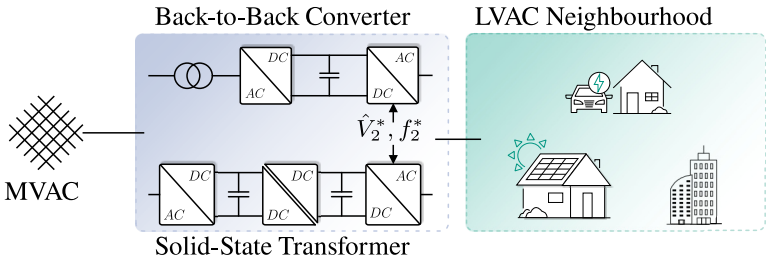

Figure 4.1: A B2B (top) or SST (bottom) enabling an ASG for increased degrees of freedom in downstream distribution systems.

4.1.2 Scenarios

The downstream secondary converter establishing a LVAC system can enable different operation scenarios. For instance, the asynchronous operation of two parallel distribution systems can allow regulated import/export and mutual power conditioning between community microgrids, as proposed by Parashar et al. (2018) and subsequently studied by Zhu, Akanksha, and Mather from 2020 onward [54–56]. Their studies found that the Distributed Energy Resource (DER) hosting capacity can be substantially enhanced while reducing PV curtailment and the number of deep cycles of energy storage systems [57]. A key advantage of an ASG is the ability to operate the downstream grid independently and use that flexibility to deliver multiple services, such as frequency response to the upstream grid, described in the following subsections on active and reactive power flow (Section 4.3, Section 4.4). Moreover, partitioning a synchronous grid into smaller asynchronous sections can limit the propagation of disturbances across the network, for example under unbalanced load or generation conditions [J2].

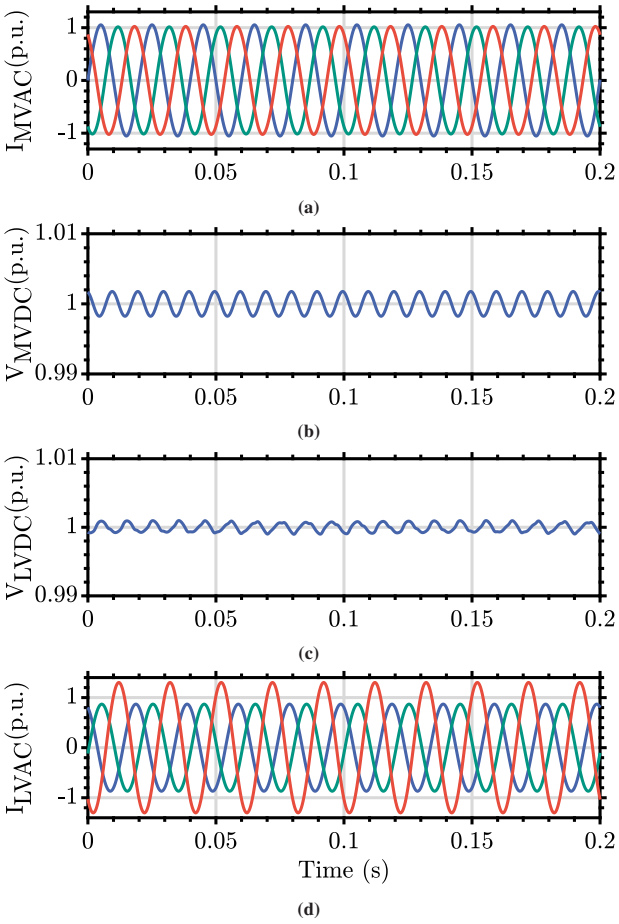

Figure 4.2: Demonstration of an unbalanced load scenario showing the unbalanced AC currents on the LV side in (d). The DC voltages with small ripples are shown in (b) and (c), while the nearly untouched and balanced MVAC currents are shown in (a).

Example - Disturbance Rejection: The plots in Fig. 4.2 illustrate the potential benefits, by displaying the AC current and DC voltage waveforms across a simulated SST system. The system is subject to an unbalanced load condition on the secondary (LV) side, as displayed by the three-phase currents in Fig. 4.2d [58]. The magnitude of phase C of the LVAC current in red is increased by 50% and the impact can be subsequently observed with minor ripples at the DC link on both MV and LV level (Fig. 4.2b and Fig. 4.2c), but does not significantly propagate to the MVAC side displayed in Fig. 4.2a. Only the 100 Hz ripple on both DC links is clearly visible, which is caused by the active power flow pulsating with two times the grid frequency, which is common in single phase AC/DC conversion systems. The observable ripple in this example is

caused by the unbalanced loading of a single phase, introducing or rather amplifying the 100 Hz ripple phenomena. This is a simple demonstration of the advantageous disturbance rejection behavior, even without a specifically designed damping or disturbance rejection algorithm, by simply employing the power transfer algorithms described in Chapter 2.

4.1.3 Project - FlexNet-EkO

In 2023, the FlexNet-EkO project partners, including MR, MITNETZ Strom, TU Dresden and Hochschule Mittweida successfully commissioned a power electronic system connecting a full neighborhood to the upstream substation asynchronously [59]. The project demonstrated the feasibility to run such a system in a real grid, reliably supplying customers with high power quality. Additional features such as outage buffering, by adding a BESS at the DC Link or simply providing grid transparency through extensive measurements have been implemented.

4.2 DC Connectivity for Load and Generator Integration

In the process of transforming the power system toward net-zero emissions, DC-based technologies play a vital role. The power electronic systems used to establish ASGs naturally come with DC terminals that can allow a direct integration of DC loads (e.g., EV charging) and generators (e.g., PV, batteries). Fig. 4.3 illustrates a variety of possible technologies that can be integrated at the DC terminals of an ASG system. The following subsections will discuss the enabling concept and the possible scenarios for DC connectivity in ASGs, paired with a concrete control example.

4.2.1 Enabling Concept

While a B2B only offers a LVDC terminal, certain SST topologies can offer two levels of DC voltage terminals, namely MVDC and LVDC, separated by an isolated DC//DC converter. The AC/DC grid interfaces on both sides, provide a reliable power transfer capability between AC and DC domain with the option to flexibly re-route the power flow.

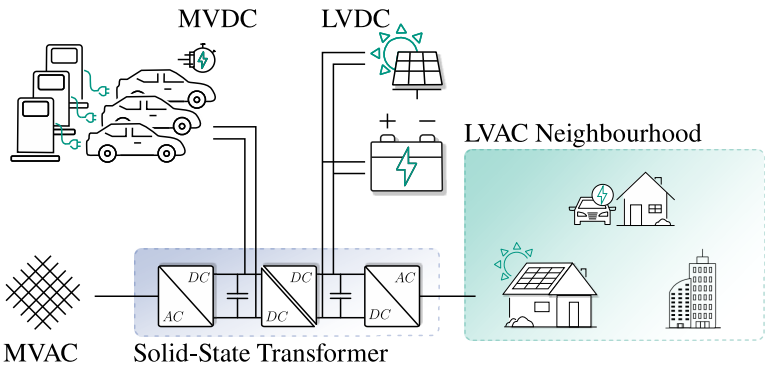

Figure 4.3: A three-stage SST enabling MVDC and LVDC applications, such as EV Fast-Charging, ESSs or PV systems.

4.2.2 Scenarios

Different components can be integrated at their corresponding DC voltage levels, offering distinct advantages over equivalent AC network integration approaches. Consequently, the applications enabled by the DC voltage terminals can be categorized according to their operating voltage levels.

Low Voltage DC: Due to their inherent DC nature, renewable energy sources including PV systems, storage systems, such as fuel cells, and batteries can be directly connected to the LVDC link of SSTs through a single DC//DC conversion stage, thereby eliminating an additional AC/DC conversion step. Similarly, DC loads including LED street lighting systems, EV charging infrastructure, and small-scale computing centers can be directly interfaced via the LVDC terminal. The strategic integration and coordinated management of these DC energy technologies facilitate DC microgrid implementations, as demonstrated in numerous studies, enabling service provision to upstream AC networks [60–68, J2].

Beyond direct component integration at the LVDC level, the LVDC link can be expanded to establish a comprehensive DC network infrastructure that operates in parallel with the existing AC network while providing interconnection points. This configuration enables distributed placement of DC resources throughout the network and optimizes energy flow through the creation of meshed hybrid network architectures [69]. These LVDC meshed hybrid networks enhance power flow control capabilities and minimize overall AC system losses by facilitating more flexible integration of renewable energy sources within the LVAC network [70, 71, J2].

Medium Voltage DC: The currently most popular use case for MVDC is the integration of high-power EV fast charging infrastructure (exceeding 1 MW capacity). Additionally, MVDC terminals can form meshed network topologies, especially at regional scales, to interconnect various high-voltage substations. This capability enables enhanced energy flow optimization and

delivers improved power supply reliability to connected loads across both LV and MV levels. Furthermore, it supports increased renewable energy integration from sources such as PV systems and wind turbines, as well as energy storage systems [30, 72, 73]. In future power system architectures, the SST MVDC link may function as a DC power routing hub interconnecting multiple network segments.

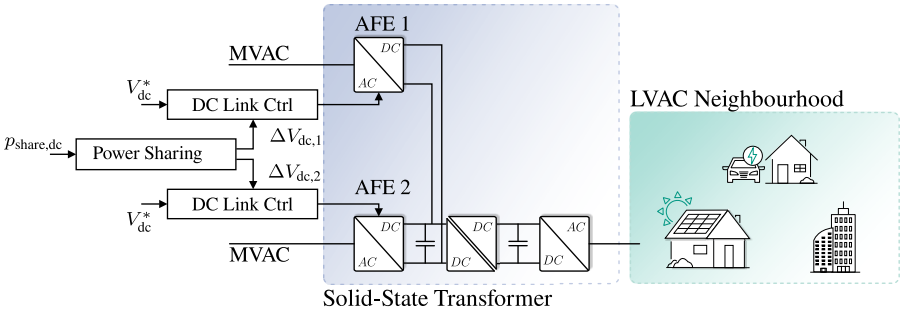

Figure 4.4: DC Power Sharing Concept, for an ASG realized with a three-stage SST with a multi-terminal MVDC link feeding.

Example - DC Power Sharing: As example for a possible application of an ASG, Fig. 4.4 illustrates a multi-terminal SST which has two MVAC/MVDC interfaces that can supply the DC link by two independent AFEs. Thus, the supply of the DC link can be shared or flexibly reconfigured, here by means of a DC droop control on top of the standard GFL AFE controller. This feature allows the SST to free up capacities in one of the connected converters for other services such as reactive power compensation or a frequency response.

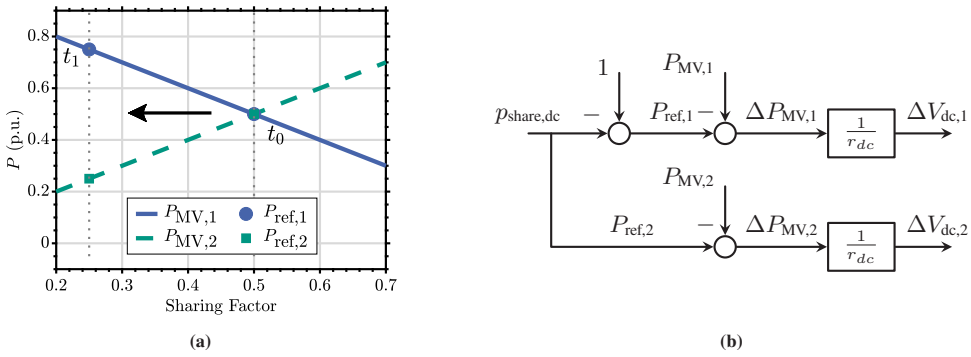

Figure 4.5: DC power sharing control implementation: (a) droop characteristics showing the relationship between DC voltage deviation and power sharing, and (b) block diagram illustrating the control algorithm for calculating DC voltage reference offsets based on the power sharing factor.

The block diagram in Fig. 4.5b illustrates the basic functionality of the DC power sharing control algorithm. The system takes a power sharing factor $p_{\text{share,dc}}$ as input, which determines how the total DC power is distributed between the two AFEs. For the first converter, this factor is subtracted from unity to create the power reference $P_{\text{ref,1}}$, while the second converter uses the sharing factor directly as $P_{\text{ref,2}}$. Each path then compares the power reference with the measured power ($P_{\text{MV,1}}$ and $P_{\text{MV,2}}$) to generate power deviations ($\Delta P_{\text{MV,1}}$ and $\Delta P_{\text{MV,2}}$), this assumes a per unit calculation. These deviations are processed through respective droop coefficients ($1/r_{\text{dc}}$) to calculate the DC voltage reference offsets ($\Delta V_{\text{dc,1}}$ and $\Delta V_{\text{dc,2}}$) for each converter's DC-link controller.

The droop characteristics in Fig. 4.5a demonstrate the inverse relationship between the two converters' power outputs as a function of the sharing factor. At the reference operating point (t_0, sharing factor = 0.5), both converters supply equal power ($P_{\text{MV,1}} = P_{\text{MV,2}} = 0.5$ p.u.). When the sharing factor is reduced to 0.25 (t_1), AFE1 increases its power output to approximately 0.75 p.u., while AFE2 reduces its output to 0.25 p.u., effectively shifting 75% of the total power burden to AFE1. This complementary behavior ensures continuous power supply while enabling dynamic load redistribution between the parallel converters.

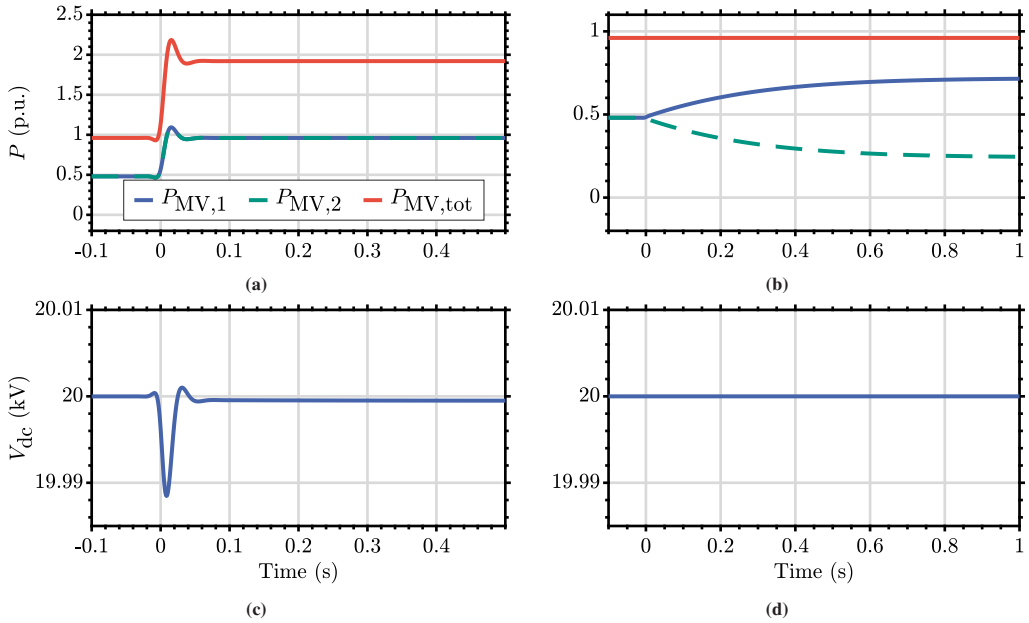

Figure 4.6: Multi-terminal AC/DC SST with DC power sharing control. Left column: LV load step response showing (a) active powers $P_{\text{MV,1}}$, $P_{\text{MV,2}}$, and $P_{\text{MV,tot}}$, and (c) DC link voltage V_{dc}. Right column: power sharing shift showing (b) 75%/25% redistribution between converters and (d) stable DC link voltage V_{dc}.

Fig. 4.6 displays simulation results of the mentioned application, where the left column shows the response to a load step on the LV side and the right column a shift in the converter loading, toward a higher loading of the AFE1 and a reduced loading of AFE2. The total power $P_{\text{MV,tot}}$ is equally supplied by $P_{\text{MV,1}}$ and $P_{\text{MV,2}}$ in Fig. 4.6a. In the moment of the load step a slight disturbance in the DC link is triggered as seen in Fig. 4.6c. This results in a loading of both AFE1 and AFE2 to nearly 1 p.u.. The second simulation scenario revolves around a shift in the loading of the two converter. In this scenario, the loading of 50% of both AFEs in the left column is now shifted. After the sharing factor shift from 0.5 to 0.25, AFE1 covers 75% of the power supply ($P_{\text{MV,1}}$) and AFE2 only 25% ($P_{\text{MV,2}}$), as depicted in Fig. 4.6b and introduced by the droop characteristic displayed in Fig. 4.5a. That behavior allows AFE2, to have additionally capacities for other services such as reactive power compensation or simply rerouting the power flow toward the Point of Common Coupling (PCC) of AFE1.

4.2.3 Project - LVDC Grid Interface by EATON

The recent publication of Yu et al. in the proceedings of the IEEE Energy Conversion Congress and Exposition in 2024, showed the current progress of EATON's research labs in China in developing a SST for LVDC applications [74]. The study presents a topology based on a modular input serial and output parallel concept where the input voltage is increased by serializing cascaded H-bridges and connecting the DC output in parallel to reach high currents. This is done by employing SiC-MOSFET semiconductors to achieve 2 MW or power at 10 kV AC input voltage and 800 V DC output voltage. In the validation and testing procedures, the prototype passed a 42 kV withstand voltage insulation test and 75 kV lighting impulse, while reaching a peak efficiency of 98.3 % and a power density of 223kW/m^2.

4.3 Active Power Flow Control

The active power flow can be shaped mainly through the secondary LV side converters operating mode (GFM vs. GFL), while the upstream MV stage typically focuses on the DC link voltage control.

An active power flow controller for ASGs primarily depends on the requirements of the downstream grid, is the grid stable in itself or does it require a reliable voltage source acting as a GFM node? When an ASG is established to an already stable and existing grid, e.g., when a grid-forming energy storage system supplies the network, the B2B or SST can operate as a pure grid-following system, which allows very flexible adjustment of the active power flow. If the

ASG is operating as a grid-forming entity on the other hand, e.g., when no other grid-forming node is available in the grid, the flexibility of the active power control is significantly impaired, since the active power consumption/generation is dictated by the downstream connected devices. This complicates the technical framework to enable an ASG to deliver active power flow control capabilities, while operating as a grid-forming entity on the LVAC side. The technical concept is discussed in the following subsection.

4.3.1 Enabling Concept

The question is how, can a grid-forming controller adjust the active power flow, while sufficiently supplying a grid code-compliant voltage magnitude and frequency? In HV and MV grids, this issue is commonly tackled by utilizing the commonly known power grid characteristics, where the active power P is proportional to the frequency f and the reactive power Q is proportional to the voltage magnitude $\hat{V}$, paired with the fact that the necessary power is balanced over wide areas. Unfortunately, matters in LV distribution grids are not as clear and the quantities P and Q might influence both f and $\hat{V}$ and vice versa. Thus, to control the active power flow in the LV grid, it is not sufficient to simply change the frequency and achieve a resulting change in active power. The goal must be to influence the connected nodes in a way that their active consumption or generation follows the desired control objective. A brute force method to achieve that would be, to install additional controllers paired with a highly sophisticated communication infrastructure in a large part of the connected nodes and dictate their desired active power set point. This approach could certainly work but introduces a variety of challenges, such as privacy concerns of end customers, high investment cost for the communication and control infrastructure paired with a complex control layer.

Therefore, this work proposes a control algorithm for ASGs utilizing known sensitivities of the connected nodes, specifically the $P \sim f$ droop characteristic of connected DG and storage units. This characteristic is known to be available due to the German grid connection rules VDE-AR-N 4105, which require every newly connected distributed generator to obey this droop characteristic [75]. Simplified, the grid code demands a droop characteristic that reduces active power feed-in during over-frequency events and an increase of active power feed-in during under-frequency events. Ideally, the full power flexibility shall be estimated using real-time sensitivity estimation methods, as discussed by Courcelle et al. in 2024 and Tao et al. in 2024 [76–79]. For simplicity reasons, and because it would be out of the scope of this work, we assume a known sensitivity of the connected loads to frequency due to the above mentioned norm and a sensitivity of active power to voltage due to existing resistive lines and consumers. Based on these two sensitivities, the voltage magnitude ($\hat{V}_2$) and frequency (f_2) as illustrated with the blue arrows in

Fig. 4.7, can be used to adapt the active power generation and consumption and thus control the active power flow in the ASG.

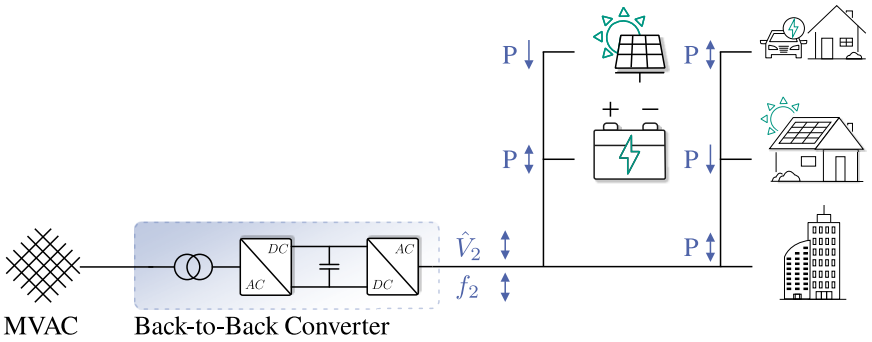

Figure 4.7: Active power flow control scheme established with a B2B system, including active resources in the low-voltage distribution network, reacting to voltage ($\hat{V}_2$) and frequency (f_2) adjustments.

4.3.2 Services

The capacity to control the active power flow empowers operators to leverage this advantage in multiple ways and integrate it in their service portfolio. For instance, it is possible to reroute the active power flow, when acting as a soft-open point connection in GFL operating mode, to reduce stress on other substations. As a result, this can avoid or postpone expensive network upgrades or energy curtailment [80]. Most importantly, the active power flow control feature allows the ASG to directly influence the active power balance of the upstream system and, due to the aforementioned relation between active power balance and frequency ($P \sim f$), an ASG can provide frequency response services. The margin of available active power highly depends on the operation mode of the LV DC/AC converter. As discussed above, in GFL mode the margin could cover the entire capacity of the power electronic system, whilst in GFM mode, the available active power correlates with the amount of units that obey the mentioned grid codes or characteristics. Recent studies have shown the promising capabilities of the power flexibility enabled by power electronic systems such as SSTs to support the MV network during frequency contingencies [81–84, J1, J2].

Furthermore, active power flow control capabilities can address the growing challenge of unexpected reverse power flows occurring from the LVAC network toward the MV grid in ADNs, an issue that conventional LFT technology cannot resolve [85].

4.4 Reactive Power Compensation

As bidirectional power flow becomes more common in future power systems, significant fluctuations in the voltage are likely to arise more often. Therefore, managing the voltage magnitude to remain within the grid-code boundaries is a critical service for system operators. This subsection examines the technical requirements to provide reactive power to the upstream grid and subsequently offer voltage support services, similar to the example illustrated in Fig. 4.8.

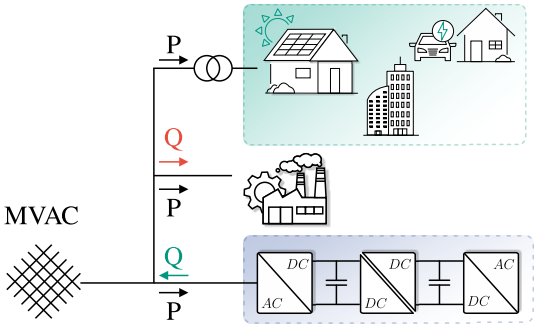

Figure 4.8: Reactive power flow and voltage support scenario offered by a SST.

4.4.1 Enabling Concept

In most operation scenarios, the primary side of the ASG facing toward the upstream grid operates in GFL mode. This allows the controller, with its main objective of maintaining the DC link voltage at a stable level, to flexibly control the reactive power. The reason for this is that the DC link voltage is controlled by the active current i_{d}^{*} to charge and discharge the capacitor, which opens a degree of freedom for the control of the reactive current component i_{q}^{*} (as described in Chapter 2). Even though the reactive power can be controlled flexibly, it is evident that the amount of available reactive power is limited by the overall capacity of the power electronic system. The available reactive power can subsequently be calculated based on the apparent power (S) equation, $S = \sqrt{P^2 + Q^2}$, which leads to the conclusion that the available margin for reactive power could be increased by reducing the active power load, P. This can be achieved by means of the previously mentioned active power control features.

4.4.2 Services

The capability to flexibly offer reactive power to the upstream grid is quite similar to the features of a Static Synchronous Compensator (STATCOM). A system specifically designed to compensate for the reactive power consumption of long lines or feeders and thus maintain the voltage magnitude at the end of the feeder. Multiple publications by Zheng, Gao, and Giacomuzzi between 2018 and 2022 highlight this service provided by a SST and compare it to a STATCOM [84, 86, 87]. The study of Gao et al. in 2018, comparing a SST with a STATCOM determined that a direct comparison between the two systems is not feasible. However, they found that for components of the SST capable of matching the STATCOM functionality, the reactive power support service might be more cost-effective than constructing a dedicated system for this service alone. In terms of concrete application examples, Shah and Crow already proposed a dynamic online Volt-Var Control (VVC) algorithm to regulate the nodal voltage by injecting or absorbing reactive power through a SST in 2016 [88]. Additionally, the SST in combination with energy storage systems has been proven to successfully control voltage and power dispatch in ADNs simultaneously [65]. Furthermore, the ability to compensate for reactive power can increase distribution networks' DER hosting capacity, as recently demonstrated by Zhu et al. [57].

4.5 Projects and Demonstrators

The development of SST technology can be traced back to 1970 when McMurray patented the high-frequency link concept, laying the foundation for modern DC//DC conversion in power electronics [22]. However, due to limitations in semiconductor technology at the time, practical implementations remained elusive for several decades. First concrete research projects were initiated in 2011 by GE, proposing a power electronic-based substation, followed by the adaption of the concept to traction applications by ABB [89, 90]. These systems had a variety of shortcomings such as the lack of standards, but most importantly research focused mainly on hardware developments, without distinguished business cases and (control) strategies to embed the SST into existing systems.

As illustrated in Fig. 4.9 and displayed in Table 4.1, the revolution of private transportation with the introduction of affordable and competitive EVs was a significant development accelerator. The SST can play a crucial role in efficient high power charging infrastructure. This development also led to an increase in naval applications projects, that basically need a similar infrastructure to charge a vehicle in a short amount of time [91].

The period from 2018 to 2024 marked a significant increase in academic research projects, as documented in Fig. 4.10, establishing the theoretical and practical foundations for commercial

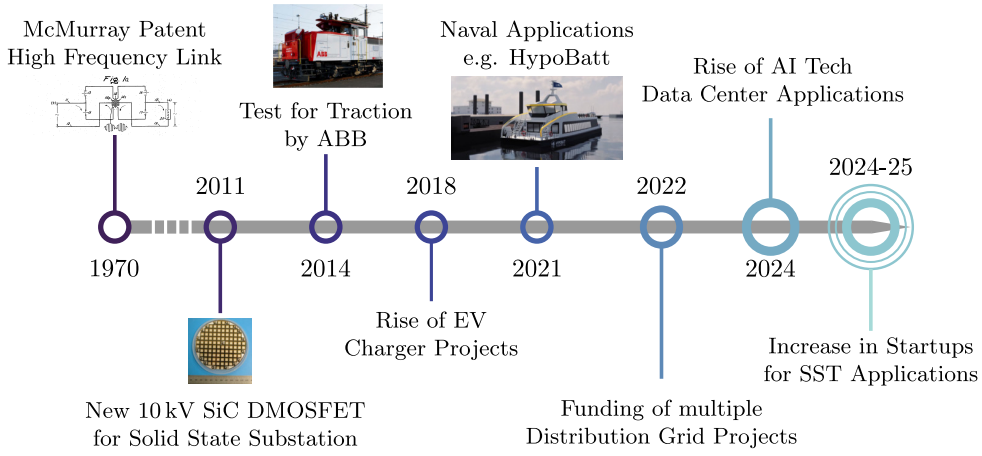

Figure 4.9: Visualized history of the SST development and key milestones, based on Table 4.1 [22, 89–92].

deployment, in charging as well as distribution grid application (AC/DC Networks). The generated knowledge and the simultaneous advent of AI technologies, associated with the rise in data center power consumption from 2024 on opened another major market segment.

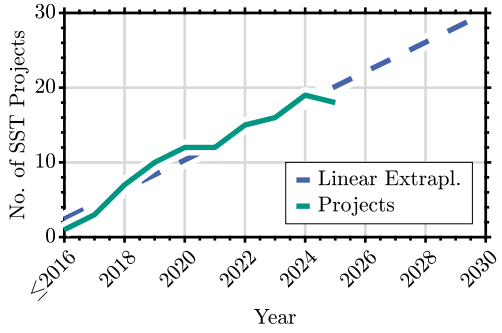

Figure 4.10: Number of SST projects and companies over time, with a simple first order extrapolation, based on the projects mentioned in Table 4.1, adopted from [J2].

This finally led to the founding of multiple start-up companies focusing on SST applications, as shown in the lower parts of the table. It also shows the dominance of US based companies, where the focus is on AC/DC distribution networks, followed by charging, and data center applications. This might come as a surprise for European readers, since Europe has been a leader in research projects as shown in Table 4.1, but the commercial exploitation seems to be more advanced in the US so far. Besides the fact that the available capital for investments in new technologies is generally higher in the US, the reason might be also found in the higher need for grid modernization in the US.

Table 4.1: Comprehensive overview of SST development projects and manufacturers, chronologically ordered.

Project/Company	Type	Year	Rating	Country	Application	Reference
GE and Wolfspeed	Project	2011	1 MVA, 13.8 kV	US	Naval, AC/DC networks	[89, 93]
Gridbridge ERMCO	Manufacturer	2017	500 kVA	US, NC	AC/DC networks	[94]
Suzhou Tongli	Project	2017-20	1000 kW, 10 kV	China	AC/DC networks, EV chargers	[95]
Single-Phase - Pusan	Project	2018	150 kW, 13.2 kV	South Korea	Hybrid AC/DC networks	[96]
ALigN	Project	2018-20	250 kVA	Germany	EV chargers	[97, 98]
LV Engine	Project	2018-22	500 kW, 10 kV	Scotland, UK	AC/DC networks	[99–101]
Delta Americas	Project	2018-22	400 kW, 13.8 kV	US	EV chargers	[68, 102]
FUNDRES	Project	2019-21	300 kW, 9 kV	EU	Railway systems	[103]
FlexNet-EkO	Project	2019-22	>300 kW	Germany	Active distribution networks	[59]
ENSURE	Project	2019-23	2 MW, 20 kV	Germany	AC/DC networks, EV chargers	[104]
TIGON	Project	2020-24	300 kW	EU	AC/DC networks	[105]
Solid State Power	Manufacturer	2020	-	US, TX	AC/DC networks	[106]
Resilient Power	Manufacturer	2020	1 MW	US, TX	EV chargers	[107]
HypoBatt	Project	2021-2025	>2 MW	EU	Naval Vessel Charging	[91]
MUSE SST	Project	2021	100 kW, 4.16 kV	US	AC/DC networks	[108, 109]
AC2DC	Project	2022	40 MW, ±60 kV	Germany	MVDC networks	[110]
50 kVA CSI	Project	2022	50 kVA, 7.2 kV	US	EV chargers, Data Centers	[111]
ACT/MCT - ETH	Project	2022	166 kW, 7 kV (DC)	CH	Efficiency of DC/DC conversion	[112, 113]
SSTAR	Project	2022-25	50 kW	EU	Efficiency and new materials	[114]
Super - Heart	Project	2022-25	100 kW	Germany	AC/DC networks, Storage integration	[115]
Amperesand	Manufacturer	2023	6 MW, 22 kV	Singapore/US	EV chargers	[116]
Charge America	Manufacturer	2023	1.2 MW	US, CA	EV chargers	[117]
DG Matrix	Manufacturer	2023	400 kW	US, NC	AC/DC networks, EV chargers	[118]
Novos Power	Manufacturer	2023	13-48 kV	US, CA	Data Centers	[119]
Eaton	Project	2024	2 MW, 10 kV	China	LVDC Grid Interface	[74]
Alderbuck	Manufacturer	2024	-	US, CA	AC/DC networks	[120]
DC Grid	Manufacturer	2024	-	US, CA	AC/DC networks	[121]
Heron Power	Manufacturer	2024	5 MW	US, CA	AC/DC networks, Data Centers	[122]
Hyperscale Power	Manufacturer	2025	-	Switzerland	AC/DC networks	[123]

5 Asynchronous Grid Connections for Frequency Response Services

This chapter investigates the potential of an ASG to provide a frequency response service, addressing *Research Question 3 (RQ3)*. A brief theoretical introduction to the concept of frequency response and frequency response as service is followed by the practical implementation of a new concept called *Frequency Propagation*, representing *Key Contribution KC5*. At its core, this concept uses the frequency deviation of the primary side power system to amplify and propagate to the secondary side and thus trigger frequency and voltage dependency of DG units. The concept of frequency propagation is tested and validated using the earlier introduced concept of PHIL, here in a double PHIL setup (see Chapter 3). As a result the measurements show the feasibility of the proposed concept and highlight potential barriers that need to be overcome ahead of a large-scale implementation, constituting *Key Contribution KC6*.

5.1 Frequency Response Services

A frequency response of a device connected to the power system can be associated with a service when the provided functionality is remunerated. The term *frequency response* is defined as the reaction of a device to the power system frequency. This reaction is typically a consequence of a discrepancy between the actual and nominal frequency (50 Hz or 60 Hz), leading to an adjustment of the consumed or generated active power of the device. The frequency response of a device can be classified according to the time required for a change in active power to be achieved.

The following classifications are widely adopted in the literature and deployed in most major power systems [124, 125].

Parts of this chapter are reproduced from

F. Wald, Q. Tao and G. De Carne, "Virtual Synchronous Machine Control for Asynchronous Grid Connections," in *IEEE Transactions on Power Delivery*, vol. 39, no. 1, pp. 397-406, Feb. 2024.

Inertial Response

Definition. Inertial frequency response is defined as the immediate or near immediate response of a device to a change in frequency $d\omega/dt$, typically occurring within milliseconds after a disturbance. Historically, this response was physically tied to the kinetic energy stored in the rotating mass of synchronous machines and not controllable itself. Inverter-based resources can mimic this behavior through control algorithms, but the response is not truly instantaneous due to measurement and control delays.

Primary Control

Definition. Primary frequency control is defined as automated control actions that adjust power output in response to frequency deviations, typically occurring within seconds after a disturbance. A primary control action should be sustained and allow the arrest of the frequency drop to a stable level.

Secondary Control

Definition. Secondary frequency control is defined as a control action that restores the system frequency to its nominal value (usually within minutes), after the initial arrest and stabilization phase. This is achieved by slower semi-automatic generator redispatching, to maintain a balanced interconnection system.

Tertiary Control

Definition. Tertiary frequency control is defined as long-term adjustments, often involving manual intervention, to ensure the availability of sufficient reserves for future contingencies, while operating economically efficient.

The timeline shown in Fig. 5.1, qualitatively illustrates the order in which each service is provided, in addition the timescale on which inverter-based resources can perform frequency response services is displayed in red. Illustrated by the black and blue dashed frequency graph are the response of the system frequency to a power imbalance. Where the blue dashed graph represents a scenario in which the power system has higher inertia and damping compared to the response shown by the black trace. The nadir describes the largest frequency deviation reached after a disturbance. The Rate of Change of Frequency (RoCoF) is the gradient at which the frequency changes after a disturbance. These values can be used to determine the severity of a disturbance, since they reflect the availability of inertial response capacity and show the system ability to arrest the frequency disturbance, i.e., compensate the power imbalance.

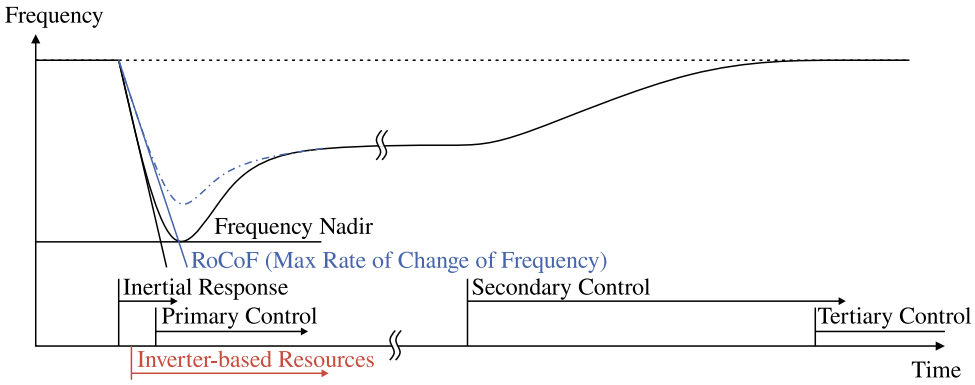

Figure 5.1: Timeline of frequency response services showing the activation sequence and duration of different control mechanisms following a frequency disturbance in the power system. The blue dashed frequency trace represents a contingency in a high inertia power system, while the black trace represents a contingency in a low inertia system.

This work focuses on power electronic systems, in particular ASGs and their fast frequency response capabilities. This is why the following sections mainly discuss the first two classes of frequency response (inertial and primary), while refraining from going into detailed descriptions of the secondary and tertiary frequency control services.

5.1.1 Inertial Frequency Response

The inertial frequency response is the instantaneous supply of an active power imbalance in the grid, by the decrease of stored kinetic energy. This is generally tied to the interaction of synchronous generators with the grid, since their rotating mass has a certain angle and the stored kinetic energy within that mass is tied to the electrical angle of the power system. Mathematically this can be described using the so-called swing equation (Eq. (2.38)), already introduced in Chapter 1 and Chapter 2. Embedding the behavior of synchronous generators into converter controls artificially, enables inverter-based resources to provide near-inertial frequency response. Nonetheless, the inertial synchronous generator response is indeed instantaneous, due to the physical coupling, which is not the case for inverter-based resources. Their response is achieved through measurements and controls that inherently are not instantaneous. The response delay typically depends on the bandwidth of the frequency estimation method, e.g., a Phase-Locked Loop (PLL) (20-100 Hz) [126]. This delay still allows for a fast response that can be classified somewhere in-between the inertial and primary frequency response. Important to mention is that there are currently very few energy markets that remunerate the immediate and short-term participation of inverter-based resources in a FFR scheme. The following markets, Ireland ([127]), the US (e.g., the PJM RegD/RegA services [128]) or Australia ([18]), have implemented markets

and mechanisms to foster and remunerate devices that provide an inertial or close to inertial response. Fig. 5.2 illustrates the currently implemented frequency control service frameworks by ENTSO-E for the Central European interconnection system. It can be seen that the fastest service is the FCR, which is generally associated with primary frequency control, but does not require or incentivize a response within milliseconds [129]. Which means that there is currently no market in Central Europe for systems that can operate within the milliseconds to second timescale without a long-lasting sustainable energy source.

5.1.2 Primary Frequency Control

The primary frequency control is generally aimed at containing the frequency deviation (ENTSO-E also refers to it as FCR) to a level that is non-critical for the power system. The ENTSO-E defines this non-critical area to a ± 200 mHz band around 50 Hz. In general the primary control should be designed to have a proportional behavior, usually referred to as droop characteristic. This leads to the fact, that a primary control results in a contained frequency with a stationary offset of the frequency compared to the nominal value. Fig. 5.1 displays the intermediate offset during the transition from primary to secondary control, which is why after a successful frequency containment, subsequent control layers with integrating characteristics are needed to regain the nominal frequency.

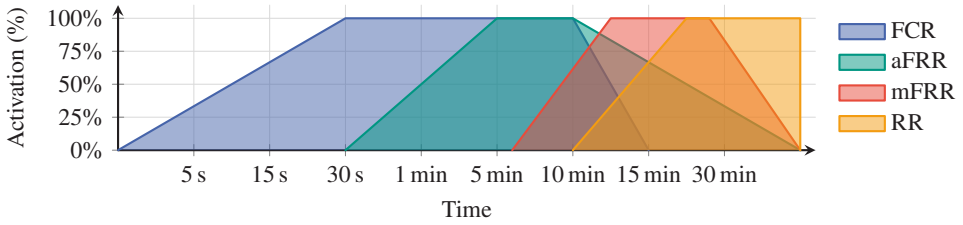

Figure 5.2: ENTSO-E frequency control services and their respective activation and duration timing showing Frequency Containment Reserve (FCR), Automatic Frequency Restoration Reserve (aFRR), Manual Frequency Restoration Reserve (mFRR), and Restoration Reserve (RR).

In terms of incentives, the Central European Transmission System Operators (TSOs) run a FCR market. The general concept is based on day-ahead auctions to bid reserve capacities for 4-hour windows in which the symmetric FCR must provide primary control services. The minimum size and resolution is 1 MW, which renders most small or flexible resources ineligible for participation [17]. In addition, the FCR market is not designed to incentivize very fast response times, within the milliseconds to seconds timescale, which again bars participation from many fast-responding resources such as an ASG [130]. The market structure is not the focus of the

current chapter, but will be discussed in more detail during the case study in Chapter 6, which includes the implementation of a frequency response market framework to assess possible revenue streams for the ASG.

For completeness, the activation timeline of the ENTSO-E frequency control services illustrated in Fig. 5.2, also displays the slower services aFRR, mFRR, and RR which correspond to the secondary and tertiary frequency control mechanisms described earlier.

5.2 The Asynchronous Grid Connection for Frequency Response

The power electronic system establishing an ASG is one of the power electronic systems that can provide near inertial and primary frequency control services, given the right environment and control design. In the following, the ASG is presumed to be operated in a distribution grid and is established through the previously introduced B2B converter system shown in Fig. 2.7. The frequency response service described in detail in Section 4.3 is enabled by the ability of the system to control the active power flow, which depends on the operation mode of the ASG. In the scenarios investigated in the following, the secondary side converter (not responsible for DC link control) is operating in GFM mode, supplying a small downstream grid with sufficient power. In such a case the active power control is much more complicated to achieve, since the active power flow in the ASG is dictated by consumers and generators. Thus, it is necessary to influence the behavior of the connected loads and generators directly, which can be achieved by exploiting the so-called sensitivity of connected loads and generators. This concept is explained in more detail in the following subsection.

5.2.1 Load Sensitivity

The behavior of loads in a power system is influenced by many external factors, including the voltage and frequency of the connected power system. Most loads have some form of sensitivity to the voltage or frequency of the grid. For example, passive components may behave like an impedance connected to the grid, with a quadratic sensitivity to the voltage. The fact that the power consumption varies with the condition of the power system has been investigated by a variety of studies, e.g., the UK-based Customer Load Active System Service (CLASS) project, in which the authors identified load model parameters from measurements of over 100 bus bars in the MW range [131]. These findings lead to the development of advanced voltage controllers for substations in later stages of the project. The controllers allowed the voltage dependent load

control, while maintaining power quality and avoiding a noticeable impact on customers and enabled a demand response flexibility within the distribution system [132].

A sensitivity parameter can be described using the deviation of power with respect to the deviation in voltage or frequency respectively. Mathematically we define the four sensitivity parameters, active power-to-voltage (σ_p), reactive power-to-voltage (σ_q), active power-to-frequency (τ_p) and reactive power-to-frequency (τ_q), as follows:

$$\sigma_\mathrm{p}(t) \overset{\text{def}}{=} \left.\frac{\mathrm{d}P(t)/P_0(t)}{\mathrm{d}V(t)/V_0(t)}\right|_{f(t)=f_0(t)} \tag{5.1}$$

$$\sigma_\mathrm{q}(t) \overset{\text{def}}{=} \left.\frac{\mathrm{d}Q(t)/Q_0(t)}{\mathrm{d}V(t)/V_0(t)}\right|_{f(t)=f_0(t)} \tag{5.2}$$

$$\tau_\mathrm{p}(t) \overset{\text{def}}{=} \left.\frac{\mathrm{d}P(t)/P_0(t)}{\mathrm{d}f(t)/f_0(t)}\right|_{V(t)=V_0(t)} \tag{5.3}$$

$$\tau_\mathrm{q}(t) \overset{\text{def}}{=} \left.\frac{\mathrm{d}Q(t)/Q_0(t)}{\mathrm{d}f(t)/f_0(t)}\right|_{V(t)=V_0(t)} \tag{5.4}$$

In discrete form we can use the deviation of power to voltage or frequency between two measurements (k and k-1) to define the following parameters as an approximation of the continuous definition above:

$$n_\mathrm{pv} = \frac{P_\mathrm{k} - P_\mathrm{k\text{-}1}/P_\mathrm{k\text{-}1}}{V_\mathrm{k} - V_\mathrm{k\text{-}1}/V_\mathrm{k\text{-}1}} \approx \sigma_\mathrm{p} \tag{5.5}$$

$$n_\mathrm{qv} = \frac{Q_\mathrm{k} - Q_\mathrm{k\text{-}1}/Q_\mathrm{k\text{-}1}}{V_\mathrm{k} - V_\mathrm{k\text{-}1}/V_\mathrm{k\text{-}1}} \approx \sigma_\mathrm{q} \tag{5.6}$$

$$n_\mathrm{pf} = \frac{P_\mathrm{k} - P_\mathrm{k\text{-}1}/P_\mathrm{k\text{-}1}}{f_\mathrm{k} - f_\mathrm{k\text{-}1}/f_\mathrm{k\text{-}1}} \approx \tau_\mathrm{p} \tag{5.7}$$

$$n_\mathrm{qf} = \frac{Q_\mathrm{k} - Q_\mathrm{k\text{-}1}/Q_\mathrm{k\text{-}1}}{f_\mathrm{k} - f_\mathrm{k\text{-}1}/f_\mathrm{k\text{-}1}} \approx \tau_\mathrm{q} \tag{5.8}$$

where V is the voltage RMS value, f the frequency, P and Q the active and reactive power at sample k and k-1 respectively. The sensitivity parameters can be calculated from measurements. The resulting values may come close but will never exactly match the continuous definition, which is why a different notation (n_pv, n_qv, n_pf, n_qf) is used. The active and reactive power deviation between the two samples is subsequently normalized with respect to the k-1 sample.

This formulation theoretically allows the update of the value every few samples, but k-1 can also be defined to be a fix value like the nominal voltage, e.g., if the power at nominal voltage is known.

The sensitivity estimation can be done using different methods, e.g., the On-Line Load sensitivity Identification (OLLI) or iterative methods such as the Newton method [133, 134]. The parameter identification is not the focus of this work, therefore the following publications can give more insights into the matter if needed [Co1, 76–79]. In the following experiments we assume a known sensitivity parameter, which can subsequently be used to estimate the power flexibility using the following exponential load model and the introduced parameters.

$$P = P_0 \cdot \left(\frac{V}{V_0}\right)^{n_{\text{pv}}} \cdot \left(\frac{f}{f_0}\right)^{n_{\text{pf}}} \tag{5.9}$$

$$Q = Q_0 \cdot \left(\frac{V}{V_0}\right)^{n_{\text{qv}}} \cdot \left(\frac{f}{f_0}\right)^{n_{\text{qf}}} \tag{5.10}$$

The sensitivity values are usually in the range of 0 to 2, where 0 denotes a constant power load not susceptible to a deviation in voltage or frequency respectively. A value of $n_{\text{pv}} = 1$ represents a constant current load while a value of 2 represents an impedance characteristic. In reality the values can also be in-between these values and the sensitivity of a whole neighborhood is a composition of sensitivities of smaller loads and generators. Inverter-based resources such as BESS or PV systems can artificially change their sensitivity by adapting their internal control objectives and therefore exceed the usually observed sensitivity ranges of 0 to 2. This has been further investigated by De Carne et al. in 2018 [135].

For a large amount of active resources such as BESS or PV, lacking modern control algorithms the inherent behavior is close to a constant power load. These units are unable to react to current grid conditions and do not have a secondary grid support control objective. As mentioned in the active power flow control service section, connection rules in Germany evolved and now require newly connected generators to offer certain support feature, due to the grid connection rule VDE AR-N 4105 [75]. This connection rule demands a supportive behavior of newly connected renewable generators during under and over-frequency events, if technically feasible. The control behavior is clearly defined as a droop characteristic with a slope of 40%P_0/Hz of active power generation reduction during over-frequency and vice versa. Although certain exceptions exist, BESS have to provide 100%P_0/Hz for under-frequency events, while PV are not required to increase their power in such events, due to the fact that a simple increase in power generation is physically impossible when running in their maximum power point.

The following plot in Fig. 5.3 illustrates the droop slopes including the exceptions and also highlights a very important aspect, the deadband of ±200 mHz in which no support has to be provided. The deadband is the reason most DG units are not at all participating in the frequency

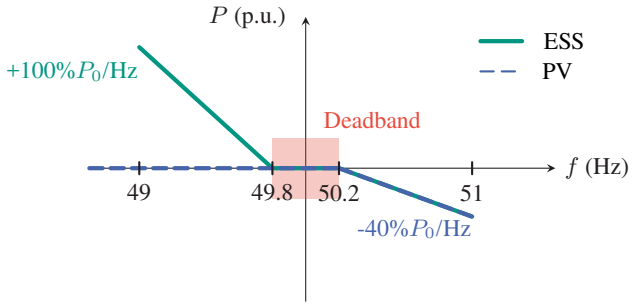

Figure 5.3: Active power to-frequency droop characteristic for newly connected generators in distribution grids, according to VDE AR-N 4105 [75].

control, since frequency deviations of more the 200 mHz rarely occur in the Central European interconnection grid. Testament to that is the fact, that even during the most recent black out event of the Iberian Peninsula in 2025 the frequency never reached a deviation of more than 200 mHz [136]. Therefore, simply using the droop characteristic to provide frequency response services is not sufficient and thus, the supportive features of the generators need to be triggered in a different way. One way to trigger the support is by adjusting the frequency in the connected downstream grid outside the boundaries of the deadband while still operating grid code compliant.

5.2.2 Frequency Propagation Concept

To exploit the power flexibility of renewable generators and passive loads alike, a control concept called *Frequency Propagation* is proposed. Enabled by the power electronic decoupling, the B2B converter allows the independent control of the downstream grid frequency and voltage magnitude. The general idea is to use the main grid frequency as set point for the downstream distribution grid with an additional gain to amplify and apply a frequency or voltage deviation. This leads to a scenario in which a slight frequency disturbance of 50 mHz in the main grid can be amplified to 300 mHz in the downstream grid supplied by the ASG, which results in an active power response by the connected renewable generators.

The concept is fully illustrated in Fig. 5.4 and can be described along the numbered stages. First of all a MVAC power imbalance ① on the bottom left causes a frequency disturbance ②. This frequency disturbance is measured (f_1), amplified, and used in the controller on the secondary

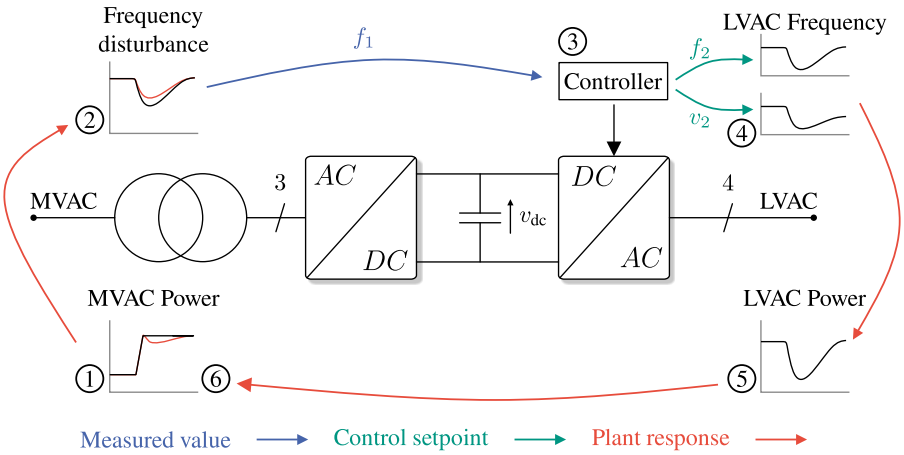

Figure 5.4: Frequency propagation concept to offer active power flow control for frequency response services, using an ASG (adapted from [J1]).

side of the B2B system ③ to alter the set point f_2 and/or v_2. In the case of an adaption of the downstream LVAC grid frequency f_2 (④ upper plot), renewable generators subsequently follow the required droop characteristic (Fig. 5.3) and adjust their active power injection/absorption ⑤, which in turn mitigates the power imbalance on the MVAC side ⑥. For an adjustment of the LVAC voltage v_2 (④ lower plot), the passive loads based on the previous load sensitivity adjust their active power consumption ⑤, which also leads to a MVAC side power imbalance mitigation ⑥. Both approaches can be used individually or in combination to exploit the full potential of the ASG for frequency response services.

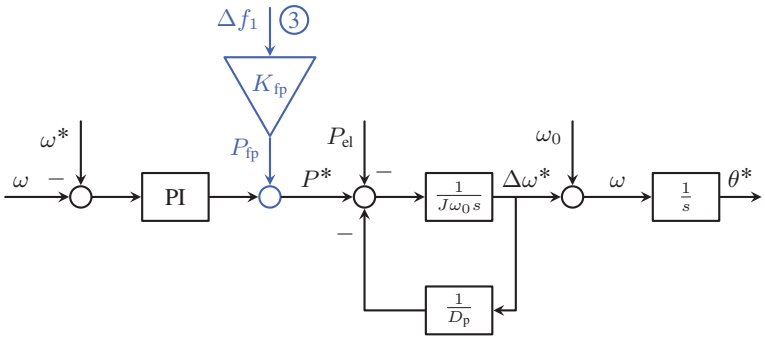

Figure 5.5: Enhanced VSM control structure with frequency propagation (in blue) to adapt the frequency (f_2) accordingly.

For the frequency adjustment, the earlier introduced controller (Fig. 2.17) is enhanced as illustrated in Fig. 5.5. The measured MVAC frequency deviation Δf_1 is multiplied by a propagation gain

K_{fp} (shown in blue ③) and then added as a feedforward term to the governor power set point of the VSM, thereby adjusting the LVAC frequency accordingly.

The controller for the voltage magnitude (Fig. 2.18) is similarly enhanced (in blue) with a propagation gain K_{vp} as shown in Fig. 5.6. This gain converts the same primary frequency deviation measurement Δf_1 into a voltage set point adjustment ΔV_{vp}, which leads to the final voltage set point V^*, for the cascaded voltage controller of the secondary side GFM converter.

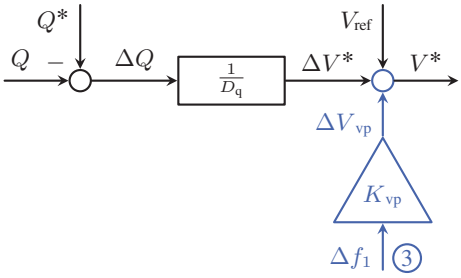

Figure 5.6: Enhanced voltage control structure with frequency-to-voltage propagation (in blue) to adapt the voltage (v_2) accordingly.

5.3 Open-loop Frequency Response Testing of Asynchronous Grid Connections in PHIL

The open-loop test of the frequency response refers to the open feedback loop on the primary side of the B2B PHIL setup, illustrated in Fig. 5.7, and highlighted by the open switch S_1, circled in red. This means that the actual active power flow based on the current i_1 is not fed back into the primary grid model, the SMM (introduced in Section 3.2.1). The feedback power $P_{\text{sup}}(i_1)$ in Fig. 3.5 is therefore not nullified. Thus, the SMM provides a realistic non-supported frequency disturbance signal that can be used as a contingency to trigger the frequency response concept of the ASG. The purpose of this scenario is the analysis and illustration of the propagation and amplification of the generated frequency contingency, leaving aside the bigger picture and its impact on the primary side grid for now.

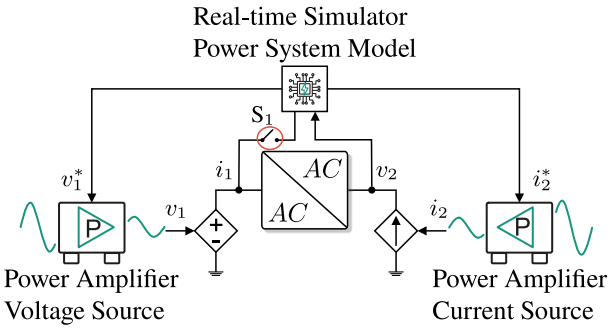

Figure 5.7: PHIL setup to test the ASG. The B2B converter is connected to two power amplifiers emulating the primary and secondary side grid respectively, controlled by a real-time simulator. The open-loop test is highlighted by the open switch S_1 (circled in red), which disconnects the feedback of the power flow to the primary grid model.

5.3.1 Active Power Flow Control exploiting Frequency Droop in Active Resources

The main steps of the open-loop test procedure are illustrated in Fig. 5.8, paired with plots on the right side of the respective electrical variables relevant for each step of the test.

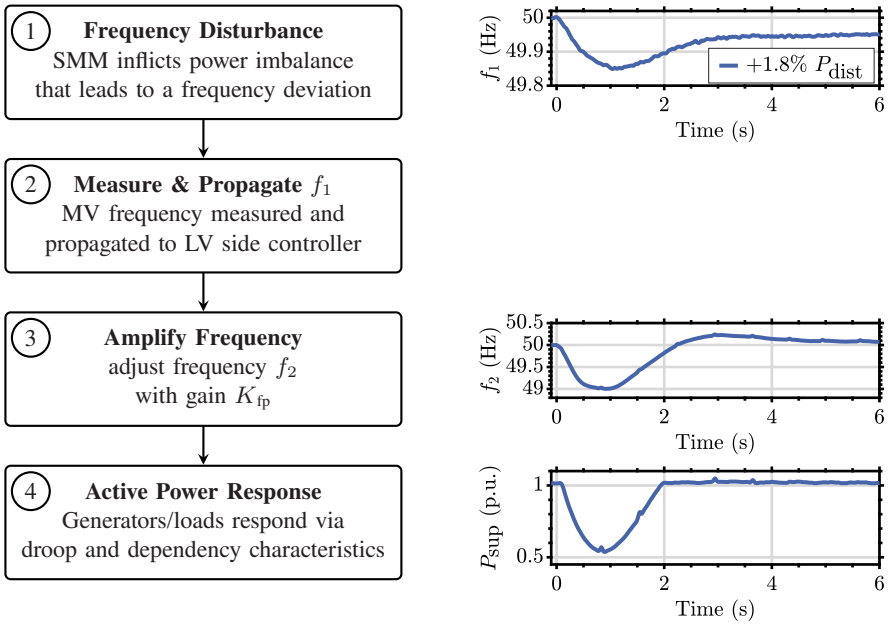

Figure 5.8: Illustration of the experimental process: frequency disturbance generation (Step 1), frequency propagation (Steps 2-3), and resulting active power response (Step 4).

The displayed plots are measurements from the base case scenario which includes an active power imbalance in the SMM of $\pm$ 1.8%, causing a frequency contingency with a nadir of $\pm$150 mHz, for base damping values of D=1 and an inertia of M=4 shown in the top right plot. The frequency contingency is subsequently propagated, amplified and used in the downstream distribution network GFM controller resulting in the frequency (f_2) of the center plot on the right. This case uses a gain of K_{fp} = 15 to amplify the frequency disturbance in f_1 to f_2. The devices in the downstream network are then following up with an active power change based on their droop characteristic, as introduced in Section 5.2.1, and plotted in the bottom right graph.

The active power consumption is reduced by roughly 0.4 p.u., which directly matches the active power capability of the connected BESS, being the only device capable of increasing the active power output and providing support in case of an under-frequency event. As discussed in previous paragraphs, grid standard VDE AR-N 4105 requires ESS to adjust their active power output for under frequency events by 100 %P_0/ Hz. In fact the steady-state active power operating point in this setup is at -6 kW (i.e. 6 kW active power consumption of the LV network), composed of -12 kW static Ohmic Load (R Load) and two systems that provide power to the grid, the BESS 4 kW and the PV 2 kW. At the nadir of 49 Hz the droop characteristic of the BESS causes the controller to increase the active power output to 8 kW, thus at the frequency nadir the active power consumption is decreased to -2 kW. More explicitly displayed in Eq. (5.11) and Eq. (5.12). This shows that the reduction in active power consumption actively mitigates the active power imbalance in the upstream grid, with the potential to support the frequency disturbance.

$$\text{Steady-State:} \quad -6\,\text{kW} = \overbrace{-12\,\text{kW}}^{\text{R Load}} + \overbrace{4\,\text{kW}}^{\text{BESS}} + \overbrace{2\,\text{kW}}^{\text{PV}} \tag{5.11}$$

$$\text{Nadir (49 Hz):} \quad -2\,\text{kW} = -12\,\text{kW} + 8\,\text{kW} + 2\,\text{kW} \tag{5.12}$$

In the following, multiple tests with varied parameters and different load compositions have been conducted. The important test parameters are summarized in Table 5.1, displaying two different load compositions the upper half with a high share of BESS capacity and the lower half with a high share of PV capacity. In addition, three different frequency propagation gains K_{fp} are tested for both positive and negative active power disturbances of $\pm$1.8%.

Table 5.1: Test case parameters for open-loop frequency response experiments.

Case No.	P_{dist} (p.u.)	K_{fp}	$P_{0,\text{BESS}}$ (kW)	$P_{0,\text{PV}}$ (kW)	$P_{0,\text{Rload}}$ (kW)
1	+1.8%	10	4	2	-12
2	+1.8%	12	4	2	-12
3	+1.8%	15	4	2	-12
4	-1.8%	10	4	2	-12
5	-1.8%	12	4	2	-12
6	-1.8%	15	4	2	-12
7	+1.8%	10	2	4	-12
8	+1.8%	12	2	4	-12
9	+1.8%	15	2	4	-12
10	-1.8%	10	2	4	-12
11	-1.8%	12	2	4	-12
12	-1.8%	15	2	4	-12

In Fig. 5.9 the experimental data for the test cases 1 to 6 with a high share of BESS capacity and a variation of the frequency propagation gain K_{fp} is displayed. The left column is dedicated to a positive active power disturbance of +1.8 % leading to a downward frequency contingency, while the right column shows the data for a negative active power disturbance of -1.8 % leading to an upward frequency contingency. The first row shows the primary frequency f_1 that triggers the frequency response algorithm of the ASG. Due to the open-loop testing, it can be seen that all frequency traces for f_1 are identical or, as in Fig. 5.9b, an axis mirrored version of Fig. 5.9a.

The second row subsequently displays the amplified LVAC frequency f_2 that is the result of the frequency propagation concept. Based on the parameter variation of K_{fp}, it can be seen in Fig. 5.9c that a higher gain leads to a more pronounced amplification, resulting in values of 49.5 Hz for K_{fp} = 10 and down to 49.0 Hz for K_{fp} = 15. The behavior is again mirrored for the positive power disturbance in Fig. 5.9d, leading to a LVAC frequency of 50.5 Hz for K_{fp} = 10 and up to 51.0 Hz for K_{fp} = 15. The bottom row of Fig. 5.9 eventually displays the active

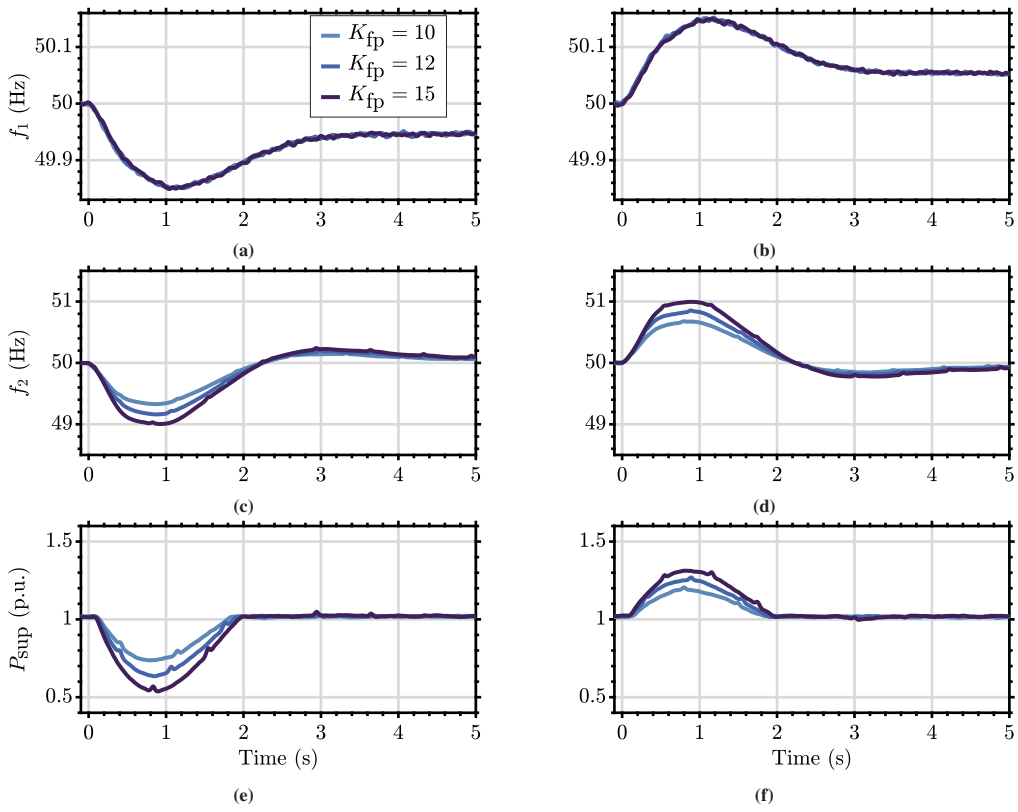

Figure 5.9: Propagation parameter (K_{fp}) variation test case of the B2B in open-loop connection within the proposed PHIL setup, for high shares of BESS. (a) and (b) show the initial frequency (f_1) on the primary side that triggers the frequency response of the LV side with the LV frequency (f_2) in (c) and (d) and the resulting active power flow adjustment in (e) and (f). The left column corresponds to a positive active power disturbance while the right column corresponds to a negative active power disturbance.

power response of the ASG. Two things can be observed here, first the active power response is more pronounced for higher values of K_{fp}, which is expected since a higher amplification of the frequency deviation leads to a stronger activation of the droop characteristic of the connected resources. Second, the active power response for the negative power disturbance in Fig. 5.9f is significantly lower compared to the positive power disturbance in Fig. 5.9e. This is again due to the fact that in an over-frequency event the connected resources only provide a 40 %P_0/ Hz active power decrease, while in an under-frequency event the BESS provides a full 100 %P_0/ Hz active power increase.

Fig. 5.10 subsequently displays the test cases 7 to 12 with a high share of PV capacity and the same variation of the frequency propagation gain K_{fp} as in cases 1 to 6.

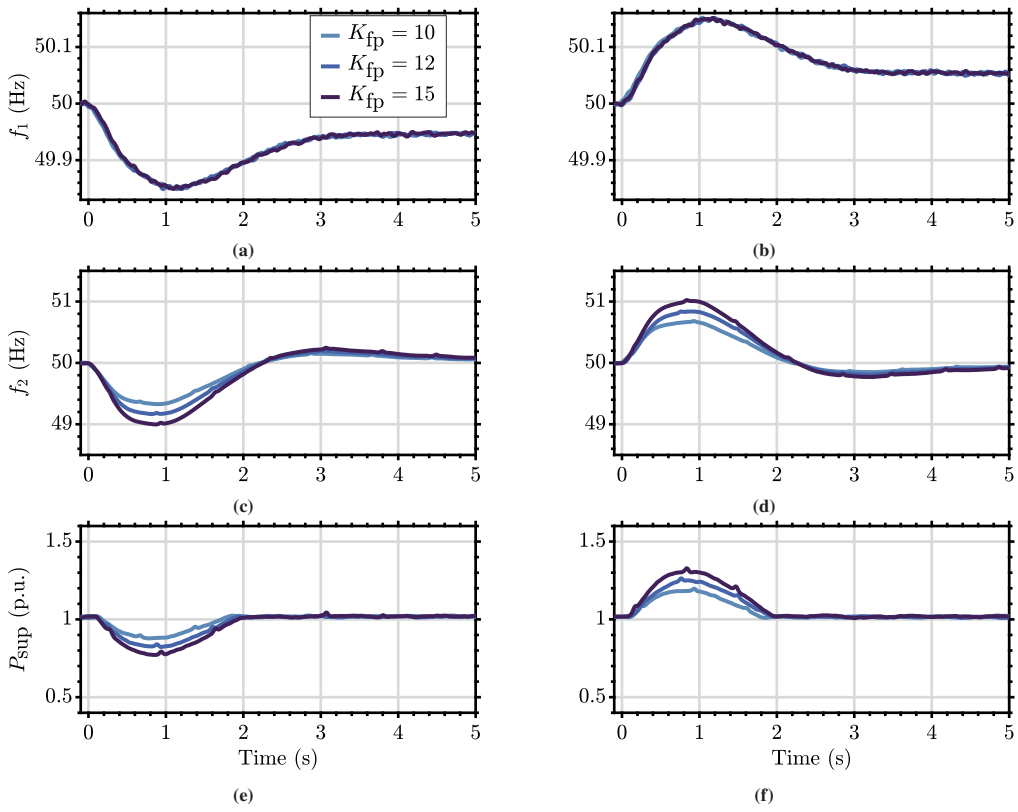

Figure 5.10: Propagation parameter (K_{fp}) variation test case of the B2B in open-loop connection within the proposed PHIL setup, for high shares of PV. (a) and (b) show the initial frequency (f_1) on the primary side that triggers the frequency response of the LV side with the LV frequency (f_2) in (c) and (d) and the resulting active power flow adjustment in (e) and (f). The left column corresponds to a positive active power disturbance while the right column corresponds to a negative active power disturbance.

The behavior is quite similar to the previous test cases and this is to be expected. Due to the fact that the results represent an open-loop configuration the traces from Fig. 5.10a to Fig. 5.10d show a consistent frequency disturbance (f_1) and subsequent amplification (f_2). What's striking, is the difference in the active power response in Fig. 5.10e compared to Fig. 5.9e and the similarities in Fig. 5.10f compared to Fig. 5.9f. In fact the active power response (Fig. 5.10e) in case of a positive power disturbance (+1.8 %) is only 51 % of the high BESS share case in Fig. 5.9e for K_{fp} = 15. The reason for that is, as explained in the beginning of this chapter, the different capability of the PV, which can only support over-frequency events. Therefore, in Fig. 5.10e only a BESS of 2 kW is participating in the frequency response mechanism which leads to the expected value of half of the previous 4 kW BESS. In Fig. 5.10f on the other hand the active power response for

the negative power disturbance (-1.8 %) is equal to the previous test case in Fig. 5.9f, since both the BESS and PV are participating equally, (40%P_0/Hz) in the over-frequency event.

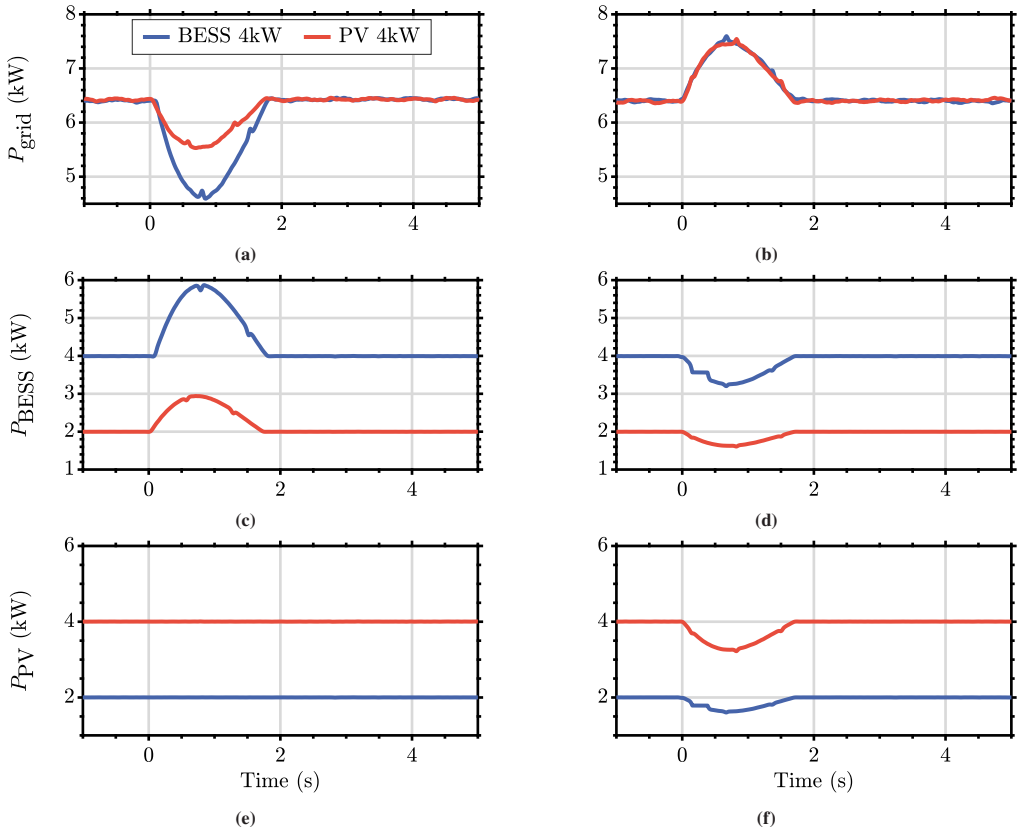

Figure 5.11: Active power response comparison between BESS-dominant (blue, cases 3 and 6) and PV-dominant (red, cases 9 and 12) configurations for negative (left) and positive (right) frequency disturbances with K_{fp} = 15. Top row (a) and (b) shows grid power, middle row (c) and (d) BESS power, bottom row (e) and (f) PV power.

To investigate this behavior in detail an additional set of plots is provided in Fig. 5.11 and Fig. 5.12. Fig. 5.11 offers a detailed comparative look at the total power response of the downstream LV grid with P_{grid} in Fig. 5.11a and Fig. 5.11b. As in the previous figure the left column shows the response for a positive active power disturbance (+1.8 %) and the right column for a negative active power disturbance (-1.8 %). The blue traces represent one case (3 and 6) for dominant BESS share in this 4 kW while the red traces represent the case with dominant PV share also at 4 kW nominal power (9 and 12), while the non-dominant resources operates at 2 kW. The second row with Fig. 5.11c and Fig. 5.11d is dedicated to the active power response of the BESS system and the bottom row with Fig. 5.11e and Fig. 5.11f to the active power response of the PV system.

It clearly shows the different power adjustment for the direction of the frequency disturbance. The BESS in Fig. 5.11c is providing a significant active power increase of nearly 50 % of its nominal power capacity, while in Fig. 5.11d the active power decrease is only around 20%, due to the different droop slopes required by the grid code. The PV system on the other hand in Fig. 5.11e is not providing any active power increase at all for under-frequency events, while in Fig. 5.11f it is providing a significant active power decrease in both cases reaching nearly 40 % of its nominal power capacity.

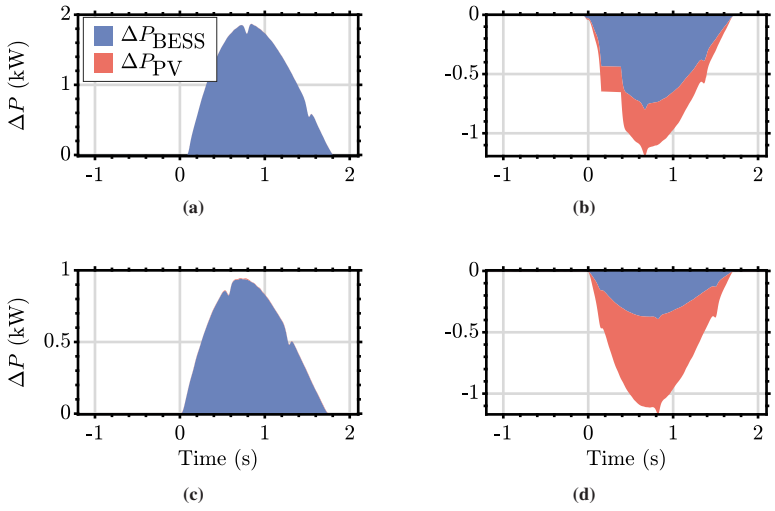

Figure 5.12: Power deviation comparison between BESS-dominant (top, (a) and (b)) and PV-dominant (bottom, (c) and (d)) configurations for negative (left) and positive (right) frequency disturbances with $K_{\text{fp}} = 15$.

Fig. 5.12 provides an even better direct comparison between the two types of resources, by displaying the power deviation ΔP from the initial operating point, here off set to 0. The top row shows the power deviation for the dominant cases (3 and 6) of BESS in Fig. 5.12a and Fig. 5.12b for negative and positive power disturbances respectively. The bottom row shows the power deviation for the dominant cases (9 and 12) of PV in Fig. 5.12c and Fig. 5.12d for negative and positive power disturbances respectively. The plotted areas highlight the significant difference between the two, which gets particularly visible in the left column (Fig. 5.12a and Fig. 5.12c), where no red area can be seen at all, since the PV system is not reacting. On the right side (Fig. 5.12b and Fig. 5.12d) on the other hand both PV systems are reacting strongly and showing the capability to reduce their active power output significantly.

5.3.2 Active Power Flow Control exploiting Voltage Dependencies

In contrast to the previous section, describing how active power flow control can be achieved through the control of the frequency (f_2) on the secondary side, this section revolves around the validation of the voltage (v_2) dependent active power flow control. Meaning, the frequency (f_2) on the secondary side is left untouched, while the voltage magnitude is adjusted, based on the test cases listed in Table 5.2. The voltage adjustment influences active power consumption of downstream resources and therefore adjust the active power flow through the ASG.

Table 5.2: Test case parameters for open-loop voltage response experiments.

Case No.	P_{dist} (p.u.)	K_{vp}	$P_{0,\text{BESS}}$ (kW)	$P_{0,\text{PV}}$ (kW)	$P_{0,\text{Rload}}$ (kW)
1	+1.8%	0.07	4	4	-12
2	+1.8%	0.08	4	4	-12
3	+1.8%	0.09	4	4	-12
4	+1.8%	0.10	4	4	-12
5	-1.8%	0.07	4	4	-12
6	-1.8%	0.08	4	4	-12
7	-1.8%	0.09	4	4	-12
8	-1.8%	0.10	4	4	-12

The results displayed in Fig. 5.13 show measurements from the open-loop PHIL experiments using the identical test setup as in Fig. 3.9, but now applying the amplified voltage disturbance to the voltage magnitude set point to synthesize (v_2) on the secondary side. The left column displays the results for a positive active power disturbance of +1.8 % leading to a downward frequency contingency, while the right column shows the data for a negative active power disturbance of -1.8 % leading to an upward frequency contingency. In the first row the primary frequency f_1 is shown triggering the propagation algorithm of the ASG, with a subsequent adjustment of the LVAC voltage v_2. The second row shows the RMS value in p.u. in downward (Fig. 5.13c) and upward direction (Fig. 5.13d). The adjustment of the voltage magnitude is based on the gain value K_{vp} and is varied in the displayed cases starting from 0.07 to 0.1 in increments of 0.01. It can be observed that a higher gain leads to a more pronounced voltage adjustment, resulting in values of roughly 0.94 p.u. for K_{vp} = 0.07 and down to 0.915 p.u. for K_{vp} = 0.1 in the downward direction (Fig. 5.13c). The behavior is again mirrored for the upward direction in Fig. 5.13d, leading to a LVAC voltage of roughly 1.05 p.u. for K_{vp} = 0.07 and to nearly 1.10 p.u. for K_{vp} = 0.1.

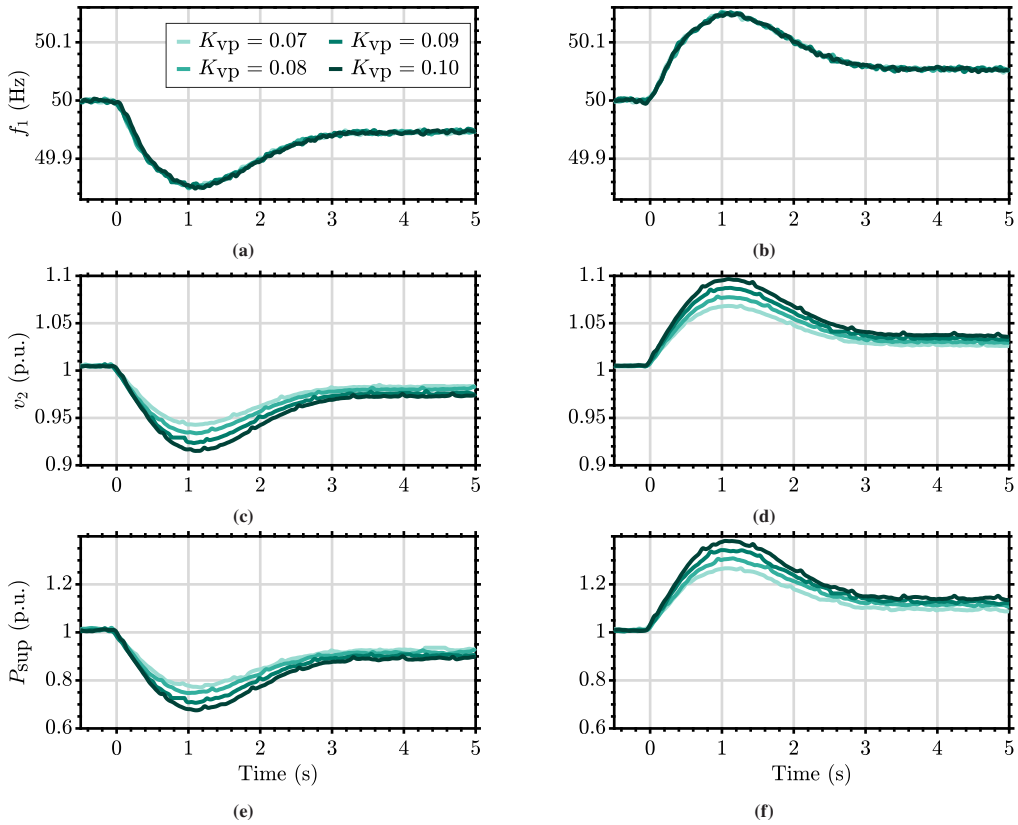

Figure 5.13: Propagation parameter (K_{vp}) variation test case of the B2B in open-loop connection within the proposed PHIL setup. (a) and (b) show the initial frequency (f_1) on the primary side that triggers the response of the LV side with the voltage magnitude (v_2) in (c) and (d) and the resulting active power flow adjustment in (e) and (f). The left column corresponds to a positive active power disturbance, while the right column corresponds to a negative active power disturbance.

Since the active power flow for these test cases is based on the reaction of passive components, the active power adjustment is directly proportional to the voltage deviation. This can be observed in the bottom row in Fig. 5.13d and Fig. 5.13c, displaying the active power adjustment (P_{sup}) of the ASG. Similar to the voltage, here the active power adjustment increases with the gain value of K_{vp}. In the downward direction (Fig. 5.13e) the active power adjustment is reduced by 23 % for K_{vp} = 0.07 and up to 32 % for K_{vp} = 0.1. The upward direction in Fig. 5.13f again mirrors the behavior resulting in an active power adjustment of 27 % for K_{vp} = 0.07 and 38 % for K_{vp} = 0.1.

This set of experiments on its own leads to the question can this power flexibility operate in conjunction with each other, exploiting both voltage and frequency dependencies while using the

flexibility for frequency support on the primary side? Thus, the next subsection show results for the open-loop combined testing of both voltage and frequency propagation.

5.3.3 Active Power Flow Control exploiting combined Frequency Droop and Voltage Dependencies

The following Fig. 5.14 displays the results for a combined voltage and frequency propagation test case in open-loop configuration.

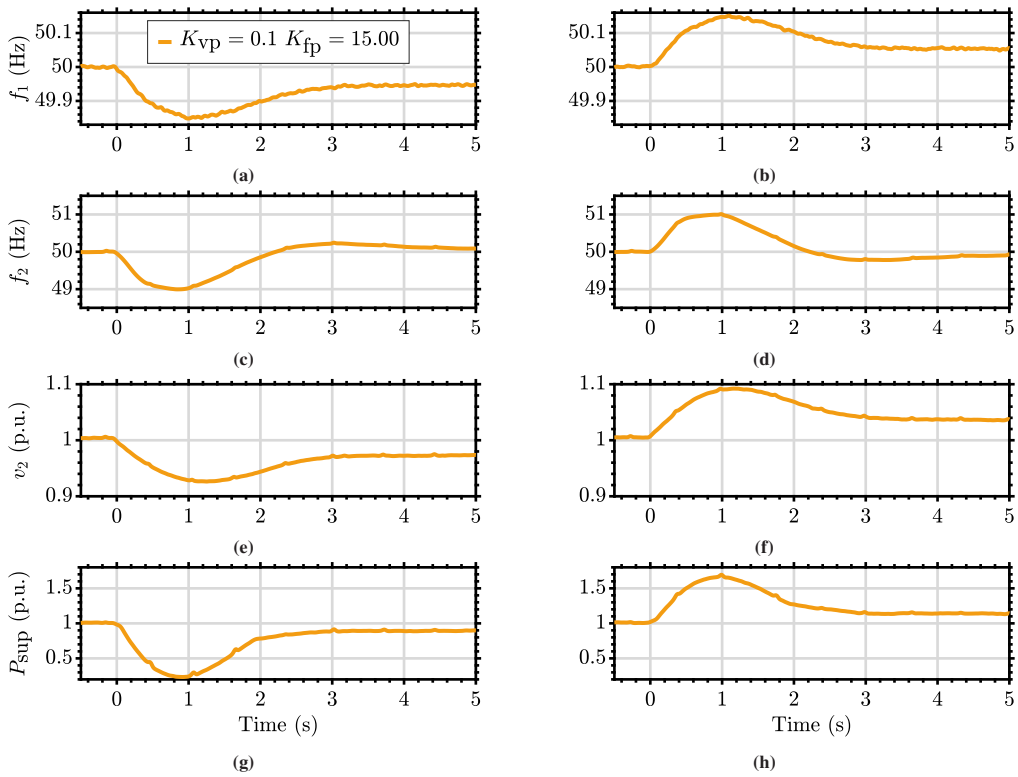

Figure 5.14: Active power response for a combined voltage and frequency control with a case for negative (left column) and positive (right column) frequency disturbances with K_{fp} = 15 and K_{vp} = 0.1. Top row (a) and (b) shows the primary frequency f_1, 2nd row (c) and (d) secondary frequency f_2, 3rd row display the secondary voltage v_2 in (e) and (f), and the bottom row (g) and (h) the active power P_{sup}.

As in the previous sections the left column shows the results for a positive active power disturbance of +1.8 % (downward frequency contingency), while the right column shows the data for a negative active power disturbance of -1.8 % (upward frequency contingency). The rows show the following

data: in the top row the primary frequency f_1 is displayed with the initial frequency contingencies; the second row shows the amplified LVAC frequency f_2 on the secondary side; the third row displays the secondary voltage magnitude v_2 as per unit RMS value; and the bottom row shows the resulting active power adjustment P_{sup} of the ASG. Both cases use a single set of parameters to highlight the general concept and behavior with $K_{\text{fp}} = 15$ and $K_{\text{vp}} = 0.1$.

Due to the fact that the displayed results are collected in an open-loop setup, the first three rows are basically identical to the previously presented data of the respective parameter combinations. The main insight is visualized in the bottom row plots Fig. 5.14g and Fig. 5.14h. Here, the active power adjustment P_{sup} is a result of the combined voltage dependency of the passive loads and the droop characteristics of the active resources connected to the secondary LV grid. It can be seen that the maximum power adjustment is reached before the 1 s mark, which correlates directly with the frequency propagation peak timing. The long-term trace shows a constant offset due to the non-integral behavior of the voltage controller. This shows the impact of both control concepts on the final active power adjustment. In the next subsection a direct comparison of the individual methods is presented.

5.3.4 Active Power Flow control Comparison between Frequency Droop, Voltage Dependency and the combined Method

The data presented so far shows the general behavior and power flexibility of the downstream LV grid for different methods of active power control. Fig. 5.15 displays these methods in the context of each other to provide a direct comparison of their capabilities. As for all the presented results, the left column shows the negative frequency contingency case, while the right column shows the positive frequency contingency case. The top row in Fig. 5.15a and Fig. 5.15b displays the primary frequency f_1 for all cases, which due to the open-loop nature is identical for all methods. The bottom row in Fig. 5.15c and Fig. 5.15d subsequently show the traces for the active power adjustment P_{sup}.

In Fig. 5.15 the differences between the tested methods really stand out. The blue trace representing the isolated frequency propagation method, has a quick and strong response in the beginning, with the fastest settling to the original operating point. The green trace representing the isolated voltage propagation method on the other hand shows a slower and weaker response that lasts longer and shows the lack of the integral behavior as expected. The yellow trace eventually shows the result of the combined voltage and frequency propagation methods. The combined characteristics of both methods - a fast and strong initial response due to the frequency propagation, which is then sustained at a higher level due to the voltage propagation method - is clearly demonstrated. Those

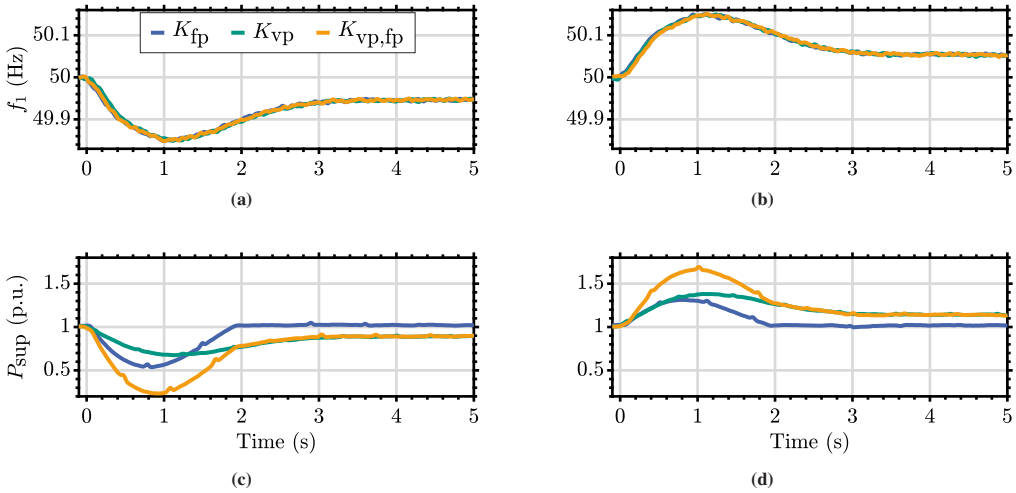

Figure 5.15: Comparison of the active power adjustment between the frequency propagation (in blue), the voltage propagation (in green) and the combined voltage and frequency propagation (in yellow) method for both negative (left column) and positive (right column) frequency disturbances with $K_{fp} = 15$ and $K_{vp} = 0.1$. Top row (a) and (b) shows the primary frequency f_1, and the bottom row (c) and (d) the active power adjustment P_{sup} for the different control algorithms.

results highlight the advantages of exploiting both dependencies at the same time to maximize the active power flexibility of the downstream LV grid.

5.4 Closed-loop Frequency Response Testing of the Asynchronous Grid Connection in PHIL

For a holistic analysis the feedback loop on the primary side of the B2B PHIL setup is closed. The whole loop including the power feedback is illustrated in Fig. 5.16. In contrast to the open-loop configuration, the actual active power flow based on the current i_1 is now fed back into the primary grid model, indicated by the closed switch S_1, circled in red.

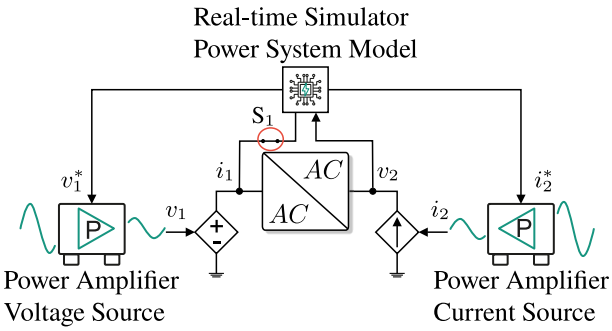

Figure 5.16: Closed-loop PHIL concept with the B2B in the center and the now closed feedback loop, represented by the closed switch S_1 circled in red.

The SMM functioning as the primary grid model, therefore includes the scaled feedback power $P_{\text{sup}}(\alpha_{\text{pen}})$ as defined in Section 3.2.1, and illustrated, and highlighted in red color, in Fig. 5.17. This setup provides a realistic frequency disturbance signal that can be influenced by the frequency response concept of the ASG. Thus, the purpose of this scenario is the analysis and validation of the complete frequency response mechanism, including the impact on the primary side grid and the effectiveness of the proposed control concept in a realistic power system environment.

The analysis reiterates the same test cases and parameter variations of the open-loop section in Section 5.3, including different propagation gain values (K_{fp}, K_{vp}), resource composition and different exploitation strategies (e.g., frequency droop and voltage dependencies). In addition, the impact of the active power response on the systems frequency is investigated along with varied penetration rating of the ASG concept. The boundary conditions and base parameters such as the power ratings for BESS and PV dominant cases, their controls (e.g., droop settings) and LV CIGRE grid configuration remain consistent with those outlined in Section 5.3 to ensure consistency across all tests. The following subsections present the experimental results for the closed-loop PHIL tests.

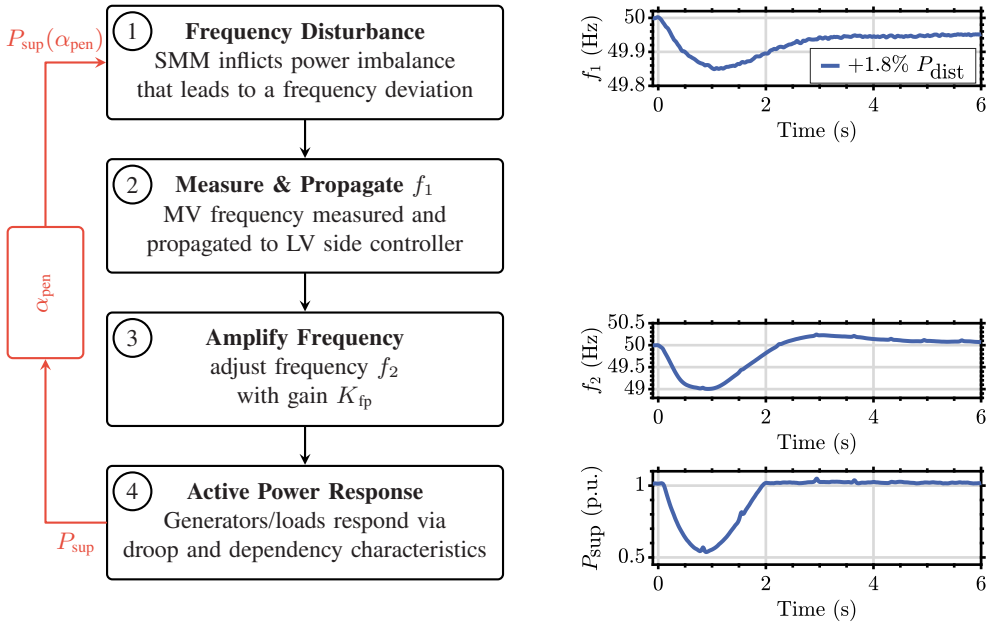

Figure 5.17: Illustration of the experimental process: frequency disturbance generation (Step 1), frequency propagation (Steps 2-3), and resulting active power response (Step 4) with the closed feedback loop to the SMM in red.

5.4.1 Closed-loop Frequency Response Testing exploiting Frequency Droop in Active Resources

Table 5.3 lists and Fig. 5.18 visualizes the first BESS dominant test cases (cases 1 to 5). The top row contrasts the base case (red) - an unsupported frequency disturbance without any active power feedback - with the closed-loop responses (shades of blue) for increasing K_{fp}. The left column of Fig. 5.18a shows a +1.8 % power demand increase (under frequency), while the right column of Fig. 5.18b shows a -1.8 % demand decrease (over frequency). The magnified frequency plot highlights reduced deviations, lower nadirs, and smaller RoCoFs for higher propagation gains.

With a penetration scaling of α_{pen} = 1 % of ASG active power capacity, the nadir and RoCoF improve by up to 25 % and 30 %, respectively, at the highest gain $K_{fp} = 20$. The lower rows display the secondary side frequency f_2 (Fig. 5.18c, Fig. 5.18d) and the adjusted active power flow P_{sup} (Fig. 5.18e, Fig. 5.18f). Both quantities exhibit the same behavior as observed in the open-loop experiments, a higher propagation gain leads to a stronger frequency adjustment on the secondary side and a larger active power response of the ASG.

For simulated load reductions (negative disturbance power, P_{dist} = -1.8, %), which cause an over-frequency, the frequency rise is likewise mitigated by the reduced power consumption of the ASG,

Table 5.3: Closed-loop frequency response test cases with BESS and PV dominance, and varying K_{fp} and α_{pen}.

Case No.	P_{dist}	α_{pen} (%)	K_{fp}	$P_{0,\text{BESS}}$ (kW)	$P_{0,\text{PV}}$ (kW)	f_1 Nadir	RoCoF (Hz/s)
Base	+1.8 %	0.0	0.0	4	2	49.849	-0.205
0	+1.8 %	1.0	12.5	4	2	49.872	-0.165
1	+1.8 %	1.0	15.0	4	2	49.877	-0.169
2	+1.8 %	1.0	20.0	4	2	49.887	-0.143
Base	-1.8 %	0.0	0.0	4	2	50.151	0.205
3	-1.8 %	1.0	12.5	4	2	50.136	0.194
4	-1.8 %	1.0	15.0	4	2	50.133	0.186
5	-1.8 %	1.0	20.0	4	2	50.126	0.179
Base	+1.8 %	0.0	0.0	2	4	49.849	-0.205
6	+1.8 %	1.0	12.5	2	4	49.863	-0.194
7	+1.8 %	1.0	15.0	2	4	49.867	-0.192
8	+1.8 %	1.0	20.0	2	4	49.870	-0.186
Base	-1.8 %	0.0	0.0	2	4	50.131	0.205
9	-1.8 %	1.0	12.5	2	4	50.137	0.194
10	-1.8 %	1.0	15.0	2	4	50.131	0.191
11	-1.8 %	1.0	20.0	2	4	50.126	0.182

as shown in the left column of Fig. 5.18. The base case (red dashed trace) depicts the unsupported frequency f_1 and exhibits a much higher peak nadir than the supported cases (blue shades). A higher propagation gain K_{fp} again corresponds to a lower nadir and reduced RoCoF. However, because the generation resources have a different droop response when increasing active power, the overall impact is smaller than for the under-frequency disturbances. As reported in Table 5.3, the maximum reductions in nadir and RoCoF are about 16.5 % and 14.5 %, respectively, for the largest gain $K_{\text{fp}} = 20$. The bottom two rows reflect this behavior: frequency propagation is similarly strong as in the under-frequency case, but the active-power response is substantially smaller and does not reach the same levels. For example, at $K_{\text{fp}} = 20$ the peak active power adjustment in the under-frequency case is close to 50 %, whereas in the over-frequency case it is only about 35 %.

The nadir reduction metric presented above and in the following is calculated as the relative reduction in frequency deviation as follows:

$$\Delta\text{Nadir} = \left(1 - \frac{|f_{\text{nadir,support}} - f_0|}{|f_{\text{nadir,base}} - f_0|}\right) \cdot 100\,\% \tag{5.13}$$

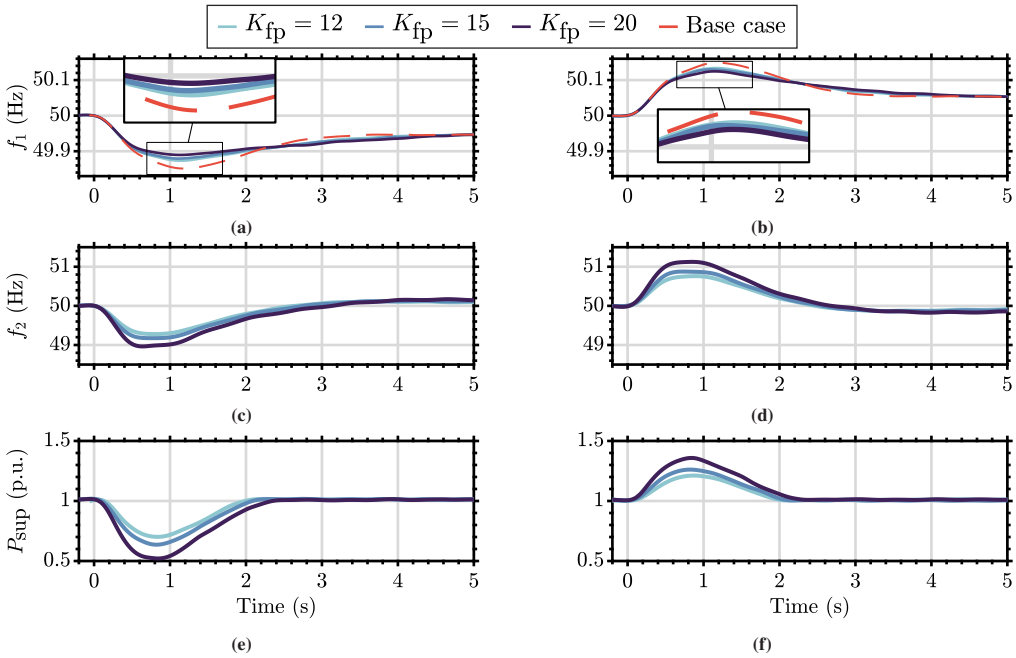

Figure 5.18: Closed-loop frequency propagation test results for a BESS-dominant configuration, with varying K_{fp} parameter and negative and positive disturbance (left and right column). The sub figures (a) and (b) show the MV frequency response with and without support (Base Case in red), (c) and (d) show the LV frequency propagation (f_2), (e) and (f) display the active power response. The higher the propagation gain K_{fp}, the darker the shade of the data trace.

where $f_0 = 50\,\text{Hz}$ and $\text{f}_{\text{nadir,base}}$ is the observed nadir frequency in the base case. The RoCoF improvement is similarly computed as:

$$\Delta\text{RoCoF} = \left(1 - \frac{|\text{RoCoF}_{\text{support}}|}{|\text{RoCoF}_{\text{base}}|}\right) \cdot 100\,\% \tag{5.14}$$

with the $\text{RoCoF}_{\text{base}}$ being the RoCoF of the unsupported base case. The RoCoF is calculated as the maximum slope of the frequency curve within the first 500 ms after the disturbance event. A detailed description of the RoCoF calculation methodology is provided in the Appendix (A.1).

The results for the PV-dominant configuration are presented in Fig. 5.19 and the lower half of Table 5.3 (cases 6-11). The general structure and behavior, mirror the ones observed in the BESS-dominant cases. The primary frequency f_1 displayed in the top row, the amplified secondary frequency f_2 in the middle row, and the active power response P_{sup} in the bottom row. However, the resource composition significantly affects the magnitude and symmetry of the provided frequency disturbance mitigation.

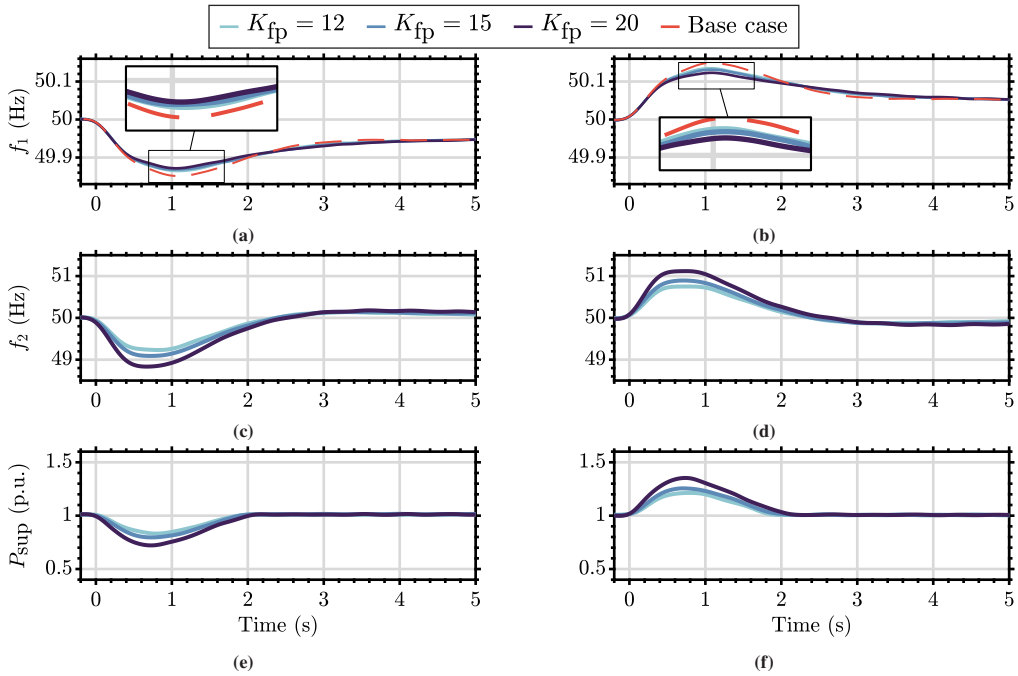

Figure 5.19: Closed-loop frequency propagation test results for a PV-dominant configuration, with varying K_{fp} parameter and negative and positive disturbance (left and right column). The sub figures (a) and (b) show the MV frequency response with and without support (Base Case in red), (c) and (d) show the LV frequency propagation (f_2), (e) and (f) display the active power response. The higher the propagation gain K_{fp}, the darker the shade of the data trace.

For positive power disturbances (+1.8 %, under-frequency events, left column), the frequency support is considerably weaker compared to the BESS-dominant cases. As shown in Fig. 5.19a, the reduction in nadir and RoCoF is limited, with maximum improvements of approximately 14 % and 9 % respectively for K_{fp} = 20 (see Table 5.3). This reduced effectiveness stems from the fact that only the 2 kW BESS participates in the under-frequency response, as the PV systems cannot increase their power output beyond their maximum-power-point. The active power response in Fig. 5.19e reflects this limitation, reaching only approximately 25 % of the nominal downstream grid capacity, compared to nearly 50 % in the BESS-dominant configuration. In contrast, for negative power disturbances (-1.8 %, over-frequency events, right column), the PV-dominant configuration demonstrates comparable performance to the BESS-dominant cases. Both the 2 kW BESS and the 4 kW PV system participate according to their 40 %P_0/Hz droop characteristic. As illustrated in Fig. 5.19b, the nadir and RoCoF reductions reach approximately 17 % and 11 % respectively for K_{fp} = 20. The active power response shown in Fig. 5.19f achieves

similar magnitudes to the BESS-dominant cases, demonstrating the significant contribution of PV curtailment during over-frequency events.

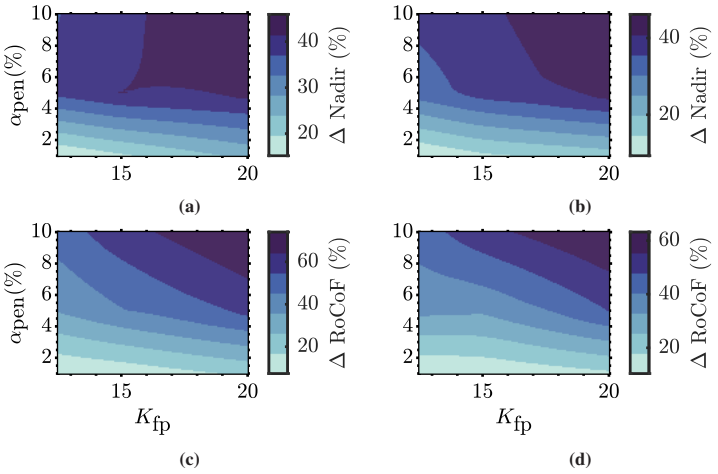

Figure 5.20: Closed-loop frequency nadir surface plot for BESS (a) and PV-dominant (b) configuration with the α_{pen} on the y-axis and the frequency propagation gain K_{fp} on the x-axis.

For a comprehensive analysis of the conducted tests, the frequency nadir and RoCoF results from both BESS and PV-dominant configurations are summarized in Table 5.4 with metrics visualized in Fig. 5.20. The illustrations depict the improved nadir (in %) and the reduced RoCoF (in Hz/s) as functions of α_{pen} (y-axis) and the frequency propagation gain K_{fp} (x-axis). Due to the previously outlined advantages of both compositions towards specific scenarios, the BESS dominant plots in the left column are based on results from under-frequency test cases and the right column PV dominant cases use data from over-frequency disturbances. The color scale ranges from light to dark blue, for low and high reductions of nadir and RoCoF respectively. It is evident that a higher penetration percentage (α_{pen}) provides the highest impact on the nadir reduction, while an increase of the propagation gain K_{fp} does have an effect as well, but to a lesser extent. This behavior is consistent for both resource compositions, although the BESS-dominant configuration generally achieves slightly better performance due to its ability to both increase and decrease power output. This can be seen in the size of the dark blue areas in Fig. 5.20a and Fig. 5.20b, indicating lower nadir values. Concerning the RoCoF the trend is similar, for the BESS-dominant resource composition as shown in Fig. 5.20c, the RoCoF improvement is equally based on penetration (α_{pen}) and propagation gain. In test cases for higher PV dominance, the impact of the propagation gain is not as consistent as the penetration percentage. This reveals itself in the gradient borders, which do not all decrease linearly toward the right side of the plot. Instead, they show some bumps. For example, a K_{fp} of 12.5 and 15 does not yield a significant improvement of the

Table 5.4: Combined test case parameters for closed-loop frequency response experiments with varying K_{fp} and α_{pen}, under BESS and PV dominance.

		BESS dominant			PV dominant		
α_{pen}	K_{fp}	Nadir f_1 (Hz)	RoCoF (Hz/s)	Δ Nadir	Nadir f_1 (Hz)	RoCoF (Hz/s)	Δ Nadir
0.0 %	0.0	49.849	-0.205	0.00 %	50.151	0.205	0.00 %
1.0 %	12.5	49.872	-0.165	15.23 %	50.137	0.194	9.33 %
5.0 %	12.5	49.907	-0.107	38.41 %	50.102	0.118	32.85 %
10.0 %	12.5	49.905	-0.060	37.09 %	50.095	0.120	37.43 %
1.0 %	15.0	49.877	-0.169	18.54 %	50.131	0.191	13.31 %
5.0 %	15.0	49.912	-0.109	41.72 %	50.094	0.143	37.84 %
10.0 %	15.0	49.910	-0.052	40.40 %	50.091	0.101	39.77 %
1.0 %	20.0	49.887	-0.143	25.17 %	50.126	0.182	16.80 %
5.0 %	20.0	49.914	-0.064	43.05 %	50.086	0.112	43.38 %
10.0 %	20.0	49.919	-0.032	46.36 %	50.081	0.080	46.18 %

RoCoF, but a change of the α_{pen} for the same propagation gain does. However, this behavior only appears at low α_{pen} ranges (e.g., 1 % and 5 %) and evens out for higher penetration percentages (e.g., 10 %).

5.4.2 Closed-loop Frequency Response Testing exploiting Voltage Dependencies

The voltage-based closed-loop experiments are conducted using the same scenario settings as the frequency propagation tests, with the key difference being the adjustment of the voltage magnitude v_2 rather than the frequency f_2 on the secondary side. As established in the open-loop analysis (Section 5.3.2), this approach exploits the voltage dependence of passive loads to achieve active power adjustments. The closed-loop configuration now investigates the impact of the proposed method on the primary frequency disturbance.

Fig. 5.21 presents the experimental results for voltage propagation in closed-loop configuration, based on the cases defined in Table 5.5. In alignment with the previous results the left column in Fig. 5.21 shows results for a positive active power disturbance (+1.8 %, under-frequency), while the right column presents data for a negative disturbance (-1.8 %, over-frequency). The voltage propagation gain K_{vp} is varied from 0.07 to 0.12, with the parameter details summarized in Table 5.5. The top row (Fig. 5.21a and Fig. 5.21b) compares the primary frequency f_1 response

Table 5.5: Test case parameters for closed-loop voltage response experiments with varying voltage propagation gains.

Case No.	α_{pen} (%)	K_{vp}	$P_{0,\text{Rload}}$ (kW)	Nadir f_1 (Hz)	RoCoF (Hz/s)
Base Case	0.0	0.0	-12	49.849	-0.205
1	1.0	0.07	-12	49.866	-0.188
2	1.0	0.08	-12	49.867	-0.192
3	1.0	0.09	-12	49.868	-0.186
4	1.0	0.10	-12	49.868	-0.194
Base Case	0.0	0.0	-12	50.151	0.205
5	1.0	0.07	-12	50.135	0.191
6	1.0	0.08	-12	50.133	0.188
7	1.0	0.09	-12	50.134	0.188
8	1.0	0.10	-12	50.128	0.185

between the unsupported base case (red dashed) and voltage-supported cases (green shades), with magnified insets highlighting the nadir region. The middle row displays the adjusted secondary voltage magnitude v_2 (Fig. 5.21c and Fig. 5.21d), while the bottom row shows the resulting active power adjustment P_{sup} (Fig. 5.21e and Fig. 5.21f).

The magnified region in Fig. 5.21a and Fig. 5.21b clearly show the nadir reduction achieved by utilizing the active power flow control based on voltage dependencies compared to the non-support cases in (red dashed). The green shades represent the different propagation gains K_{vp}, with darker shades indicating higher gains. One can observe the proportional relationship between the increased propagation gain K_{vp} and the extent to which the LVAC voltage magnitude v_2 is adjusted (Fig. 5.21c and Fig. 5.21d). This adjustment is subsequently visible in the active power flow response P_{sup} depicted in Fig. 5.21e and Fig. 5.21f. This enhanced active power flow effectively mitigates the frequency deviation in the primary grid, as evidenced by the metric displayed in Table 5.5. Here, the nadir frequency f_{nadir} and RoCoF values are summarized for each test case, demonstrating the beneficial impact of voltage-based active power flow control in closed-loop operation. The nadir values show a consistent reduction compared to the base case, by at least 10 % and up to 14.6 %. In the very right column the RoCoF values do not display a picture that clear. The data shows a clear reduction of the RoCoF, between the base case and the support cases, but the trend for an increase in propagation gain does not align directly with the reduction of the RoCoF.

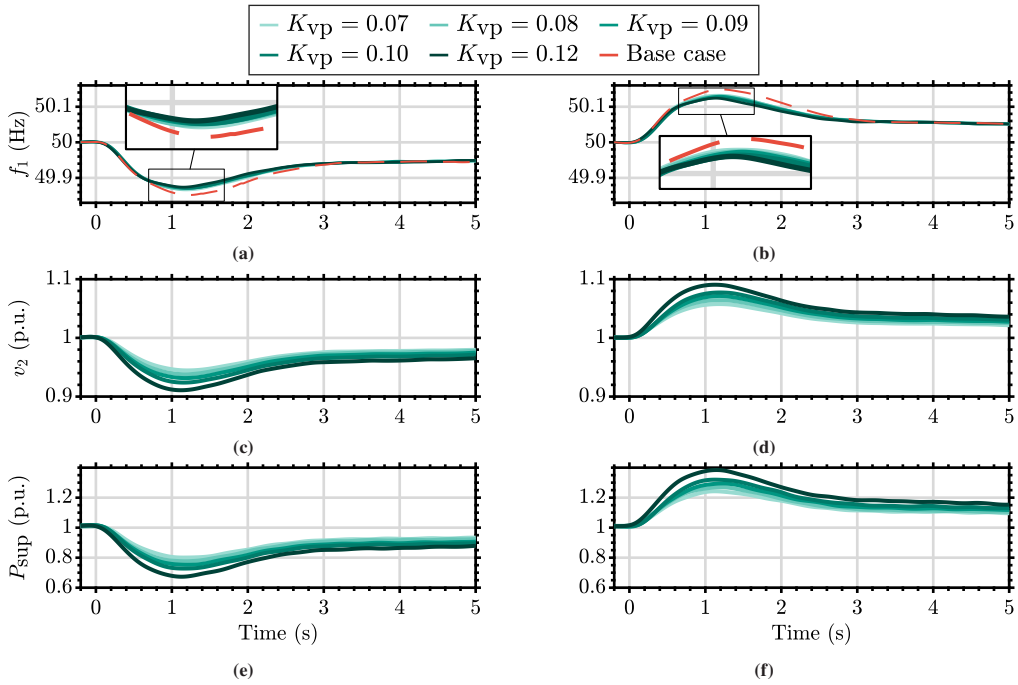

Figure 5.21: Closed-loop frequency to voltage propagation test results, with varying K_{vp} parameter and negative and positive disturbance (left and right column). The sub figures (a) and (b) show the MV frequency response with and without support (Base Case in red), (c) and (d) show the LV voltage magnitude (v_2), (e) and (f) display the active power response. The higher the propagation gain K_{vp}, the darker the shade of the data trace.

The RoCoF calculation uses a slide window average to mitigate noise impact and rule out any measurement artifacts, the detailed RoCoF calculation can be found in the Appendix A. Nevertheless, for future implementations of the voltage dependent frequency response concept, the amount of test cases need to be increased, to identify a clear trend of the RoCoF reduction in relation to the propagation gain K_{vp}.

For a deeper look into the data including the variation of the penetration percentage (α_{pen}), two surface plots are provided in Fig. 5.22. These plots depict the parameter variation of the propagation gain K_{vp} (x-axis) and the penetration percentage α_{pen} (y-axis) against the nadir reduction (in %) in Fig. 5.22a and the RoCoF reduction (in %) in Fig. 5.22b. Both plots illustrate a clear trend showing that the nadir and RoCoF improve with increasing penetration percentage. The effect of the propagation gain K_{vp} is also visible, but only to a limited extent, represented by the slight decline of the color borders from left to right. This shows that for the same α_{pen} the nadir reduction can be improved by increasing the propagation gain K_{vp}. In the uncovered area of the surface plots, the system has not been tested yet.

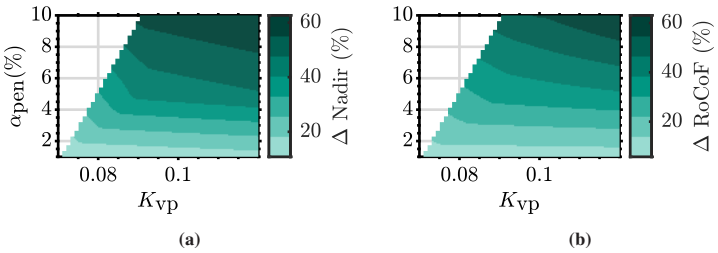

Figure 5.22: Closed-loop frequency nadir and RoCoF surface plot for the voltage dependent active power flow control with the penetration percentage α_{pen} on the y-axis and the frequency to voltage propagation gain K_{vp} on the x-axis.

Table 5.6: Nadir and RoCoF metrics for closed-loop voltage-dependent frequency response experiments across varying K_{vp} and α_{pen}.

α_{pen}	K_{vp}	Nadir f_1	Δ Nadir	RoCoF (Hz/s)	Δ RoCoF
0.0 %	0.0	49.849 Hz	0.0 %	-0.205 Hz/s	0.0 %
1.0 %	0.07	49.866 Hz	10.8 %	-0.188 Hz/s	8.6 %
1.0 %	0.08	49.867 Hz	11.9 %	-0.192 Hz/s	6.7 %
1.0 %	0.09	49.868 Hz	12.5 %	-0.186 Hz/s	9.6 %
1.0 %	0.10	49.868 Hz	12.6 %	-0.194 Hz/s	5.8 %
1.0 %	0.12	49.871 Hz	14.6 %	-0.187 Hz/s	9.3 %
5.0 %	0.09	49.914 Hz	42.7 %	-0.136 Hz/s	33.7 %
5.0 %	0.10	49.919 Hz	46.3 %	-0.124 Hz/s	39.7 %
5.0 %	0.12	49.920 Hz	47.2 %	-0.128 Hz/s	37.5 %
10.0 %	0.09	49.936 Hz	57.3 %	-0.101 Hz/s	50.9 %
10.0 %	0.10	49.940 Hz	60.1 %	-0.090 Hz/s	56.1 %
10.0 %	0.12	49.944 Hz	62.6 %	-0.076 Hz/s	63.1 %

An overview of all conducted test cases and their respective results, is given in Table 5.6. The data further emphasizes the big impact of the penetration percentage on the frequency response performance and the achievable reductions of nadir and RoCoF, respectively. The high α_{pen} cases of 10 % show a nadir reduction of up to 62.6 % and a RoCoF reduction of 63.1 %, which is a significant improvement compared to the base case without any support functionality.

5.4.3 Closed-loop Frequency Response Testing exploiting combined Frequency Droop and Voltage Dependencies

The last set of experiments investigates the combined frequency response concept exploiting both frequency droop and voltage dependencies for the control of the active power flow through the B2B converter. This approach activates both the propagation of f_1 to adjust the secondary frequency f_2 and the voltage magnitude v_2 at the same time.

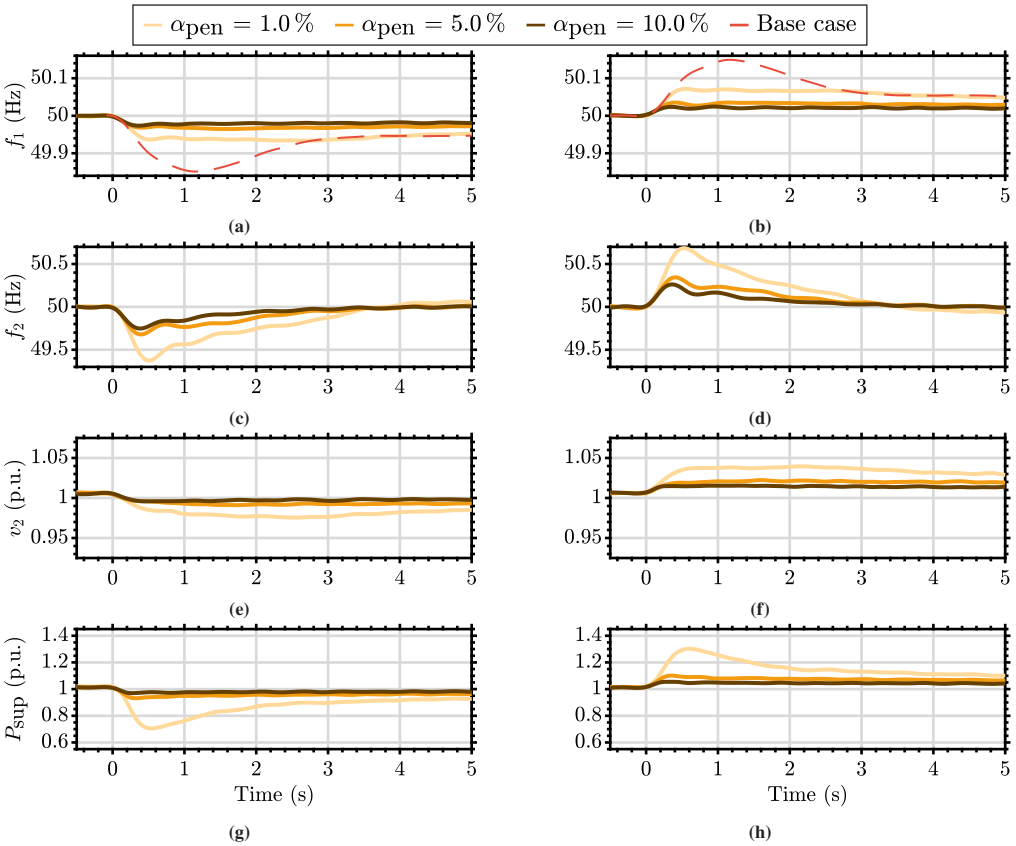

Figure 5.23: Closed-loop combined voltage and frequency propagation results with a case for negative (left column) and positive (right column) frequency disturbance with different penetration percentages (α_{pen} = 1 %, 5 % and 10 %). Top row (a) and (b) shows the primary frequency f_1, 2nd row (c) and (d) secondary frequency f_2, 3rd row displays the secondary voltage v_2 in (e) and (f), and the bottom row (g) and (h) the active power P_{sup}.

The conducted tests follow the same scenario settings as the previous closed-loop experiments. This offers the opportunity to explore a wide variety of parameter variations including combinations of propagation gains K_{fp} and K_{vp}, different resource compositions, and penetration percentages. For the sake of clarity, this section presents a selected subset of the conducted tests with a BESS-dominant resource composition. The propagation gains are set to $K_{\text{fp}} = 17.5$ and $K_{\text{vp}} = 0.08$, while the penetration percentage is varied from 0 % to 10 % and as before both directions of frequency disturbances are considered. The test case parameters and results are summarized in Table 5.7.

The test cases introduced in Table 5.7 are visualized in Fig. 5.23, which displays the results for both negative (left column) and positive (right column) frequency disturbances. The metric distribution is kept consistent with previous figures, where the top row (Fig. 5.23a and Fig. 5.23b) illustrates the primary frequency f_1 response, the second row (Fig. 5.23e and Fig. 5.23f) shows the secondary frequency f_2, the third row (Fig. 5.23c and Fig. 5.23d) presents the voltage magnitude v_2, and the bottom row (Fig. 5.23g and Fig. 5.23h) displays the active power response P_{sup}. Each subplot compares the unsupported base case (red dashed) with the combined frequency and voltage propagation cases (yellow shades) for penetration percentages of 1 %, 5 %, and 10 %. The yellow shades range from light yellow (1 %) to brown (10 %).

The results in Fig. 5.23 demonstrate the effectiveness of the combined frequency and voltage propagation approach in mitigating frequency deviations in the primary grid. After the previous analysis with the isolated control concept an improvement when combining both methods is expected, but the magnitude of the improvement is startling. The nadir reduction for the α_{pen}=1 % case (light yellow) reaches up to 55.5 % for the negative disturbance and 51.9 % for the positive

Table 5.7: Test case parameters for closed-loop frequency response experiments with the combined frequency and voltage propagation methods for varying penetrations levels (α_{pen}).

Case No.	α_{pen}	Nadir f_1	Δ Nadir	RoCoF (Hz/s)	Δ RoCoF
Base Case	0.0 %	49.85 Hz	0.0 %	-0.20 Hz/s	0.0 %
1	1.0 %	49.93 Hz	55.5 %	-0.10 Hz/s	52.1 %
2	5.0 %	49.96 Hz	76.3 %	-0.03 Hz/s	84.8 %
3	10.0 %	49.97 Hz	82.3 %	-0.02 Hz/s	91.3 %
Base Case	0.0 %	50.15 Hz	0.0 %	0.20 Hz/s	0.0 %
1	1.0 %	50.07 Hz	51.9 %	0.10 Hz/s	42.5 %
2	5.0 %	50.03 Hz	76.4 %	0.03 Hz/s	84.2 %
3	10.0 %	50.02 Hz	83.6 %	0.01 Hz/s	93.7 %

disturbance, with similar numbers for the RoCoF reduction, which is significant for this low level of support capacity. Increasing the penetration percentage to 5 % (yellow) and 10 % (brown) further mitigates the frequency disturbance to the degree that it might not actually be seen as a significant disturbance anymore. The nadir reductions reach up to 76.3 % and 82.3 % for the negative disturbance, which leads to absolute frequency values of 49.96 Hz and 49.97 Hz, respectively, a value quite regularly experienced in normal grid operation [136]. With the significantly mitigated frequency deviations the active power responses P_{sup} in Fig. 5.23g and Fig. 5.23h also show a significant reduction in their response magnitudes. This is due to the closed-loop nature, in which the active power response is directly linked to the frequency deviation through the propagation mechanisms. Most importantly, as frequency deviation is minimized, the required active power adjustment also decreases which leads to a more efficient response without unnecessary excessive power swings.

5.4.4 Active Power Flow Control Comparison between Frequency Droop, Voltage Dependency and the combined Method - Closed-loop

To put the previously presented closed-loop results into perspective, the following section compares the three active power flow control methods: frequency droop, voltage dependency, and the combined approach. The cases selected for presentation are based on previously chosen parameters, a BESS-dominant resource composition, with a penetration percentage of $\alpha_{\text{pen}} = 1.0\,\%$ for all methods.

In the selected over-frequency disturbance case ($P_{\text{dist}} = +1.8\,\%$) illustrated in Fig. 5.24, the differences between the three methods are clearly distinguishable. Both the frequency droop method (blue) and the voltage dependency method (green) demonstrate similar performance in terms of nadir and RoCoF reduction, as seen in Fig. 5.24a and Table 5.8. The RoCoF improvement of the frequency droop based method is slightly better than the voltage dependent method, with 10.4 % compared to 8.7 %, while the active power support is sustained for a period of $\sim$2 s before returning to the pre-disturbance level. The voltage dependent method shows a typical droop control behavior with sustained active power support, due to the steady-state frequency deviation. This is reflected in the active power response P_{sup} in Fig. 5.24b. The fact that the frequency f_1 is not significantly different after the 2 s is the result of the low penetration percentage of 1.0 %, which limits the overall impact of the support functionalities. After a sufficiently long time, the generator model of the SMM will provide the major part of the primary frequency response, leading to a similar steady-state frequency value for all methods eventually.

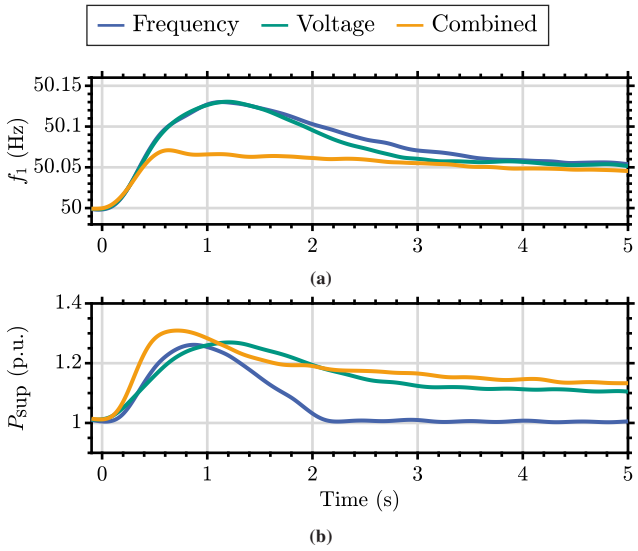

Figure 5.24: Closed-loop comparison of frequency propagation methods for a positive frequency disturbance, showing the MV frequency response f_1 in (a) and the active power response P_{sup} in (b). The three methods compared are the frequency droop (blue), voltage dependency (green), and the combined approach (yellow).

Nonetheless, in the short term the combined method (yellow) outperforms both individual methods significantly in terms of nadir and RoCoF reduction, achieving a nadir reduction of 49.3 % and a RoCoF reduction of 47.3 %. The active power response P_{sup} in Fig. 5.24b reflects the combined contribution of both control mechanisms, resulting in a more substantial and sustained active power support compared to the individual methods. This in turn leads to a faster frequency disturbance mitigation in the primary grid (f_1), which subsequently reduces the propagated frequency deviation used for f_2 and v_2 set point adjustments amplifying the overall efficiency of the response.

Table 5.8: Performance comparison of closed-loop frequency response methods showing RoCoF, nadir, and active power contribution for frequency-only, voltage-only, and combined approaches.

Method	K_{fp}	K_{vp}	α_{pen}	Nadir (Hz)	Δ Nadir (%)	RoCoF (Hz/s)	Δ RoCoF (%)
Frequency	15	0.00	1.0	50.130	12.8	0.170	10.4
Voltage	0	0.08	1.0	50.130	12.5	0.173	8.7
Combined	15	0.08	1.0	50.076	49.3	0.100	47.3

5.5 Conclusion of the Active Power Control and Frequency Response Capability Testing

This chapter investigated the potential of an ASG, established with a B2B systems, to provide FFR services through a novel frequency propagation concept. The experimental validation using a dual PHIL setup demonstrated that the ASG can effectively exploit downstream distribution grid flexibility to control the active power flow and support the primary grid frequency. The frequency propagation concept leverages two mechanisms: the amplification of primary-side frequency deviations to activate droop characteristics of grid-code compliant DG units, and the manipulation of downstream voltage magnitude to influence voltage-sensitive loads.

5.5.1 Key Experimental Findings

Novel Frequency Propagation Mechanism. The PHIL tests validated autonomous active power flow control without direct communication between grid operators, ASG or the downstream DG units. The concept exploits frequency-droop characteristics of grid-code compliant distributed generators (VDE AR-N 4105 with a $\pm$200 mHz deadband) and voltage sensitivities of passive loads. Key features include:

- The active power flow control is a power electronics-enabled solution otherwise not be possible with traditional synchronous connections (e.g., LFT).
- Autonomous control based solely on local frequency (f_1, f_2) and voltage (v_2) measurements.
- ASG system uses amplified frequency disturbances to aggregate downstream DG units.

Performance Results. System-level impact analysis was conducted using a high-level power system single-machine model. The analysis was performed for the three different propagation mechanisms, frequency droop exploit, voltage dependent exploit, combined method. Each method was evaluated with parameter variations within the control of the ASG and the available active power capacity. An asymmetric frequency response of the ASG can be observed for the frequency droop exploitation due to differing droop gains and capabilities of BESS and PV. The quantitative analysis for a high penetration scenario of α_{pen} = 10 %, in a BESS dominant test case showed improvements as follows:

- Frequency droop exploit: up to 46 % nadir reduction, 61 % RoCoF improvement.
- Voltage dependent exploit: up to 63 % nadir reduction, 63 % RoCoF improvement.

- Combined method: up to 83 % nadir reduction, 93 % RoCoF improvement.

5.5.2 Critical Barriers and Implementation Challenges

Technical Implementation Gaps. The roll-out of the ASG deploying a frequency propagation concept at scale faces several technical challenges, including:

- Accurate power flexibility estimation needs a robust real-time capable load sensitivity identification method.
- Analysis for parallel ASG operation, and their interaction with each other.
- Actual grid-code compliance of DG units under propagated frequency/voltage conditions, needs to be investigated and validated.
- Reliability and protection schemes for ASG downstream grids are still under-development.

Market Structure Limitations - Central Europe. On top of the technical challenges, current regulation frameworks prohibit the participation of ASGs in many FFR markets, particularly in Central Europe. This is due to the following reasons:

- ENTSO-E FCR market requires 1 MW minimum bid for 4-hour time slots, with no remuneration for millisecond-timescale response.
- Large fleet of grid-code compliant DG units remain dormant under normal conditions ($\pm$ 200 mHz deadband).
- Service gap exists between inertial response and primary FCR services.

5.5.3 Concluding Remarks

This chapter provides experimental evidence that ASGs can be valuable FFR assets enabling active power flow control to and from downstream grids, without direct communication. The technical feasibility is proven, and the path forward depends on regulatory evolution and market innovation to unlock this untapped flexibility resource. Transitioning from laboratory validation to grid-scale implementation requires advancements in:

- Standardized grid-code requirements for ASGs, e.g., SSTs.
- Robust market ready power electronic products to establish ASGs.

- Market structures recognizing sub-second response capabilities.

The next chapter is based on the technical findings presented here and explores the economic viability of ASGs providing FFR services in a North American market.

6 Economic Analysis of Asynchronous Grid Connections offering FFR Services

With the technical feasibility demonstrated in the previous chapters, the market participation potential of the ASG technology in frequency response services is investigated in the following. By evaluating the economic feasibility of the ASG technology in a frequency response market this chapter addresses *Research Question 4 (RQ4)*. The market framework identification, long-term simulation model development, and comprehensive economic analysis presented in the following constitute the *Key Contributions KC7, KC8,* and *KC9*. These steps will demonstrate the economic viability through year-long simulations and robust sensitivity analysis.

The analysis focuses on revenue stream identification and explores the deployment of the ASG in North America, specifically within the PJM market. As a Regional Transmission Organization (RTO) in the United States, PJM operates an electric transmission system across 13 states within the Eastern Interconnection grid. The introduction of the previous chapter highlighted the state-of-the-art frequency response/control levels currently employed in modern power systems. It is also mentioned that the Central European system operators, as of today, do not offer a market for dynamic FFR services, that remunerate distributed resources on a pay-for-performance basis. The only available FFR service in Central Europe is the FCR service operating with a day-ahead bidding scheme. In this scheme, participants have to offer their capacity a day in advance for windows of 4 hours, thereby ruling out any resources that may experience fluctuating availability. Which is why the choice for the revenue stream analysis fell on a more dynamic market, the PJM *RegD* frequency regulation market.

Parts of this chapter are reproduced from

F. Wald, A. Sajadi, B. Mather, and G. De Carne, "Asynchronous Grid Connections Providing Fast-Frequency Response: System Integration Study," *IEEE Transactions on Power Delivery*, Accepted in Jan. 2026.

To enable the physical aggregation of DG units, the ASG in this scenario is assumed to supply a distribution grid with DG units obeying the German grid connection standard VDE-AR-N 4105 [75].

This combination of North American market framework and German grid connection standard, eliminates the need for additional communication infrastructure or complex control hierarchies typically required to aggregate DG units and enable profitable frequency response service participation.

6.1 PJM FFR Regulation Market - RegA/D

PJM operates a real-time ancillary service market, in which the frequency regulation service is based on an Automatic Generation Control (AGC) concept, sending regulation signals to participating units, to help maintain a balanced system. The signals for frequency regulation are divided into two signals, *RegA* and *RegD*. Where *RegA* represents a low-pass filtered Area Control Error (ACE) signal for traditionally slow-acting resources and *RegD* is the high-pass filtered ACE signal designed for fast response resources, e.g., ESSs.

Fig. 6.1 shows a generalized block diagram of the PJM regulation concept for the *RegD* service. The measurements for voltage and frequency are collected from different locations in the grid and eventually lead to the estimation of the ACE within the area of control. Subsequently, the estimated error is used as a metric in the AGC to dispatch regulation signals to the participating units. The overall regulation needed is split up among the participating and available units, based on their offered regulation capacity, represented in the diagram by Unit 1 to Unit n. On the power system level this is where the loop is closed, the units contribute to the overall power system balance by adjusting their active power output based on the received *RegD* signal and thereby help to mitigate load changes such as ΔP_L.

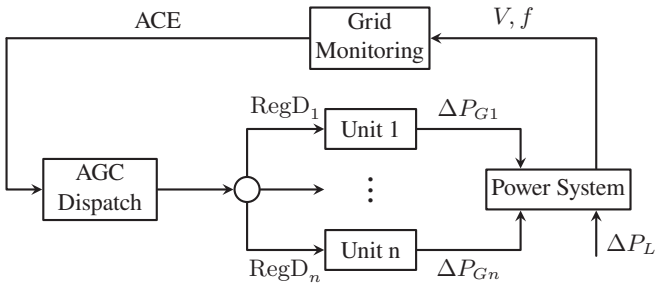

Figure 6.1: Generalized block diagram of PJM's *RegD* frequency regulation concept.

Given the fast acting nature of the proposed ASG concept, the case study investigates the ASG participation in the fast *RegD* service. PJM sends the *RegD* signal in intervals of 2 seconds to participating systems, with normalized values of -1 to 1. This normalized value can then be used to adjust the active power output of the resource according to the offered regulation capacity.

Exemplary data of both the fast *RegD* and slow *RegA* regulation signals is displayed in Fig. 6.2. One can see that both signals trend in the same direction, but it is evident that the *RegD* signal has a significantly higher variability compared to *RegA*, and therefore provokes a more dynamic response from the participating unit.

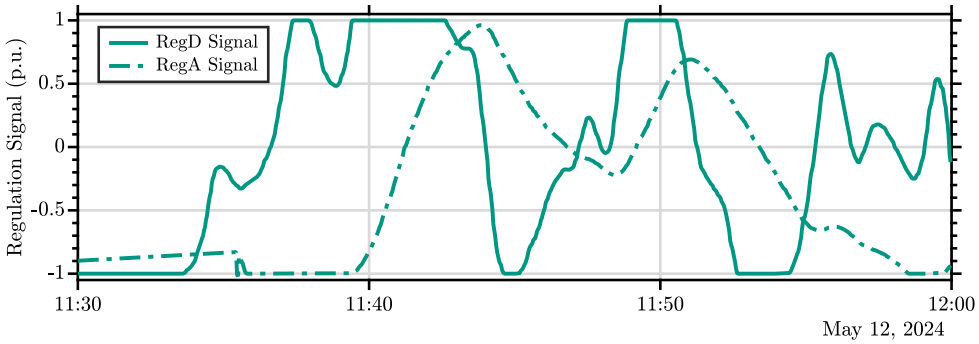

Figure 6.2: Example time series of PJM's fast *RegD* and slow *RegA* signal over a 30-minute window.

6.1.1 PJM RegD Revenue Calculation

PJM's frequency response service compensation follows a pay-for-performance model, aligned with FERC Order No. 755. Compensation depends not only on regulated active power volume but also on signal adherence precision [137]. The performance evaluation combines actual integrated power regulation (capability or mileage, M_{RegD}) with performance score (ρ) to determine five-minute remuneration credits. PJM offers all the data needed to demonstrate and simulate a potential participation freely accessible online which also includes excel tools to calculate the performance score ρ, high resolution historic regulation signals (*RegD*/*RegA*), and clearing prices [128]. The credit calculation uses a so-called mileage (M_{RegD}) as a measure of provided regulation capacity and the mileage ratio β_t^M defined as:

$$\beta_{\mathrm{t}}^{\mathrm{M}} = \frac{M_{RegD}}{M_{RegA}} \tag{6.1}$$

where M_{RegD} is the integrated movement of the regulation control signal, as shown below for *RegD*:

$$M_{RegD} = \sum_{i=1}^{N} |RegD_i - RegD_{i-1}| \tag{6.2}$$

where N=150 is the number of 2-second samples in the 5-minute evaluation window.

This calculation process subsequently yields the regulation credit (C_{reg}) for a 5 minute window, based on the following equations:

$$C_{\text{reg}} = M_{RegD} \cdot \rho \cdot (\lambda_{\text{C}} + \beta_{\text{t}}^{\text{M}} \cdot \lambda_{\text{P}}) \tag{6.3}$$

with the *Regulation Capability Clearing Price* as λ_{C} (in \$/ MW), M_{RegD} (in MW) integrated regulation within the time window and the *Regulation Performance Clearing Price* represented by λ_{P} (in \$/Δ MW).

For the analysis below, both clearing prices are sourced from the historic data during the investigated time period. The freely accessible database in PJM's open data miner interface, provides the full 5-minute resolution clearing prices [128, 138]. In the following a study period of one year is chosen (09/23-08/24) and the prices ranged from 0 to \$238.5/ MW for λ_{C} and from 0 to \$2.8/Δ MW for λ_{P}, with average values of \$2.2/ MW and \$0.08/Δ MW respectively.

6.2 Asynchronous Grid Implementation in PJM

Participation in PJM's *RegD* service requires adapting the previously described ASG control structure. From a high-level perspective as illustrated in Fig. 6.1, the overall regulation concept is a closed-loop control. On the ASG level the control loop is reacting to a set point adjustment of the nominal frequency, based on the *RegD* signal, not directly mitigating any frequency error.

As displayed in Fig. 6.2, the *RegD* signal is a normalized value between -1 and 1, representing the full range of the offered regulation capacity. Full range of the offered capacity means that a participating unit estimates the available active power margin it is able to control and thus reliably offer as regulation capacity.

An example: A unit offering 100 kW of regulation capacity would need to adjust its active power output by +100 kW when receiving a *RegD* signal of 1, and -100 kW when receiving a *RegD* signal of -1. Translated to the ASG control structure investigated in the previous chapter the LV grid frequency (f_2) set point ω needs to be adjusted accordingly. The PHIL tests showed possible active power margins of up to 20 % of the available DG capacity without violating any

grid connection standards. Thus, when extrapolating this to an ASG that supplies a distribution grid in which 2 MW of active power is supplied by DG units and paired with a more conservative active power flexibility margin of 10 %, a regulation capacity of 200 kW could be offered.

6.2.1 VSM Enhancement to Exploit the Frequency Droop

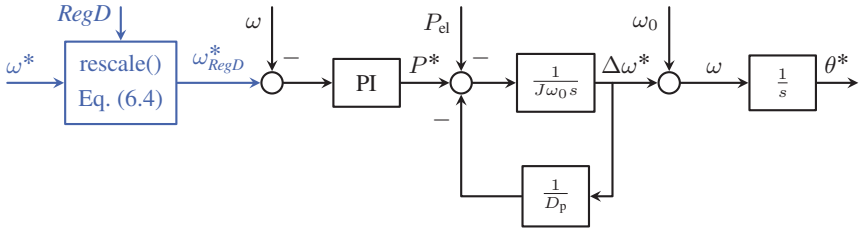

Figure 6.3: VSM enhancement for PJM *RegD* participation by adjusting the frequency set point based on the *RegD* signal.

To adapt the previously introduced control loops a modification of the downstream frequency set point is proposed as illustrated in Fig. 6.3. The adjustment of the frequency set point ω^* is now directly influenced by the received *RegD* signal from the AGC system within PJM. Modifying the set point to ω^*_{RegD} will provoke a droop control reaction from the DG units connected to the LV system. Because of the normalized values received from the AGC, a rescaling of the ω^* set point based on the *RegD* signal is necessary. The rescaling operation is outlined in Eq. (6.4) resulting in the scaled frequency set point ω^*_{RegD}.

$$\omega^*_{RegD} = \omega^* - \Delta\omega_{\max} \cdot \mathrm{RegD} \tag{6.4}$$

where $\omega^* = 377\,\mathrm{rad/s}$ (60 Hz standard North American frequency) is the nominal set point. We define a conservative maximum allowed frequency deviation of 1 Hz which is an angular velocity of $\Delta\omega_{\max} = 6.28\,\mathrm{rad/s}$, and $\mathrm{RegD} \in [-1, 1]$ is the normalized regulation signal. This linear transformation maps the RegD signal range of $[-1, 1]$ to a set point range of $[370.7, 383.3]\,\mathrm{rad/s}$, centered at the nominal $377\,\mathrm{rad/s}$. The actual set point mapping is reversed, therefore the *RegD* adjustment term is subtracted from the nominal set point, because a positive *RegD* signal indicates that the system requires an additional active power injection. This is achieved by lowering the frequency set point and thus provoking a droop control reaction from the DG units, as introduced by the German standard VDE-AR-N 4105 [75]. At $\mathrm{RegD} = -1$, the set point becomes $\omega^*_{RegD} = 383.3\,\mathrm{rad/s}$, at $\mathrm{RegD} = 0$, it remains at $\omega^*_{RegD} = 377\,\mathrm{rad/s}$, and at $\mathrm{RegD} = 1$, it reaches $\omega^*_{RegD} = 370.7\,\mathrm{rad/s}$.

The resulting set point is then used in the governor control as follows:

$$P^* = (\omega^*_{\text{regD}} - \omega)\left(K_{\text{pgov}} + \frac{K_{\text{igov}}}{s}\right) \tag{6.5}$$

6.2.2 Average RMS Model of an Asynchronous Grid Connection

With the modeling of the ASG on different levels of detail introduced earlier. The economic analysis required a simulation model that carries a low computational burden and allows a long-term simulation of one year within a reasonable time frame, while maintaining sufficient accuracy. To that end an average model of the ASG including a simplified LV distribution grid model is developed in DIgSILENT PowerFactory, as an RMS simulation model. The model still includes the main control loops of the ASG (Governor and VSM) as well as the droop control characteristics of the downstream DG units, but omits the complete modeling of both converters in detail. This still produces valid results, since the active power flow dynamic is much slower than the influence of detailed converter models. The block diagram of the developed model is shown in Fig. 6.4.

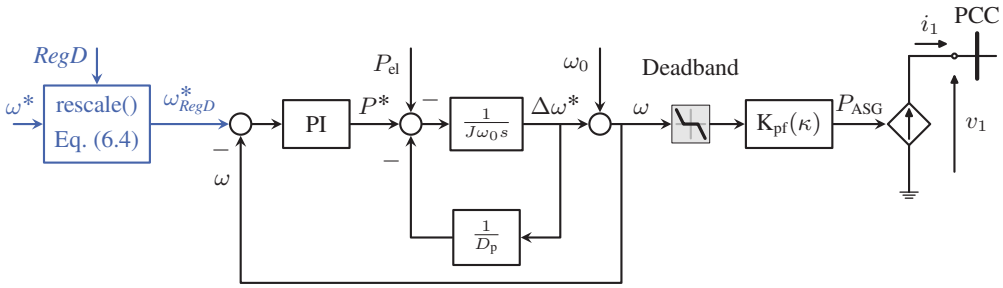

Figure 6.4: Block diagram of the developed average ASG model for long-term simulations in DIgSILENT PowerFactory.

The majority of the components have been introduced before (Fig. 6.3) with the $rescale()$ function (Eq. (6.4) in blue), the governor PI controller and the VSM, from left to right. What is new in this diagram is the simplified representation of downstream DG units, represented by a deadband and droop control block as $\text{K}_{\text{pf}}(\kappa)$. The deadband is set to $\pm$ 200 mHz, following the German grid connection standard VDE-AR-N 4105 [75]. $\text{K}_{\text{pf}}(\kappa)$ represents the frequency-to-active power droop characteristic of the downstream DG units, described as follows:

$$P_{\text{ASG}}(i_{\text{d,q}}) = \begin{cases} \omega \cdot \text{K}_{\text{pf}} \cdot \kappa, & \text{if } |\Delta\omega| \geqslant 200\,\text{mHz} \\ 0 & \text{otherwise} \end{cases} \tag{6.6}$$

where K_{pf} is the droop characteristic defined by the German standard VDE-AR-N 4105 [75]. The parameter κ represents the load composition and subsequently determines the lumped droop gain and capacity of the connected DG units. κ is defined as the ratio between the active power flow in DG units and the ASG capacity. For which the total absolute active power flow of DG units is defined as:

$$P_{\mathrm{DG},\Sigma} = \sum_i |P_{\mathrm{DG},i}| \tag{6.7}$$

where $P_{\mathrm{DG},i}$ represents the active power flow of each individual DG unit. The load composition parameter κ can then be categorized into distinct operational scenarios as follows:

$$\frac{P_{\mathrm{DG},\Sigma}}{P_{\mathrm{ASG}}} = \kappa = \begin{cases} 0 & \text{passive loads only} P_{\mathrm{DG},\Sigma} = 0 \\ (0,1) & 0 < P_{\mathrm{DG},\Sigma} < P_{\mathrm{ASG}} \\ 1 & P_{\mathrm{DG},\Sigma} = P_{\mathrm{ASG}} \\ > 1 & P_{\mathrm{DG},\Sigma} > P_{\mathrm{ASG}} \end{cases} \tag{6.8}$$

where P_{ASG} is the rated capacity of the ASG. It is important to note that $P_{\mathrm{DG},i}$ refers to the absolute active power flow, regardless of whether the DG unit is injecting power into the grid or absorbing power from it. Thus, the ratio κ captures only the available active power capacity from the DG units, not the net active power exchange between the ASG and the distribution grid. This distinction is crucial because this means scenarios where the total absolute active power from DG units ($P_{\mathrm{DG},\Sigma}$) exceed the ASG capacity, i.e., $\kappa > 1$ are possible. That scenario is not only technically possible, but also quite feasible, thus κ may exceed unity by far, given the right balance between the individual DG units and accompanying passive loads. For the following analysis on the other hand, a representative load composition of $\kappa = 0.5$ is selected, consistent with the PHIL test configuration, whereby 50 % of the ASG capacity is available for droop-based control through the aggregated DG units.

In the upcoming analysis the following scenario is considered: An ASG supplying 4 MW to the downstream grid, with $\kappa = 0.5$ means that 2 MW of active power is supplied by DG units and thus available for frequency propagation control. Assuming the previously introduced conservative active power flexibility margin of 10 %, the regulation capacity is, as in the above example, 200 kW.

Circling back to the regulation data as displayed in Fig. 6.2, the active power regulation that results from the *RegD* signal sent to the enhanced ASG model illustrated in Fig. 6.4 is depicted in Fig. 6.5.

It can be observed that the active power regulation (in blue) closely follows the *RegD* signal (in green), but not perfectly. This is a result of the $\pm$ 200 mHz deadband implemented in the DG droop model of Eq. (6.6), as required by the German grid connection standard VDE-AR-N

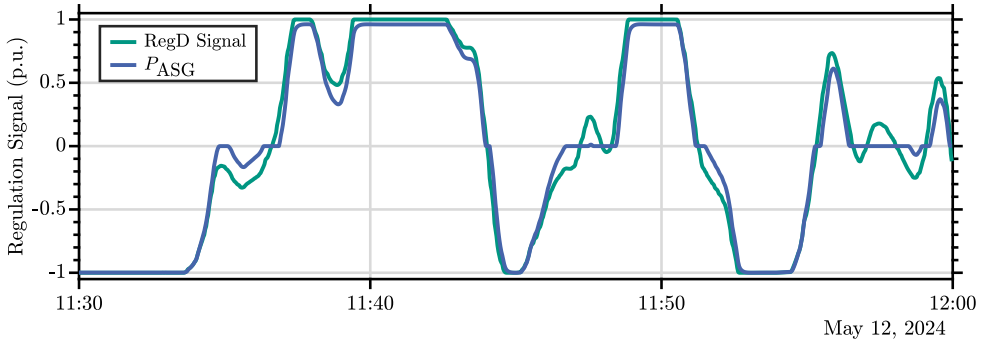

Figure 6.5: Active power response of the enhanced ASG model (in blue) to the PJM *RegD* signal (in green) over a 30-minute window.

4105 [75]. The inaccuracy introduced by that can be further inspected in the magnified plot of Fig. 6.6, which shows a 1-minute window between 11:59 and 12:00 of the previous plot in more detail.

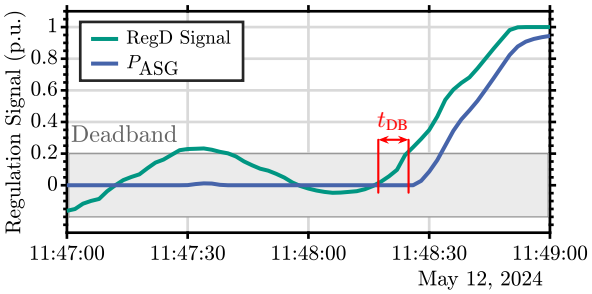

Figure 6.6: Magnified active power response of the enhanced ASG model (in blue) to the PJM *RegD* signal (in green) over a 1-minute window. The red lines and t_{DB} mark the response delay due to the deadband shaded in the gray area.

In red the delayed reaction of the ASG's active power regulation to the *RegD* signal is highlighted and denoted with t_{DB}. The delay here is $t_{DB} = 10\,s$, but that may vary depending on the gradient of the regulation signal. This delay affects the tracking accuracy and leads to a reduced performance score ρ when evaluating the regulation performance according to PJM's methodology.

6.3 Revenue Calculation

The recorded active power response of the enhanced ASG model is now used to calculate the potential revenue when participating in PJM's *RegD* service. This requires the calculation of

the mileage M_{RegD}, the resulting ratio β_t^M and subsequently the regulation credit C_{reg} for each 5-minute window throughout the one-year study period, based on Eqs. (6.1) to (6.3). Sticking with the 2 MW of available DG capacity to control as discussed above, the monthly credit is plotted in the bar chart in Fig. 6.7.

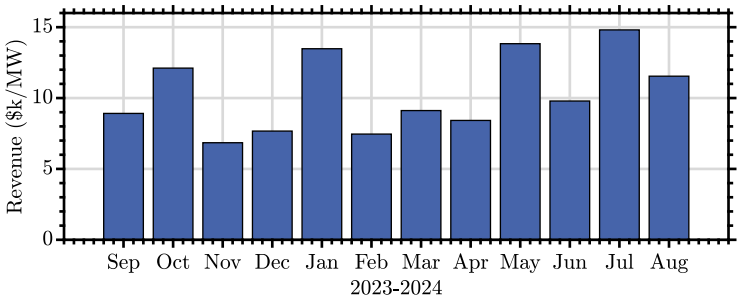

Figure 6.7: Monthly revenue of the enhanced ASG model participating in PJM's *RegD* service with 2 MW of controllable DG capacity over a one-year period.

The results show a monthly revenue ranging from approximately \$6,850/ MW to \$14,800/ MW per month, with an average monthly revenue of ∼\$10,000/ MW. This results in an annual revenue of approximately \$124,000/ MW for the one-year study period.

The same data with focus on the composition of the revenue is shown in Fig. 6.8, where the contribution of the capability price (in light blue) and performance price (in dark blue) to the total revenue is illustrated.

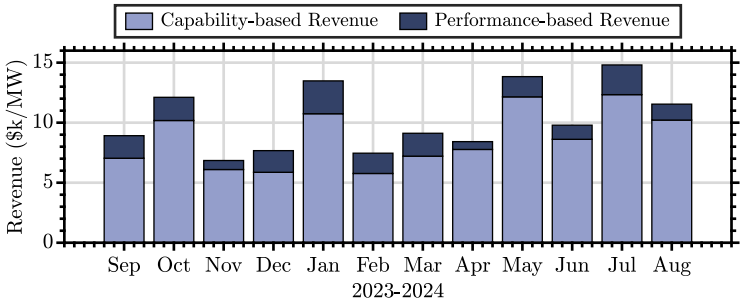

Figure 6.8: Monthly revenue composition of the enhanced ASG model participating in PJM's *RegD* service with 2 MW of controllable DG capacity over a one-year period.

This illustration highlights the significant contribution of the capability-based revenue stream compared to the performance-based revenue. The capability-based revenue term refers to the portion of the total revenue derived from the regulation capability clearing price (λ_{C}) in Eq. (6.3) as marked in the term below:

$$C_{\text{reg,cap}} = M_{RegD} \cdot \rho \cdot (\lambda_{\text{C}}) \tag{6.9}$$

while the performance-based revenue term is calculated from the regulation performance clearing price (λ_{P}) denoted in the following:

$$C_{\text{reg,perf}} = M_{RegD} \cdot \rho \cdot (\beta_{\text{t}}^{\text{M}} \cdot \lambda_{\text{P}}) \tag{6.10}$$

A closer look at the actual revenue calculation formula reveals that both revenue streams are directly proportional to the performance score ρ, which renders the term *performance-based revenue* a bit misleading. But it is still valid due to the fact that the performance clearing price λ_{P} is the basis of this component of the revenue. Nevertheless, the performance rather refers to the mileage ratio β_t^M and the needed *RegD* performance in comparison to the *RegA* signal, than to the specific unit performance itself.

This implicates that the overall revenue is highly dependent the calculated performance score ρ and the actual performed mileage provided by the unit. There is no revenue component that is solely based on the capacity allocated for regulation, even if the regulation is not performed. It is therefore a true pay-for-performance market, in which both revenue components are performance dependent.

6.3.1 Performance Score Impact

Following up the previous discussion on the performance impact on the revenue, a sensitivity analysis is conducted to investigate the influence of different performance scores ρ on the overall revenue. This analysis is performed by scaling the originally calculated performance score of the enhanced ASG model, which is $\rho = 0.76$, to factors of 0.5 and 0.9. It has to be noted that this scaling is only based on post-processing of the recorded mileage data, not on changing the actual control performance of the ASG model. To reflect a system with improved or degraded performance, not only the performance score ρ is changed, but also the recorded mileage M_{RegD} and mileage ratio $\beta_{\text{t}}^{\text{M}}$ is scaled accordingly. The resulting monthly revenue for the three different performance score scenarios is plotted in the bar chart below in Fig. 6.9.

The data shows a significant impact of the performance score on the overall revenue. Scaling the performance score to a value of $\rho = 0.6$ leads to a reduction of the yearly revenue of $\sim$\$94,500/ MW which is a reduction of $\sim$20 %. On the other hand, increasing the performance score to $\rho = 0.9$ leads to an increased yearly revenue of $\sim$\$151,000/ MW, which is an increase of $\sim$21 %. The result highlights the importance of an accurate and fast tracking of the units'

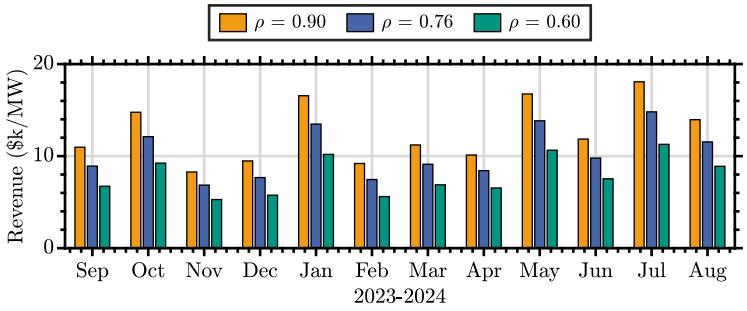

Figure 6.9: Impact of performance score (ρ) variations on the revenue for a 2 MW ASG participating in PJM's *RegD* service.

regulation to the *RegD* signal, this approximation shows a nearly linear relationship between performance score and revenue.

6.4 Economic Projection

The revenue calculation presents the possible short-term income of the ASG when participating in PJM's *RegD* service. For a sound analysis of the overall economic viability of the presented ASG concept, a long-term financial evaluation is necessary. This is done by taking into account the following financial metrics:

1. **Net Present Value (NPV):** The NPV is generally used as an indicator of profitability of an investment over a defined investment horizon. It considers future income and expenditures, while discounting their value back to the present day on the basis of a given discount rate.

2. **Internal Rate of Return (IRR):** The IRR reflects the efficiency of a potential investment. It is defined as the growth rate that is needed to make the NPV equal to zero throughout the given investment horizon.

3. **Cashflow (Cf):** The cashflow simply represents the net amount of cash that is being generated or consumed by the investment in a specific period. It is used in the previous two metrics and can provide insights such as a break even point, but on its own provides limited information.

Ahead of the long-term economic assessment, some assumptions need to be made regarding the initial investment cost, growth rate of revenue and expenditures, as well as the discount rate.

Discount Rate, Growth Rate and Expenditures. As the initial annual revenue is calculated to ~$124,000/ MW it is assumed to rise with a growth rate of 6% per year. Expenditures will mainly

be operation and maintenance costs (c_{OM}) which are initially assumed to amount to a value of 2% of the initial investment cost I, also increasing at the same 6% rate. The growth and discount rates are subject to a wide variety of events within the global economy, which is why a reliable prediction into the future is impossible. Recommendations by the Inter-American Development Bank have therefore been taking into account during the selection process of the discount and growth rate [139]. The discount rate is aligned with the growth rate to r = 6%.

Investment Cost. Together with the growth rate the initial investment cost is of high importance, but also of high uncertainty as detailed below. Therefore, the chosen base investment cost will later be subject to a sensitivity analysis. Presently, the cost value itself is picked rather conservatively, based on detailed investigations within the CIGRE working group B4.91 on SSTs, the final working group report is currently in the drafting phase. The working group estimates the investment cost for a three-stage SST (see Fig. 2.2) with a power rating of 2 MW to be approximately $338,000, which is $169/ kW. As depicted in Fig. 6.10, the estimate includes a flat 30% margin for manufacturing and R&D overheads, and it includes all components deemed necessary for a grid-connected SST. The components include inductors, cooling, auxiliary systems, containers (for outdoor installation), and the power electronics (displayed as Power Electronic Building Blocks (PEBBs)).

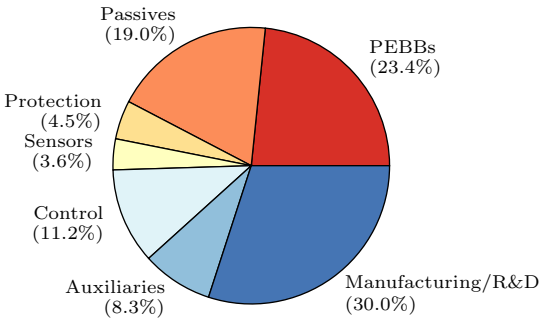

Figure 6.10: Investment cost breakdown for an exemplary three-stage SST of 2 MW power rating, showing the distribution of costs across different component categories, this is based on work from the CIGRE B4.91 working group on SSTs.

It should be mentioned that early reports on SST costs e.g., Huber and Kolar in 2014 estimated the cost per kW to be around $52 [140]. This example does not account for manufacturing overheads and is described to be a mix of third party quotes and rough estimates of material costs of early stage SST prototypes. The authors specifically mention that costs of third party products were much higher than the raw material costs estimated by them, which is why the more recent and detailed CIGRE working group data is used as a basis for this analysis.

6.4.1 Net Present Value Calculation

These estimations and assumptions enable the long-term financial evaluation of the presented ASG concept by calculating the NPV. This serves as a primary indicator of investment profitability over a defined investment horizon, here we choose a period of 15 years. The NPV uses the future cash flow (Cf) which is based on future revenue and expenditures, discounting its value back to the present day to understand whether an investment is worthwhile. A NPV > 0 is considered a positive investment, while a negative NPV indicates a loss. The NPV is calculated based on the following formula:

$$NPV = \sum_{t=0}^{T} \frac{\mathrm{Cf}(t)}{(1+\mathrm{r})^t} \tag{6.11}$$

where T is the total number of periods (years) and r is the discount rate applied to the cash flow (Cf). The above introduced investment cost assumption leads to a positive NPV of ∼$1,538,000/ MW for a 2 MW system over a 15-year investment horizon.

To account for the uncertainty in the investment cost, a sensitivity analysis to potentially increased investment costs I and an increased discount rate is conducted. The range of values for both analysis cover a wide range to also consider extreme scenarios. Fig. 6.11a illustrates the NPV for investment costs ranging from the initial investment cost as assumed above to an investment cost of a factor of five.

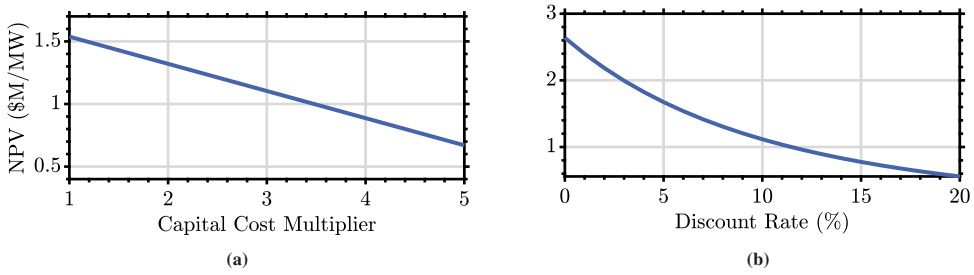

Figure 6.11: Net Present Value (NPV) over a 15-year investment period for a range of increased initial investment costs (1x to 5x base investment cost I) in (a) and a range of discount rates ($r \in [0, 20]\%$) in (b).

The calculation shows that even for very high investments costs of five times the base, which would be approximately $845/ kW or $3.38 million for a 2 MW system, the NPV remains positive at approximately $670,000/ MW. This indicates a robust economic perspective for the presented ASG concept, even under conservative investment cost assumptions. In addition to the investment cost sensitivity, the impact of varying discount rates on the NPV is depicted in Fig. 6.11b. The discount rate is varied from 0 to 20 %, while keeping the initial investment cost at the base value. This analysis reveals that even for very high discount rates of up to 20 %, the NPV remains positive

at approximately \$150,000/ MW. This further underscores the economic robustness of the ASG even in the context of increasing economic uncertainty.

6.4.2 Internal Rate of Return Calculation

In the next step of the long-term economic assessment, the IRR is used as metric to determine boundary conditions of the economic feasibility. The IRR is determined as the discount rate that brings the NPV to zero. In fact the equations for NPV and IRR are closely related, in the sense that the IRR is now set as the unknown discount rate, instead of r and the NPV is set to zero as follows:

$$0 = \sum_{t=0}^{T} \frac{\mathrm{Cf}(t)}{(1 + \mathrm{IRR})^t} \tag{6.12}$$

Then the equation can be solved numerically to estimate the IRR for which the investment breaks even within the defined investment horizon. With this information one can compare different investment opportunities to understand which investment is more profitable at which discount rate.

The IRR over a range of investment costs, as illustrated in Fig. 6.12, emphasizes the economic viability of the ASG. Scaling the investment cost for the ASG in the range of 1 to 5 times the base

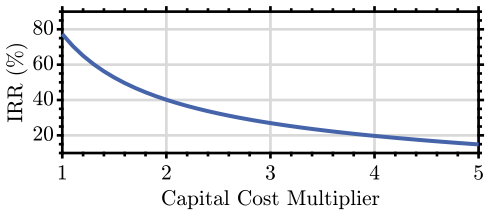

Figure 6.12: Internal Rate of Return (IRR) over a 15-year investment period for a range of increased initial investment costs (1x to 5x base investment cost I).

investment cost always yields a minimum IRR of more than 14%. This underlines the previous statement that the investment remains economically viable even for higher costs of production or material. I.e., even with five-fold investment costs, an interest rate of 14% is required to make the investment more profitable than the ASG, based on the previously made assumptions.

6.4.3 Cashflow Analysis

Both previously introduced metrics are based on the projected future cash flows, starting with the actually simulated first year and calculating the potential future growth (initial revenue is ∼$124,000/ MW). To forecast the potential long-term revenue for the next 15 years the previously discussed revenue growth rate of 6% is applied [139]. The yearly Cf is calculated by subtracting investment cost (I) and operation and maintenance cost (c_{OM}) from the annual revenue ($\Sigma C_{\mathrm{reg}}(t)$), as in:

$$\mathrm{Cf}(t) = \Sigma C_{\mathrm{reg}}(t) - \mathrm{I}(t) - c_{\mathrm{OM}}(t) \tag{6.13}$$

c_{OM} is estimated as a percentage of the capital investment (2 %), increasing with the capital growth rate, and I is only included as a negative cash flow in the first year of the project.

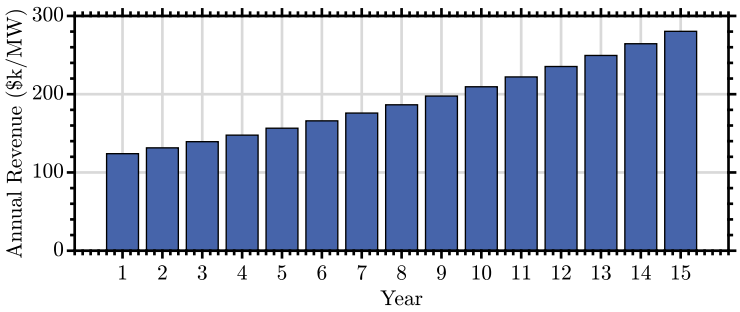

Figure 6.13: Yearly revenue projection over a 15-year investment period, assuming a revenue growth rate of 6% per year.

The resulting revenue per MW increases to up to $280,000 displayed in Fig. 6.13, and is used to calculate the resulting cash flow during that period. The cumulative cash flows illustrated in Fig. 6.14 displays the forecast for the 15-year investment period for different scenarios. The plots illustrate the sensitivity of the cumulative cash flow to the initial investment cost (I) in Fig. 6.14a and the revenue growth rate in Fig. 6.14b. For the variation of investment cost in Fig. 6.14a, the base investment cost of $338,000 for a 2 MW system ($169/ kW) is shaded in the darkest blue, with the increased investment costs (up to $5 \times$ I) shaded in increasingly lighter blue shades. The red arrow indicates the simple linear shift due to the lower negative starting point of the cashflow, that end at $845k/MW for a five-fold scaling. This leads to the delayed break-even point that can be observed for increased investment costs, which is delayed from year 2 to year 7, for the $5 \times$ I.

A similar analysis is conducted for the revenue growth rate in Fig. 6.14b, the lowest case here defined with a growth rate of $r = 3\%$ is again shown in the darkest blue, while the increased growth rates up to 9% are shown in increasingly lighter shades of blue. The difference between the traces here is non-linear, as can be expected for the variation of a factor that impacts the

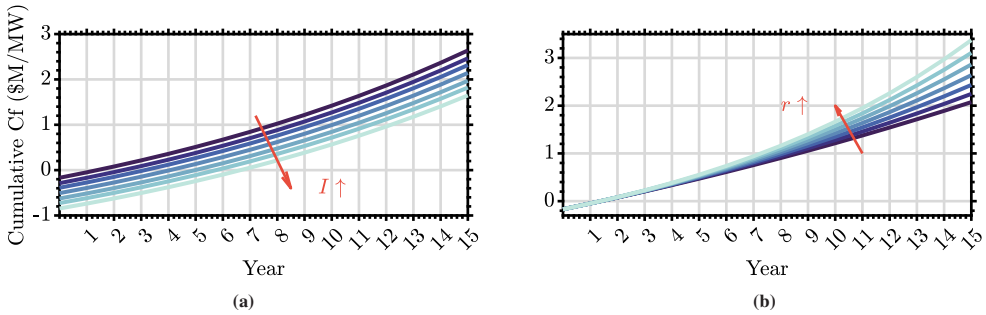

Figure 6.14: (a) Cumulative cash flow projection over a 15-year investment period for a range of increased initial investment costs (1x to 5x base cost, dark to light blue). (b) Cumulative cash flow projection over a 15-year investment period for a range of revenue growth rates (3% to 9%, scaled dark to light blue).

outcome exponentially. In the early years the differences are quite small, and do not influence the break-even point, but the long-term effects are significant. The red arrow highlights the increased slope of the cash flow for higher growth rates which results in a final cash flow of nearly $3.3M for the 9% growth rate, while the 3% growth rate only reaches approximately $2M after 15 years.

6.5 Conclusion and Summary of the Economic Analysis

This chapter investigated the economic viability of the ASG technology providing FFR services within the PJM *RegD* market framework. The core premise for the concept to work and allow revenue generation is the ability to physically aggregate DG units by exploiting their frequency-to-active power droop characteristics and manipulating the frequency set point accordingly. This active power adjustment then leads to the possibility to follow a fast regulation signal such as *RegD* from PJM. The analysis combined two frameworks: the North American market structure of PJM's *RegD* service and the German DG interconnection standard VDE-AR-N 4105. Therefore, this scenario is currently not viable in either market, but serves as a demonstration of the possible power flexibility that is still hidden and could be unlocked with appropriate market frameworks or connection standards.

6.5.1 Key Technical and Economic Findings

Physical Aggregation Implementation. The previously introduced ASG controller has been changed to now utilize the externally provided regulation signal of PJM as a frequency (and

thus active power) set point modifier. This frequency set point modification (ω^*_{regD}), avoids the installation of additional communication infrastructure and allows a very fast aggregation of DG units. The approach is inherently scalable, as regulation capacity grows proportionally with the penetration of grid-code compliant DG units in the distribution network. For the economic analysis a conservative flexibility margin of 10% has been assumed, paired with 2 MW of downstream DG capacity ($\kappa = 0.5$), which results in a net 200 kW of regulation capacity.

Revenue Performance. With said technical implementations a RMS simulation in DIgSILENT PowerFactory has been performed that covered a one-year study period (09/23–08/24), with a resolution of 60 μs. This simulation used real historic data of the regulation signal *RegD* applied within the PJM system. Although, the DG units in the simulation were subject to a $\pm$200 mHz deadband, the recorded simulated active power regulation achieved a performance score of $\rho = 0.76$. With the acquired regulation data and performance score the monthly revenue has been estimated to a range of approximately \$6,850/ MW to \$14,800/ MW, leading to an annual revenue of approximately \$124,000/ MW for the one-year study period. A sensitivity analysis of the performance score impact, in the post-processing workflow of the recorded signals, revealed a linear relation between performance score and revenue, which underlines the claim of PJM to be a true pay-for-performance market.

Long-term Economic Viability. For a sound assessment the annual revenue has been projected over a 15-year investment horizon, taking into account a revenue growth rate of 6% per year and operation and maintenance costs of 2% of the initial investment cost. This projected revenue has subsequently been used to calculate the NPV, IRR and cash flow over the investment horizon. With a base investment cost of \$169/ kW the NPV is approximately \$1,538,000/ MW at a 6% discount rate. This value decreases with higher discount rates and investment cost, but remains positive even for a five-fold increase of investment costs (NPV=\$670k/MW) or a discount rate of 20% (NPV=\$150k/MW). The same sensitivity analysis of investment cost has been performed for the IRR, which has a very high value of 77% for the base investment cost, but is reduced to 14% at the five-folds investment cost increase. These results suggest a very robust business case, that could withstand quite large deviations from the optimal starting conditions.

6.5.2 Challenges and Limitations

Performance Bottlenecks. The performance of the current implementation is still limited by the following factors.

- The aggregated DG units obey a $\pm$200 mHz deadband which leads to reduced tracking accuracy and delays.

- The current controller limits its frequency to a deviation of ± 1 Hz, exceeding this could lead to higher flexibility margins as long as it doesn't interrupt customers or violate grid codes.

Market and Regulatory Frameworks. As highlighted in the introduction to this chapter the analysis conducted here relies on the combination of market frameworks and grid codes with origins from different system operators on different continents. Thus, this exact construct of the ASG physically aggregating DG units and participating in the PJM regulation service is not viable as of today. In Central Europe no FFR market with remuneration windows under 4 hours or a pay-for-performance scheme exists. On the other hand the grid codes within the PJM region do not require DG units to obey an active power-to-frequency droop characteristic, which is a prerequisite for the physical aggregation mechanism to work. Therefore, the performed analysis highlights opportunities for both system operators and standardization entities to utilize the available frequency response capacity and allow small and distributed units to actively participate in the market.

Assumptions and Uncertainties. To put the presented findings in the right context, a couple of key assumptions need to be acknowledged.

- Revenue projections are based on a single year simulation (09/23–08/24), with historical data from PJM and the assumption of a 6% growth rate.
- The investment cost for a SST is estimated to \$169/ kW, the data originates from detailed analysis and discussion with a CIGRE working group. Nevertheless, the estimates are prone to inaccuracies as long as the SST technology matures towards a market ready product.
- The calculated performance score ($\rho = 0.76$) is based on simulation results that, even though an experimental validation has been performed, may diverge in field deployment. Some factors such as heterogeneous DG behavior or dynamic limitation of power electronics due to lifetime management have not been considered in the simulation model.

These assumptions may lead to certain inaccuracies, but the performed sensitivity analysis for different investment costs, performance scores or growth rates allowed a sound assessment. Thus, the economic viability can be judged as robust even for pessimistic values of the previously assumed values.

6.5.3 Concluding Remarks

This economic analysis found compelling arguments to update and improve existing market frameworks and grid connection rules on both sides of the Atlantic. The core emphasizes of this chapter is that a physical aggregation mechanism, e.g., established by the ASG concept via frequency set point manipulation can be economically robust and viable under certain conditions. With the given assumptions a yearly revenue of \$124,000/ MW can be achieved in the first year, with the possibility to rapidly break-even (after 2 years) and exceptional resilience to cost and growth rate variations.

For the successful deployment the following three aspects must converge:

1. **Market structures** that allow service provision (e.g., fast frequency response) with a high granularity and a pay-for-performance model, that rewards accuracy with a resolution in seconds.

2. **Technical infrastructure** must allow high penetration rates of DG, while permitting power electronic systems to work as physical aggregators close to or exceeding substation functionality.

3. **Grid connection rules** that require distributed resources to respond to system events such as over/under voltage or frequency.

The pathways for next steps are multi layered and include potential action items for regulators, system operators and researchers. For the next steps in research it is important to understand and investigate the potential flexibility of DG units in more detail, including the exploitation of voltage-dependent resources. This could lead to more accurate estimations of concrete metrics such as the performance score, but most importantly it might open up other markets with different remuneration schemes. Eventually a prototype could be designed and build to demonstrate the technical feasibility in a field trail over longer time spans with uninterrupted operation and regulation.

7 Conclusion and Vision

7.1 Conclusion

With the emission reduction targets as the main driver of the energy transition, system operators and researchers around the world are striving to accelerate this transition, while upholding a fundamental promise of a technologically advanced society: the uninterrupted availability of energy. This transition bears major technical challenges, such as the spatial and temporal mismatch of generation and consumption or changing control paradigms for power systems with reduced levels of inertia.

The present thesis developed a new control concept built upon advanced power electronic technology capable of establishing an asynchronous grid connection, e.g., Solid-State Transformers. This concept can be one piece of the puzzle to solve power system issues such as frequency volatility by making use of dynamic response capabilities of distributed generation units.

To lay a sound foundation for the thesis the general capability of asynchronous grid connections to offer supportive services and enable future grid operation scenarios have been reviewed. As a result the ability to adapt the active power absorption or injection has been identified as an important and promising service in the face of an inertia and system stability crisis. This led to the above mentioned new control concept called *Frequency Propagation*, effectively resulting in a *Fast-Frequency Response*, it uses the voltage magnitude and/or frequency of the downstream connected distribution system as communication medium. The connected systems either obey a frequency droop characteristics that forces them to adjust the active power based on the locally measured frequency or react to the voltage magnitude based on their inherent nature, e.g., resistive behavior.

To validate the proposed concept, two setups have been developed: a Controller Hardware-in-the-Loop for rapid control development and realistic converter control validation, and a double Power Hardware-in-the-Loop setup to fully test the power electronic converter and control algorithm connected to two emulated power systems. With the use of this validation setup the newly proposed concept demonstrated its capability a) to adapt the active power flow above a margin of

10% around the operating point and b) utilize this to mitigate frequency disturbances occurring in the upstream grid.

In the subsequent analysis a simplified model for RMS simulations has been developed and deployed to execute a long-term (1 year) dynamic simulation of an asynchronous grid connection offering a *Fast-Frequency Response* as a service. The generated simulation data enabled the theoretical deployment of the system in the PJM market framework for frequency response services, allowing the estimation of the revenue by the offered service throughout the year. Based on the revenue estimation an economic assessment for a 15-year investment horizon has been conducted, yielding promising results for operators or investors. The economic viability has been quantified by metrics such as NPV and IRR, concluding that the investment in an asynchronous grid connection under the given assumptions is worthwhile and robust. The economic viability is highlighted by the positive NPV of \$1,538,000/ MW at 6 % discount rate and a six figure (\$124,000/ MW) annual revenue in the first year, which can lead to a break even in year two for investment cost assumptions of \$169/ kVA.

In summary the presented work provides a grid integration study for asynchronous grid connections bridging the gap between power electronic and power system controls. A new control concept, called *Frequency Propagation*, for asynchronous grid connections has been established to adjust its active power flow by aggregating untapped power flexibility potential in the distribution system. The proposed control concept demonstrated the capability to provide frequency response services in a laboratory scale test environment with real power electronic hardware and emulated grids (PHIL). A subsequent revenue stream identification has been performed, conducting long-term simulations and estimating a robust and sound economic perspective when participating in the North American frequency response market of PJM.

7.2 Remaining Challenges

The thesis can be regarded as one of the first attempts to implement an ASG or SST-like technology in a pragmatic scenario, that enables service provision and is accompanied by an economic assessment providing a framework for future business cases development. With the power system evolving and the power electronic technologies for ASGs such as SSTs, or the B2Bs within the power system context, still in a development, a range of questions and challenges remain ahead of a system-wide roll-out.

Thus, the following paragraphs outline some of the challenges and research questions to be addressed in future research endeavors.

Converter Interaction. The high penetration rate of power electronic-based systems can introduce resonances impacting power quality and instabilities. Thus, a rigorous analysis of ASGs operating in parallel to each other is necessary to rule out or mitigate any negative interactions. This includes interaction between multiple ASGs in the same grid, but also with other systems e.g., DG units aggregated by the frequency propagation concept.

Distribution System Protection. A major challenge for the implementation of power electronic-fed subgrids is the protection of the connected devices. This is caused by the fact that traditional protection concepts rely on the power system to supply sufficient short-circuit current in the event of a fault to trigger the respective fuse based on the selective coordination. The necessary short-circuit current can be routed through traditional LFTs, due to their inherent overcurrent capabilities. For power electronic systems this poses a challenge as they do not allow for high over currents and thus the traditional protection with fuses may not work [141]. Solutions for this challenges could be: the collaborative over-current provision by all connected power electronics, if sufficiently available; the redesign of the protection concept, e.g., use of new protection devices such as solid-state circuit breakers; or allocation of a bypass LFT in parallel to the ASG.

Standards for SSTs and DC. The standardization landscape for SSTs remains underdeveloped, with no directly applicable international standard for power system integration. Existing frameworks prove either overly restrictive—such as IEC-62040 for Uninterruptible Power Supplies, designed for small critical loads—or excessively broad, like IEC-62477, which covers generic power electronic converter integration [142, 143]. The proliferation of national regulations for applications like EV charging infrastructure further complicates the development of universal SST solutions. International standardization efforts must progress in coordination with emerging DC resource standards. Critical technical aspects requiring standardization include protection coordination and Basic Insulation Level specifications to prevent unplanned outages [144]. Furthermore, application-specific requirements—such as fault ride-through capabilities for wind farm integration—must be incorporated into standardization frameworks [145, J2].

Power System Scale. In future studies the ASG technology needs to be investigated in large scale power systems, that allow impact assessment on detailed power system stability, interaction with other grid assets and integration in long-term scenarios for planing purposes.

Power Flexibility. One of the most important factors for the proposed control concept is the availability of DG units with inherent or mandated power flexibility. This flexibility needs to be understood in more detail. Do different load compositions influence the overall flexibility and if so, how? Additionally, can the concept work with black box systems downstream, not knowing their power flexibility, and if that is not the case, how can it be estimated reliably? Finally, distribution system models with high degrees of detail and the possibility to define a dynamic

flexibility of single units in conjugation with individual load profiles could provide even more insights in the potential to exploit DG units.

Distributed Generation Participation and Market Design. The potential of DG units for ancillary service provision is immense, but leveraging is first and foremost hindered by a lack of incentives. Therefore, regulation entities and system operators need to re-think their design structure, increasing the emphasis to allow participation of DG units. This can be achieved through multiple pathways, a liberal approach to this would be simply designing a market that offers attractive economic incentives to participants, but also mandating certain behavior during defined grid conditions within the grid connection rules is possible.

7.3 The Vision

Following the control paradigm of asynchronous grid connections, could lead to a clustering of the power system, and towards autonomously operating grid sections, that optimize their local operation while still interacting and exchanging power with adjacent clusters. The voltage and frequency within a cluster is completely decoupled from other clusters and allows the full range of power control exploiting voltage and frequency sensitivities. It allows fast-paced control actions without compromising any privacy or security concerns and make expensive low-latency communication between DG units superfluous. Additionally, clusters may operate a local service and energy market or participate as one large entity in higher level markets. This cluster structure also offers a high degree of power system security, since one unstable or corrupted cluster can be isolated without impacting large parts of the system. Of course this serves first and foremost as a utopia, but may spark ideas for future power system operation and further emphasize the advantages of distributed and decentralized systems, which also applies to power systems.

A Appendix

A.1 Rate of Change of Frequency (RoCoF) Calculation Methodology

The Rate of Change of Frequency (RoCoF) is a critical metric for quantifying the dynamic response of power systems to disturbances. This section details the robust calculation methodology employed throughout this work.

A.1.1 Definition and Significance

The RoCoF quantifies how rapidly the system frequency changes following a disturbance event and is typically expressed in Hz/s or mHz/s. Mathematically, the instantaneous RoCoF at time t is defined as:

$$\text{RoCoF}(t) = \left.\frac{\mathrm{d}f}{\mathrm{d}t}\right|_t \tag{A.1}$$

where $f(t)$ is the system frequency as a function of time. In practice, discrete measurements necessitate a finite-difference approximation:

$$\text{RoCoF}_{\Delta t} = \frac{f(t_0 + \Delta t) - f(t_0)}{\Delta t} \tag{A.2}$$

where t_0 is the disturbance onset time and Δt is the measurement interval. Common measurement intervals in grid codes include 100 ms and 500 ms.

A.1.2 Challenges in Discrete RoCoF Measurement

Direct application of Equation A.2 to measured frequency data presents several challenges:

1. **Measurement noise:** High-resolution frequency measurements ($f_s \approx 20$ kHz in this work) contain sampling noise and quantization effects that can introduce instantaneous spikes.
2. **Filter artifacts:** While low-pass filtering reduces noise, it can introduce phase shifts and edge effects near the disturbance onset.
3. **Temporal uncertainty:** The exact disturbance onset time t_0 is subject to detection threshold sensitivity, introducing uncertainty in the reference point.

These factors can lead to significant variability in single-point RoCoF estimates, particularly for fast transients in low-inertia systems.

A.1.3 Sliding Window Averaging Method

To improve robustness while maintaining temporal resolution, this work employs a *sliding window averaging* approach. Instead of computing a single RoCoF value between two specific time points, multiple RoCoF estimates are calculated across a small temporal window and subsequently averaged.

A.1.3.0.1 Mathematical Formulation For a measurement interval Δt (e.g., 500 ms) and a temporal window of width $\pm\tau$ (typically 10 ms), the robust RoCoF is computed as:

$$\text{RoCoF}_{\Delta t}^{\text{robust}} = \frac{1}{N} \sum_{i=1}^{N} \frac{f(t_0 + \Delta t + \delta_i) - f(t_0 + \delta_i)}{\Delta t + (\delta_i - \delta_i)} \tag{A.3}$$

where:

- $\delta_i \in [-\tau, +\tau]$ are time offsets within the window
- N is the number of offset pairs evaluated
- t_0 is the detected disturbance onset time
- Δt is the target measurement interval

Simplifying Equation A.3, since the time interval remains constant at Δt for all pairs:

$$\text{RoCoF}_{\Delta t}^{\text{robust}} = \frac{1}{N \cdot \Delta t} \sum_{i=1}^{N} [f(t_0 + \Delta t + \delta_i) - f(t_0 + \delta_i)] \tag{A.4}$$

A.1.3.0.2 Discrete Implementation For discrete time-series data with sampling period $T_s = 1/f_s$, the offsets are implemented as sample indices. Let k_0 denote the sample index corresponding to the disturbance onset, and $k_{\Delta t}$ the index at time $t_0 + \Delta t$. The window width in samples is $W = \lfloor \tau \cdot f_s \rceil$. The discrete robust RoCoF is then:

$$\text{RoCoF}_{\Delta t}^{\text{robust}} = \frac{1}{2W+1} \sum_{w=-W}^{+W} \frac{f[k_{\Delta t} + w] - f[k_0 + w]}{t[k_{\Delta t} + w] - t[k_0 + w]} \tag{A.5}$$

where $f[k]$ and $t[k]$ denote the frequency and time values at sample index k, respectively. The denominator is computed for each pair to account for any non-uniform sampling, though with uniform sampling this reduces to a constant Δt.

A.1.3.0.3 Boundary Handling Near the boundaries of the recorded data (beginning or end of measurement), some offsets may fall outside the valid sample range. The implementation includes bounds checking:

$$\text{RoCoF}_{\Delta t}^{\text{robust}} = \frac{1}{N_{\text{valid}}} \sum_{w \in \mathcal{W}_{\text{valid}}} \frac{f[k_{\Delta t} + w] - f[k_0 + w]}{t[k_{\Delta t} + w] - t[k_0 + w]} \tag{A.6}$$

where $\mathcal{W}_{\text{valid}} = \{w : 1 \leqslant k_0 + w \leqslant N_{\text{samples}} \text{ and } 1 \leqslant k_{\Delta t} + w \leqslant N_{\text{samples}}\}$ and $N_{\text{valid}} = |\mathcal{W}_{\text{valid}}|$.

A.1.4 Implementation Parameters

The following parameters are used throughout this work:

Table A.1: RoCoF calculation parameters

Parameter	Symbol	Value
Sampling frequency	f_s	20 kHz
Temporal window width	τ	$\pm$10 ms
Window samples	W	$\pm$200
Number of calculations	$2W + 1$	401
Measurement intervals	Δt	100 ms, 500 ms
Low-pass filter cutoff	f_c	10 Hz
Filter order	n	2 (Butterworth)

A.1.5 Justification and Validation

A.1.5.0.1 Noise Reduction The sliding window approach acts as an additional averaging filter in the time domain. For white measurement noise with variance σ^2, the variance of the averaged RoCoF estimate is reduced by a factor of N_{valid}:

$$\sigma^2_{\text{RoCoF}} = \frac{2\sigma^2}{N_{\text{valid}} \cdot \Delta t^2} \tag{A.7}$$

With $N_{\text{valid}} \approx 401$, this represents a $\sqrt{401} \approx 20$-fold reduction in the standard deviation of the RoCoF estimate compared to a single-point calculation.

A.1.5.0.2 Temporal Resolution While the method averages over a ± 10 ms window, the effective temporal resolution remains adequate for the transients of interest. For typical power system disturbances, frequency variations over 20 ms are much smaller than the overall 500 ms trajectory. The window width ($\tau = 10$ ms) represents only 2% of the 500 ms measurement interval, ensuring the averaged result remains representative of the target time point.

A.1.6 Limitations and Considerations

While the sliding window method provides robust RoCoF estimates, several limitations should be noted:

- **Non-stationary transients:** For highly non-linear frequency trajectories, averaging over 20 ms may slightly smooth rapid variations. This is generally acceptable for the quasi-linear initial RoCoF phase but should be considered for higher-order derivative metrics.
- **Computational cost:** The method requires N_{valid} calculations per metric versus one for single-point methods. At 20 kHz sampling, this adds negligible processing time (< 1 ms per measurement file).
- **Window selection:** The choice of $\tau = 10$ ms is empirically justified but somewhat arbitrary. Sensitivity analysis (not shown) indicates results are stable for $\tau \in [5, 15]$ ms.

A.1.7 Summary

The sliding window averaging method provides robust, reproducible RoCoF estimates suitable for quantitative comparison of control strategies in low-inertia systems. By averaging multiple temporally-adjacent estimates, the method reduces sensitivity to measurement noise and artifacts while maintaining adequate temporal resolution for characterizing fast frequency dynamics. This methodology is applied consistently throughout all experimental results presented in this work.

List of Figures

1.1 Flowchart of the thesis structure aligned with the overall research field and paired with the respective research questions and publications. 11
2.1 ASG concept figure, showing the decoupling between MV (subscript 1) and LV (subscript 2) frequency (f) and voltage magnitude ($\hat{\mathrm{V}}$), with the AC/AC block in the center, representing a power electronic system. Two potential topologies to establish the connection, the SST (left) and B2B (right), are displayed on the left side. 14
2.2 Three-stage SST topology, with a generalized high level control structure. 15
2.3 Three possible topologies for MV converters, with a three-level neutral point clamped converter displayed in a), a MMC in b) and a CHB in c), adopted from [23]. 16
2.4 DAB circuit schematic with magnetic coupling. 17
2.5 Phase shift control of a DAB converter, showing the two voltage levels and the phase shift between the two AC voltages. 18
2.6 Schematics of common LV VSC topologies, with a two-level converter displayed in a), a two-level converter with four legs to connect the neutral conductor in b) and a three-level neutral point clamped converter in c). 19
2.7 B2B topology, with a generalized high level control structure. 20
2.8 Detailed schematic of a two-level VSC. 21
2.9 Carrier-based PWM modulation showing a sinusoidal modulation signal and triangular carrier (upper subplot) with resulting digital PWM switching output (lower subplot). 23
2.10 The *Park* transformation consisting of (a) the *Clark* transformation and (b) the transformation from the stationary $\alpha\beta$ into the rotating dq system. . . . 25
2.11 Detailed view of the AFE control structure, showing the signal routing and cascaded voltage and current controller. 27
2.12 Block diagram of the AFE control structure. 28
2.13 Closed-loop current control. 29
2.14 Closed-loop voltage control. 30
2.15 Bode plot of the open-loop voltage control transfer function, including the remaining phase margin (ϕ_{VC}). 32

2.16 Schematic view of a grid-forming control structure, showing the general signal routing using a VSM algorithm. . . . 34
2.17 Detailed view of the VSM control structure, illustrating the mathematical representation of the active power loop, responsible for the frequency response. . . . 35
2.18 Detailed view of the VSM control structure, illustrating the mathematical representation of the reactive power droop. . . . 35
2.19 Grid-forming current control loop block diagram showing the cascaded PI controller, delays, and plant model. . . . 36
2.20 Grid-forming voltage control loop block diagram showing the outer voltage controller, equivalent current loop delay, and capacitive plant model. . . . 36
3.1 Illustration of an ideal converter model with switches is shown in a) and a diagram of the switching behavior of a semiconductor model is displayed in b). . . . 42
3.2 Conceptual diagram of the ITM interfacing AC and DC circuit models through instantaneous power balance. The current is measured on the AC side and the voltage ratio between both sides is used to calculate the DC-side current source set point. . . . 43
3.3 Average primary side converter model. . . . 44
3.4 Average secondary side converter model. . . . 46
3.5 Block diagram of the single machine model consisting of speed droop, governor and reheat turbine blocks. The model emulates the frequency response of a large synchronous machine connected to a power system [48]. . . . 48
3.6 A simplified CIGRE LV benchmark network with the ASG as the grid interface to the upstream MV grid. An R Load, a BESS and a PV system are connected to the LV grid. The power set point of these systems can be freely controlled during execution. . . . 50
3.7 Generalized CHIL test architecture showing the interface between software model and hardware controller, adopted from [50]. . . . 52
3.8 CHIL setup at EnergyLab, KIT, showing a real-time simulator (green box) connected to an Imperix BoomBox 3.0 controller hardware (red box) through an IO interface (yellow box). . . . 52
3.9 Generalized PHIL test architecture showing the interface between software model and hardware under test, adopted from [50]. . . . 55
3.10 Detailed illustration of the 1 MVA PHIL setup at the EnergyLab, KIT, showing the B2B converter interfaced to power amplifiers controlled by the real-time simulator, adopted from [J1]. . . . 56
3.11 Single machine model interface for the PHIL setup. The model uses the measured active power feed back to calculate the frequency deviation $\Delta\omega$ which is used to generate three-phase voltage references $v^*_{1,abc}$ for the power amplifier. . . . 57

3.12 CIGRE LV benchmark network interface for PHIL setup. The power amplifier replaces the transformer and upstream voltage source, with current measurements i_{abc} fed back to the real-time simulation. 57
3.13 The imperix power converter module *PEB3038* in (a) with the closed modular rack in (b), courtesy of Imperix [51]. 58
3.14 B2B grid connection schematic showing both converters, LC filters (L_G, R_f, C_f), and the primary-side connection panel with circuit breakers and pre-charge circuit. 60
3.15 View of the interior of the EGSTON 200 kVA CSU. From left to right the photos show, the grid connection and isolation transformer in the first cabinet, the active front-end with filters in cabinet 2, in cabinet 3 the six CDA units and the connection panels and breakers in cabinet 4 [52]. 61
4.1 A B2B (top) or SST (bottom) enabling an ASG for increased degrees of freedom in downstream distribution systems. 64
4.2 Demonstration of an unbalanced load scenario showing the unbalanced AC currents on the LV side in (d). The DC voltages with small ripples are shown in (b) and (c), while the nearly untouched and balanced MVAC currents are shown in (a). 65
4.3 A three-stage SST enabling MVDC and LVDC applications, such as EV Fast-Charging, ESSs or PV systems. 67
4.4 DC Power Sharing Concept, for an ASG realized with a three-stage SST with a multi-terminal MVDC link feeding. 68
4.5 DC power sharing control implementation: (a) droop characteristics showing the relationship between DC voltage deviation and power sharing, and (b) block diagram illustrating the control algorithm for calculating DC voltage reference offsets based on the power sharing factor. 68
4.6 Multi-terminal AC/DC SST with DC power sharing control. Left column: LV load step response showing (a) active powers $P_{\mathrm{MV},1}$, $P_{\mathrm{MV},2}$, and $P_{\mathrm{MV,tot}}$, and (c) DC link voltage V_dc. Right column: power sharing shift showing (b) 75%/25% redistribution between converters and (d) stable DC link voltage V_dc. 69
4.7 Active power flow control scheme established with a B2B system, including active resources in the low-voltage distribution network, reacting to voltage ($\hat{V}_2$) and frequency (f_2) adjustments. 72
4.8 Reactive power flow and voltage support scenario offered by a SST. 73
4.9 Visualized history of the SST development and key milestones, based on Table 4.1 [22, 89–92]. 75
4.10 Number of SST projects and companies over time, with a simple first order extrapolation, based on the projects mentioned in Table 4.1, adopted from [J2]. 75

5.1 Timeline of frequency response services showing the activation sequence and duration of different control mechanisms following a frequency disturbance in the power system. The blue dashed frequency trace represents a contingency in a high inertia power system, while the black trace represents a contingency in a low inertia system. 79
5.2 ENTSO-E frequency control services and their respective activation and duration timing showing FCR, aFRR, mFRR, and RR. 80
5.3 Active power to-frequency droop characteristic for newly connected generators in distribution grids, according to VDE AR-N 4105 [75]. 84
5.4 Frequency propagation concept to offer active power flow control for frequency response services, using an ASG (adapted from [J1]). 85
5.5 Enhanced VSM control structure with frequency propagation (in blue) to adapt the frequency (f_2) accordingly. 85
5.6 Enhanced voltage control structure with frequency-to-voltage propagation (in blue) to adapt the voltage (v_2) accordingly. 86
5.7 PHIL setup to test the ASG. The B2B converter is connected to two power amplifiers emulating the primary and secondary side grid respectively, controlled by a real-time simulator. The open-loop test is highlighted by the open switch S_1 (circled in red), which disconnects the feedback of the power flow to the primary grid model. 87
5.8 Illustration of the experimental process: frequency disturbance generation (Step 1), frequency propagation (Steps 2-3), and resulting active power response (Step 4). 87
5.9 Propagation parameter (K_{fp}) variation test case of the B2B in open-loop connection within the proposed PHIL setup, for high shares of BESS. (a) and (b) show the initial frequency (f_1) on the primary side that triggers the frequency response of the LV side with the LV frequency (f_2) in (c) and (d) and the resulting active power flow adjustment in (e) and (f). The left column corresponds to a positive active power disturbance while the right column corresponds to a negative active power disturbance. 90
5.10 Propagation parameter (K_{fp}) variation test case of the B2B in open-loop connection within the proposed PHIL setup, for high shares of PV. (a) and (b) show the initial frequency (f_1) on the primary side that triggers the frequency response of the LV side with the LV frequency (f_2) in (c) and (d) and the resulting active power flow adjustment in (e) and (f). The left column corresponds to a positive active power disturbance while the right column corresponds to a negative active power disturbance. 91

5.11 Active power response comparison between BESS-dominant (blue, cases 3 and 6) and PV-dominant (red, cases 9 and 12) configurations for negative (left) and positive (right) frequency disturbances with K_{fp} = 15. Top row (a) and (b) shows grid power, middle row (c) and (d) BESS power, bottom row (e) and (f) PV power. 92
5.12 Power deviation comparison between BESS-dominant (top, (a) and (b)) and PV-dominant (bottom, (c) and (d)) configurations for negative (left) and positive (right) frequency disturbances with K_{fp} = 15. 93
5.13 Propagation parameter (K_{vp}) variation test case of the B2B in open-loop connection within the proposed PHIL setup. (a) and (b) show the initial frequency (f_1) on the primary side that triggers the response of the LV side with the voltage magnitude (v_2) in (c) and (d) and the resulting active power flow adjustment in (e) and (f). The left column corresponds to a positive active power disturbance, while the right column corresponds to a negative active power disturbance. 95
5.14 Active power response for a combined voltage and frequency control with a case for negative (left column) and positive (right column) frequency disturbances with K_{fp} = 15 and K_{vp} = 0.1. Top row (a) and (b) shows the primary frequency f_1, 2nd row (c) and (d) secondary frequency f_2, 3rd row display the secondary voltage v_2 in (e) and (f), and the bottom row (g) and (h) the active power P_{sup}. 96
5.15 Comparison of the active power adjustment between the frequency propagation (in blue), the voltage propagation (in green) and the combined voltage and frequency propagation (in yellow) method for both negative (left column) and positive (right column) frequency disturbances with K_{fp} = 15 and K_{vp} = 0.1. Top row (a) and (b) shows the primary frequency f_1, and the bottom row (c) and (d) the active power adjustment P_{sup} for the different control algorithms. 98
5.16 Closed-loop PHIL concept with the B2B in the center and the now closed feedback loop, represented by the closed switch S_1 circled in red. 99
5.17 Illustration of the experimental process: frequency disturbance generation (Step 1), frequency propagation (Steps 2-3), and resulting active power response (Step 4) with the closed feedback loop to the SMM in red. 100
5.18 Closed-loop frequency propagation test results for a BESS-dominant configuration, with varying K_{fp} parameter and negative and positive disturbance (left and right column). The sub figures (a) and (b) show the MV frequency response with and without support (Base Case in red), (c) and (d) show the LV frequency propagation (f_2), (e) and (f) display the active power response. The higher the propagation gain K_{fp}, the darker the shade of the data trace. 102

5.19 Closed-loop frequency propagation test results for a PV-dominant configuration, with varying K_{fp} parameter and negative and positive disturbance (left and right column). The sub figures (a) and (b) show the MV frequency response with and without support (Base Case in red), (c) and (d) show the LV frequency propagation (f_2), (e) and (f) display the active power response. The higher the propagation gain K_{fp}, the darker the shade of the data trace. 103
5.20 Closed-loop frequency nadir surface plot for BESS (a) and PV-dominant (b) configuration with the α_{pen} on the y-axis and the frequency propagation gain K_{fp} on the x-axis. 104
5.21 Closed-loop frequency to voltage propagation test results, with varying K_{vp} parameter and negative and positive disturbance (left and right column). The sub figures (a) and (b) show the MV frequency response with and without support (Base Case in red), (c) and (d) show the LV voltage magnitude (v_2), (e) and (f) display the active power response. The higher the propagation gain K_{vp}, the darker the shade of the data trace. 107
5.22 Closed-loop frequency nadir and RoCoF surface plot for the voltage dependent active power flow control with the penetration percentage α_{pen} on the y-axis and the frequency to voltage propagation gain K_{vp} on the x-axis. 108
5.23 Closed-loop combined voltage and frequency propagation results with a case for negative (left column) and positive (right column) frequency disturbance with different penetration percentages (α_{pen} = 1 %, 5 % and 10 %). Top row (a) and (b) shows the primary frequency f_1, 2nd row (c) and (d) secondary frequency f_2, 3rd row displays the secondary voltage v_2 in (e) and (f), and the bottom row (g) and (h) the active power P_{sup}. 109
5.24 Closed-loop comparison of frequency propagation methods for a positive frequency disturbance, showing the MV frequency response f_1 in (a) and the active power response P_{sup} in (b). The three methods compared are the frequency droop (blue), voltage dependency (green), and the combined approach (yellow). 112
6.1 Generalized block diagram of PJM's *RegD* frequency regulation concept. 118
6.2 Example time series of PJM's fast *RegD* and slow *RegA* signal over a 30-minute window. 119
6.3 VSM enhancement for PJM *RegD* participation by adjusting the frequency set point based on the *RegD* signal. 121
6.4 Block diagram of the developed average ASG model for long-term simulations in DIgSILENT PowerFactory. 122

6.5 Active power response of the enhanced ASG model (in blue) to the PJM *RegD* signal (in green) over a 30-minute window. 124
6.6 Magnified active power response of the enhanced ASG model (in blue) to the PJM *RegD* signal (in green) over a 1-minute window. The red lines and t_{DB} mark the response delay due to the deadband shaded in the gray area. 124
6.7 Monthly revenue of the enhanced ASG model participating in PJM's *RegD* service with 2 MW of controllable DG capacity over a one-year period. . . . 125
6.8 Monthly revenue composition of the enhanced ASG model participating in PJM's *RegD* service with 2 MW of controllable DG capacity over a one-year period. 125
6.9 Impact of performance score (ρ) variations on the revenue for a 2 MW ASG participating in PJM's *RegD* service. 127
6.10 Investment cost breakdown for an exemplary three-stage SST of 2 MW power rating, showing the distribution of costs across different component categories, this is based on work from the CIGRE B4.91 working group on SSTs. 128
6.11 Net Present Value (NPV) over a 15-year investment period for a range of increased initial investment costs (1x to 5x base investment cost I) in (a) and a range of discount rates ($r \in [0, 20]\%$) in (b). 129
6.12 Internal Rate of Return (IRR) over a 15-year investment period for a range of increased initial investment costs (1x to 5x base investment cost I). 130
6.13 Yearly revenue projection over a 15-year investment period, assuming a revenue growth rate of 6% per year. 131
6.14 (a) Cumulative cash flow projection over a 15-year investment period for a range of increased initial investment costs (1x to 5x base cost, dark to light blue). (b) Cumulative cash flow projection over a 15-year investment period for a range of revenue growth rates (3% to 9%, scaled dark to light blue). 132

List of Tables

2.1 Switching states and voltages of a two level VSC. 22
2.2 Primary side parameter. 33
2.3 Grid-forming converter control parameters. 39
3.1 Single machine model parameters. 50
3.2 Primitive impedance matrix (Ω / km) [49]. 51
3.3 Back-to-back converter parameters. 59
3.4 The characteristics of each Egston 200 kVA CSU. 61
4.1 Comprehensive overview of SST development projects and manufacturers, chronologically ordered. 76
5.1 Test case parameters for open-loop frequency response experiments. 89
5.2 Test case parameters for open-loop voltage response experiments. 94
5.3 Closed-loop frequency response test cases with BESS and PV dominance, and varying K_{fp} and α_{pen}. 101
5.4 Combined test case parameters for closed-loop frequency response experiments with varying K_{fp} and α_{pen}, under BESS and PV dominance. 105
5.5 Test case parameters for closed-loop voltage response experiments with varying voltage propagation gains. 106
5.6 Nadir and RoCoF metrics for closed-loop voltage-dependent frequency response experiments across varying K_{vp} and α_{pen}. 108
5.7 Test case parameters for closed-loop frequency response experiments with the combined frequency and voltage propagation methods for varying penetrations levels (α_{pen}). 110
5.8 Performance comparison of closed-loop frequency response methods showing RoCoF, nadir, and active power contribution for frequency-only, voltage-only, and combined approaches. 112
A.1 RoCoF calculation parameters 143

Publications

This doctoral research resulted in the following peer-reviewed publications, incorporated in whole or in part in this thesis. The publications are listed separately as journal articles and conference contributions.

Journal articles

[J1] F. Wald, Q. Tao, and G. De Carne, "Virtual synchronous machine control for asynchronous grid connections," *IEEE Transactions on Power Delivery*, vol. 39, no. 1, pp. 397–406, 2024.

[J2] F. Wald, V. M. Hrishikesan, O. Gomis-Bellmunt, H. Ji, M. Davoudi, A. Bidram, M. Syed, M. Joevski, S. Brüske, C. Kumar, R. P. Alzola, I. Colak, S. Pannala, M. Liserre, and G. De Carne, "Applications and services of solid-state transformers in active distribution networksa critical review," *IEEE Transactions on Smart Grid*, vol. 16, no. 5, pp. 3615–3637, 2025.

[J3] F. Wald, A. Sajadi, B. Mather, and G. D. Carne, "Asynchronous grid connections providing fast-frequency response: System integration study," *IEEE Transactions on Power Delivery*, pp. 1–12, 2026.

Conference contributions

[C1] F. Wald and G. De Carne, "Adaptive virtual synchronous machine control for asynchronous grid connections," in *2023 11th International Conference on Power Electronics and ECCE Asia (ICPE 2023 - ECCE Asia)*, 2023, pp. 991–996.

[C2] J. Yun, F. Wald, R. Langella, L. Rubino, and G. De Carne, "Solid-state transformer modeling for power system integration studies," in *Power Systems Computation Conference 2026, Limassol, Cyprus*, submitted, Abtract accepted.

The following peer-reviewed publications were co-authored by Felix Wald, but not included in this thesis.

Co-authored articles

[Co1] Q. Tao, J. Geis-Schroer, F. Wald, M. Courcelle, M. Langwasser, T. Leibfried, M. Liserre, and G. De Carne, "The potential of frequency-based power control in distribution grids," in *2022 IEEE 13th International Symposium on Power Electronics for Distributed Generation Systems (PEDG)*, 2022, pp. 1–6.

[Co2] G. De Carne, M. Liserre, and F. Wald, "Smart transformer control of the electrical grid," in *Advances in Power System Modelling, Control and Stability Analysis*, Jul. 2024, pp. 451–471.

[Co3] Q. Tao, M. Courcelle, F. Wald, J. Yun, M. Suriyah, T. Leibfried, and G. De Carne, "Beyond 50 hz, unlocking voltage and frequency for more flexible grids," *IET Generation, Transmission & Distribution*, Accepted in May 2026.

[Co4] G. De Carne, G. Lauss, S. D'Arco, S. Srdic, F. Wiegel, G. Buticchi, P. Kotsampopoulos, F. Ashrafidehkordi, F. Wald, K. Schoder, S. Hubschneider, A. Monti, A. Benigni, A. Paspatis, S. Cui, J.-J. Jung, M. Nazir, R. Cox, K. Strunz, V. Hagenmeyer, and J. Enslin, "Power hardware-in-the-loop for electrical systems: From research experience to guidelines for industrial testing," *IEEE Open Journal of Power Electronics*, vol. 7, pp. 822–842, 2026.

Bibliography

[1] Xin Lan and Ralph Keeling, "Trends in CO2 - NOAA global monitoring laboratory," https://gml.noaa.gov/ccgg/trends/data.html.

[2] P. A. Stott, N. Christidis, F. E. L. Otto, Y. Sun, J.-P. Vanderlinden, G. J. van Oldenborgh, R. Vautard, H. von Storch, P. Walton, P. Yiou, and F. W. Zwiers, "Attribution of extreme weather and climate-related events," *WIREs Climate Change*, vol. 7, no. 1, pp. 23–41, 2016.

[3] Adam Barth, "Global Energy Perspective 2025," McKinsey, Tech. Rep., 2025.

[4] "World energy transitions outlook 2023: $1.5^{\circ}\mathrm{C}$ pathway," IRENA, Abu Dhabi, Tech. Rep., 2023.

[5] "Global renewables outlook: Energy transformation 2050," IRENA, Abu Dhabi, Tech. Rep., 2020.

[6] "Annual Energy Outlook 2023," U.S. Energy Information Administration (EIA), Washington, D.C., Tech. Rep., Mar. 2023.

[7] "Power systems in transition," IEA, Paris, Tech. Rep., Apr. 2021.

[8] "Renewables 2023 – analysis," IEA, Paris, Tech. Rep., Jan. 2024.

[9] European Commission, "EU action to address the energy crisis," https://commission.europa.eu/topics/energy/eu-action-address-energy-crisis_en.

[10] ——, "Communication from the commission to the european parliament, the european council, the council, the european economic and social committee and the committee of the regions REPowerEU plan," 2022.

[11] G. Di Bella, M. Flanagan, K. Foda, S. Maslova, A. Pienkowski, M. Stuermer, and F. Toscani, "Natural gas in europe: The potential impact of disruptions to supply," *Energy Economics*, vol. 138, p. 107777, Oct. 2024.

[12] "The future of european energy security," https://www.csis.org/analysis/future-european-energy-security, Oct. 2024.

[13] M. Qu, L. Shen, Z. Zeng, B. Yang, H. Zhong, X. Yang, and X. Lu, "Prolonged wind droughts in a warming climate threaten global wind power security," *Nature Climate Change*, vol. 15, no. 8, pp. 842–849, Aug. 2025.

[14] A. Verdone, M. Panella, E. De Santis, and A. Rizzi, "A review of solar and wind energy forecasting: From single-site to multi-site paradigm," *Applied Energy*, vol. 392, p. 126016, Aug. 2025.

[15] J. A. P. Lopes, F. J. Soares, and P. M. R. Almeida, "Integration of electric vehicles in the electric power system," *Proceedings of the IEEE*, vol. 99, no. 1, pp. 168–183, Jan. 2011.

[16] J. W. Jewett and R. A. Serway, *Physics for Scientists and Engineers with Modern Physics*, 7th ed. Belmont, CA: Thomson, Brooks/Cole, 2008.

[17] ENTSO-E, "Frequency containment reserves," https://www.entsoe.eu/network_codes/eb/fcr/.

[18] D. Fernández-Muñoz, J. I. Pérez-Díaz, I. Guisández, M. Chazarra, and A. Fernández-Espina, "Fast frequency control ancillary services: An international review," *Renewable and Sustainable Energy Reviews*, vol. 120, p. 109662, Mar. 2020.

[19] D. Fernandez-Muñoz, I. Guisandez, J. I. Perez-Diaz, M. Chazarra, A. Femandez-Espina, and F. Burke, "Fast frequency control services in europe," in *2018 15th International Conference on the European Energy Market (EEM)*, Jun. 2018, pp. 1–5.

[20] "RDI Roadmap 2024–2034," ENTSO-E, Tech. Rep., 2024.

[21] ICS Investigation Expert Panel, "Grid Incident in Spain and Portugal on 28 April 2025 - Factual Report," ENTSO-E, Tech. Rep., Oct. 2025.

[22] W. McMurray, "Power converter circuits having a high frequency link," US Patent US3 517 300A, Jun., 1970.

[23] G. De Carne, "Analysis of smart transformer features for electric distribution," Ph.D. dissertation, Christian-Albrechts-Universität zu Kiel, May 2018.

[24] A. Nabae, I. Takahashi, and H. Akagi, "A new neutral-point-clamped PWM inverter," *IEEE Transactions on Industry Applications*, vol. IA-17, no. 5, pp. 518–523, Sep. 1981.

[25] J.-S. Lai and F. Z. Peng, "Multilevel converters-a new breed of power converters," *IEEE Transactions on Industry Applications*, vol. 32, no. 3, pp. 509–517, May 1996.

[26] D. Peftitsis, G. Tolstoy, A. Antonopoulos, J. Rabkowski, J.-K. Lim, M. Bakowski, L. Ängquist, and H.-P. Nee, "High-power modular multilevel converters with SiC jfets," *IEEE Transactions on Power Electronics*, vol. 27, no. 1, pp. 28–36, Jan. 2012.

[27] T. Zhao, G. Wang, S. Bhattacharya, and A. Q. Huang, "Voltage and power balance control for a cascaded h-bridge converter-based solid-state transformer," *IEEE Transactions on Power Electronics*, vol. 28, no. 4, pp. 1523–1532, Apr. 2013.

[28] H. Qin and J. W. Kimball, "Solid-state transformer architecture using AC–AC dual-active-bridge converter," *IEEE Transactions on Industrial Electronics*, vol. 60, no. 9, pp. 3720–3730, Sep. 2013.

[29] S. Shao, L. Chen, Z. Shan, F. Gao, H. Chen, D. Sha, and T. Dragičević, "Modeling and advanced control of dual-active-bridge DC–DC converters: A review," *IEEE Transactions on Power Electronics*, vol. 37, no. 2, pp. 1524–1547, Feb. 2022.

[30] B. Grainger and R. W. De Doncker, Eds., *Medium Voltage DC System Architectures*, ser. IET Energy Engineering Series. IET, 2022, no. 143.

[31] D. Sha and G. Xu, *High-Frequency Isolated Bidirectional Dual Active Bridge DC–DC Converters with Wide Voltage Gain*, ser. CPSS Power Electronics Series. Singapore: Springer, 2019.

[32] S. Inoue and H. Akagi, "A bidirectional isolated DC–DC converter as a core circuit of the next-generation medium-voltage power conversion system," *IEEE Transactions on Power Electronics*, vol. 22, no. 2, pp. 535–542, Mar. 2007.

[33] R. De Doncker, D. Divan, and M. Kheraluwala, "A three-phase soft-switched high-power-density DC/DC converter for high-power applications," *IEEE Transactions on Industry Applications*, vol. 27, no. 1, pp. 63–73, Jan. 1991.

[34] R. Zhang, V. H. Prasad, D. Boroyevich, and F. C. Lee, "Three-dimensional space vector modulation for four-leg voltage-source converters," *IEEE Transactions on Power Electronics*, vol. 17, no. 3, pp. 314–326, Jan. 2002.

[35] J.-H. Kim and S.-K. Sul, "A carrier-based PWM method for three-phase four-leg voltage source converters," *IEEE Transactions on Power Electronics*, vol. 19, no. 1, pp. 66–75, Jan. 2004.

[36] B. Lu and S. K. Sharma, "A literature review of IGBT fault diagnostic and protection methods for power inverters," *IEEE Transactions on Industry Applications*, vol. 45, no. 5, pp. 1770–1777, Sep. 2009.

[37] D. G. Holmes and T. A. Lipo, *Pulse Width Modulation for Power Converters: Principles and Practice*, ser. IEEE Series on Power Engineering. Hoboken, NJ: John Wiley, 2003.

[38] C. J. O'Rourke, M. M. Qasim, M. R. Overlin, and J. L. Kirtley, "A geometric interpretation of reference frames and transformations: Dq0, clarke, and park," *IEEE Transactions on Energy Conversion*, vol. 34, no. 4, pp. 2070–2083, 2019.

[39] A. Yazdani and R. Iravani, *Voltage-Sourced Converters in Power Systems: Modeling, Control, and Applications*. John Wiley & Sons, Jan. 2010.

[40] R. Teodorescu, M. Liserre, and P. Rodríguez, Eds., *Grid Converters for Photovoltaic and Wind Power Systems*. John Wiley & Sons, Jan. 2011.

[41] U. Nuß, *Hochdynamische Regelung Elektrischer Antriebe*, 2nd ed. Berlin Offenbach: VDE Verlag GmbH, 2017.

[42] K. J. Åström and T. Hägglund, *PID Controllers: Theory, Design, and Tuning*, 2nd ed. Research Triangle Park, NC: Instrument Society of America, 1995.

[43] K. Sakimoto, Y. Miura, and T. Ise, "Stabilization of a power system with a distributed generator by a virtual synchronous generator function," in *8th International Conference on Power Electronics - ECCE Asia*, Jan. 2011, pp. 1498–1505.

[44] H.-P. Beck and R. Hesse, "Virtual synchronous machine," in *2007 9th International Conference on Electrical Power Quality and Utilisation*, Oct. 2007, pp. 1–6.

[45] Y. Chen, R. Hesse, D. Turschner, and H.-P. Beck, "Comparison of methods for implementing virtual synchronous machine on inverters," *Renewable Energy and Power Quality Journal*, pp. 734–739, Apr. 2012.

[46] S. D'Arco and J. A. Suul, "Virtual synchronous machines — classification of implementations and analysis of equivalence to droop controllers for microgrids," in *2013 IEEE Grenoble Conference*, Jun. 2013, pp. 1–7.

[47] D. B. Rathnayake, R. Razzaghi, and B. Bahrani, "Generalized virtual synchronous generator control design for renewable power systems," *IEEE Transactions on Sustainable Energy*, vol. 13, no. 2, pp. 1021–1036, Apr. 2022.

[48] N. J. Balu, M. G. Lauby, and P. S. Kundur, Eds., *Power System Stability and Control*. McGraw Hill, Jan. 1994.

[49] K. Strunz, E. Abbasi, R. Fletcher, N. Hatziargyriou, R. Iravani, and G. Joos, "TF C6.04.02: TB 575 – Benchmark systems for network integration of renewable and distributed energy resources," CIGRE, Tech. Rep., Apr. 2014.

[50] IEEE Standards Association, "IEEE SA P2004 - recommended practice for hardware-in-the-loop (HIL) simulation-based testing of electric power apparatus and controls," Aug. 2025.

[51] "Imperix - rapid control prototyping solutions for power electronics," https://imperix.com/, Oct. 2025.

[52] G. Pammer, "P-HIL turtorial key design factors," Oct. 2019.

[53] R. Abe, H. Taoka, and D. McQuilkin, "Digital grid: Communicative electrical grids of the future," *IEEE Transactions on Smart Grid*, vol. 2, no. 2, pp. 399–410, 2011.

[54] S. Parashar, A. Kumar, and S. Bhattacharya, "High power medium voltage converters enabled by high voltage SiC power devices," in *2018 International Power Electronics Conference (IPEC-Niigata 2018 -ECCE Asia)*, May 2018, pp. 3993–4000.

[55] A. Singh, X. Zhu, B. Mather, and F. Gurara, "Grid application and controls development for medium-voltage SiC-based grid interconnects," in *2020 IEEE Energy Conversion Congress and Exposition (ECCE)*, Oct. 2020, pp. 3754–3760.

[56] X. Zhu, A. Singh, and B. Mather, "Grid value investigation of medium-voltage back-to-back converters," in *2021 IEEE Power & Energy Society Innovative Smart Grid Technologies Conference (ISGT)*, Feb. 2021, pp. 1–5.

[57] ——, "Grid value analysis of medium-voltage back-to-back converter on DER hosting enhancement," *IEEE Transactions on Power Delivery*, vol. 38, no. 1, pp. 553–563, Feb. 2023.

[58] G. De Carne, M. Liserre, and F. Wald, "Smart transformer control of the electrical grid," in *Advances in Power System Modelling, Control and Stability Analysis*, Jul. 2024, pp. 451–471.

[59] HS Mittweida, "FlexNet eko," https://www.flexnet-eko.de/.

[60] X. Yu, X. She, X. Zhou, and Alex. Q. Huang, "Power management for DC microgrid enabled by solid-state transformer," *IEEE Transactions on Smart Grid*, vol. 5, no. 2, pp. 954–965, Jan. 2014.

[61] X. She, X. Yu, F. Wang, and A. Q. Huang, "Design and demonstration of a 3.6-kV–120-V/10-kVA solid-state transformer for smart grid application," *IEEE Transactions on Power Electronics*, vol. 29, no. 8, pp. 3982–3996, Jan. 2014.

[62] A. Agrawal, C. S. Nalamati, and R. Gupta, "Hybrid DC–AC zonal microgrid enabled by solid-state transformer and centralized ESD integration," *IEEE Transactions on Industrial Electronics*, vol. 66, no. 11, pp. 9097–9107, 2019.

[63] X. She, A. Q. Huang, S. Lukic, and M. E. Baran, "On integration of solid-state transformer with zonal DC microgrid," *IEEE Transactions on Smart Grid*, vol. 3, no. 2, pp. 975–985, Jan. 2012.

[64] C. Kumar, R. Zhu, G. Buticchi, and M. Liserre, "Sizing and SOC management of a smart-transformer-based energy storage system," *IEEE Transactions on Industrial Electronics*, vol. 65, no. 8, pp. 6709–6718, Aug. 2018.

[65] X. Gao, F. Sossan, K. Christakou, M. Paolone, and M. Liserre, "Concurrent voltage control and dispatch of active distribution networks by means of smart transformer and storage," *IEEE Transactions on Industrial Electronics*, vol. 65, no. 8, pp. 6657–6666, Jan. 2018.

[66] V. M. Hrishikesan, D. Das, C. Kumar, H. B. Gooi, S. Mekhilef, and X. Guo, "Increasing voltage support using smart power converter based energy storage system and load control," *IEEE Transactions on Industrial Electronics*, vol. 68, no. 12, pp. 12 364–12 374, Dec. 2021.

[67] V. Hrishikesan, A. K. Deka, and C. Kumar, "Capacity enhancement of a radial distribution grid using smart transformer," *IEEE Access*, vol. 8, pp. 72 411–72 423, 2020.

[68] C. Zhu, "High-efficiency, medium-voltage input, solid-state, transformer-based 400kW/1000V/400A extreme fast charger for electric vehicles."

[69] R. Zhu, M. Liserre, M. Langwasser, and C. Kumar, "Operation and control of the smart transformer in meshed and hybrid grids: Choosing the appropriate smart transformer control and operation scheme," *IEEE Industrial Electronics Magazine*, vol. 15, no. 1, pp. 43–57, Mar. 2021.

[70] D. Das, V. M. Hrishikesan, C. Kumar, and M. Liserre, "Smart transformer-enabled meshed hybrid distribution grid," *IEEE Transactions on Industrial Electronics*, vol. 68, no. 1, pp. 282–292, Jan. 2021.

[71] C. Kumar, R. Manojkumar, S. Ganguly, and M. Liserre, "Impact of optimal control of distributed generation converters in smart transformer based meshed hybrid distribution network," *IEEE access : practical innovations, open solutions*, vol. 9, pp. 140 268–140 280, 2021.

[72] H. V. M., C. Kumar, and M. Liserre, "An MVDC-based meshed hybrid microgrid enabled using smart transformers," *IEEE Transactions on Industrial Electronics*, vol. 69, no. 4, pp. 3722–3731, 2022.

[73] H. V M and C. Kumar, "Operation of meshed hybrid microgrid during adverse grid conditions with storage integrated smart transformer," *IEEE Open Journal of the Industrial Electronics Society*, vol. 2, pp. 315–325, 2021.

[74] J. Yu, C. Luo, J. Duan, C. Wang, R. Lu, A. Trujillo, C. Li, and W. Li, "Design and validation of a 2MW 10KV medium-voltage solid state transformer," in *2024 IEEE Energy Conversion Congress and Exposition (ECCE)*, Phoenix, AZ, USA, 2024, pp. 1426–1433.

[75] "Generating systems on the low-voltage grid minimum technical requirements for the connection and parallel operation of generation systems on the low-voltage grid," VDE, Standard VDE-AR-N 4105, Nov. 2018.

[76] M. Courcelle, Q. Tao, J. Geis-Schroer, S. Bruno, T. Leibfried, and G. De Carne, "Methods comparison for load sensitivity identification," in *2023 IEEE Belgrade PowerTech*, Jun. 2023, pp. 1–6.

[77] M. Courcelle, Q. Tao, J. Geis-Schroer, T. Leibfried, and G. De Carne, "Perturbation-based load sensitivity identification for solid-state transformer-based load control," *IEEE Transactions on Power Delivery*, pp. 1–12, 2024.

[78] Q. Tao, J. Geis-Schroer, M. Courcelle, T. Leibfried, and G. De Carne, "Investigation of frequency dependency of residential loads in modern power systems: An experimental approach," in *2023 11th International Conference on Power Electronics and ECCE Asia (ICPE 2023 - ECCE Asia)*, May 2023, pp. 329–334.

[79] Q. Tao, M. Courcelle, J. Geis-Schroer, T. Leibfried, and G. De Carne, "Experimental investigation of power-to-voltage sensitivity profiles of residential loads for load management studies," *IEEE Transactions on Power Delivery*, pp. 1–12, 2024.

[80] G. De Carne, G. Buticchi, Z. Zou, and M. Liserre, "Reverse power flow control in a ST-fed distribution grid," *IEEE Transactions on Smart Grid*, vol. 9, no. 4, pp. 3811–3819, Jan. 2018.

[81] Q. Tao, J. Geis-Schroer, F. Wald, M. Courcelle, M. Langwasser, T. Leibfried, M. Liserre, and G. De Carne, "The potential of frequency-based power control in distribution grids," in *2022 IEEE 13th International Symposium on Power Electronics for Distributed Generation Systems (PEDG)*, Jun. 2022, pp. 1–6.

[82] J. Rodrigues, C. Moreira, and J. P. Lopes, "Smart transformers as active interfaces enabling the provision of power-frequency regulation services from distributed resources in hybrid AC/DC grids," *Applied Sciences*, vol. 10, no. 4, p. 1434, Jan. 2020.

[83] J. Chen, M. Liu, G. De Carne, R. Zhu, M. Liserre, F. Milano, and T. O'Donnell, "Impact of smart transformer voltage and frequency support in a high renewable penetration system," *Electric Power Systems Research*, vol. 190, Jan. 2021.

[84] S. Giacomuzzi, M. Langwasser, G. De Carne, G. Buja, and M. Liserre, "Smart transformer-based medium voltage grid support by means of active power control," *CES Transactions on Electrical Machines and Systems*, vol. 4, no. 4, pp. 285–294, Jan. 2020.

[85] G. De Carne, G. Buticchi, M. Liserre, and C. Vournas, "Frequency-based overload control of smart transformers," in *2015 IEEE Eindhoven PowerTech*, Jan. 2015, pp. 1–5.

[86] L. Zheng, A. Marellapudi, V. R. Chowdhury, N. Bilakanti, R. P. Kandula, M. Saeedifard, S. Grijalva, and D. Divan, "Solid-state transformer and hybrid transformer with integrated energy storage in active distribution grids: Technical and economic comparison, dispatch, and control," *IEEE Journal of Emerging and Selected Topics in Power Electronics*, vol. 10, no. 4, pp. 3771–3787, Aug. 2022.

[87] X. Gao, R. Zhu, G. De Carne, and M. Liserre, "Comparison of voltage support services by means of STATCOM and smart transformer in medium voltage grid," in *2018 13th IEEE Conference on Industrial Electronics and Applications (ICEA)*, Wuhan, China, May 2018, pp. 946–951.

[88] D. Shah and M. L. Crow, "Online volt-var control for distribution systems with solid-state transformers," *IEEE Transactions on Power Delivery*, vol. 31, no. 1, pp. 343–350, Feb. 2016.

[89] D. Grider, M. Das, A. Agarwal, J. Palmour, S. Leslie, J. Ostop, R. Raju, M. Schutten, and A. Hefner, "10 kV/120 a SiC DMOSFET half h-bridge power modules for 1 MVA solid state power substation," in *2011 IEEE Electric Ship Technologies Symposium*, 2011, pp. 131–134.

[90] C. Zhao, D. Dujic, A. Mester, J. K. Steinke, M. Weiss, S. Lewdeni-Schmid, T. Chaudhuri, and P. Stefanutti, "Power electronic traction transformer—medium voltage prototype," *IEEE Transactions on Industrial Electronics*, vol. 61, no. 7, pp. 3257–3268, Jul. 2014.

[91] "HypoBatt," https://www.hypobatt.eu, 2024.

[92] T. Gardner, "Google to buy power for AI needs from small modular nuclear reactor company kairos," *Reuters*, Oct. 2024.

[93] M. K. Das, C. Capell, D. E. Grider, S. Leslie, J. Ostop, R. Raju, M. Schutten, J. Nasadoski, and A. Hefner, "10 kV, 120 a SiC half h-bridge power MOSFET modules suitable for high frequency, medium voltage applications," in *2011 IEEE Energy Conversion Congress and Exposition (ECCE)*, 2011, pp. 2689–2692.

[94] "GridBridge," https://grid-bridge.com.

[95] CIRED WG 2019-1, "DC networks on the distribution level – new trend or vision?" 2021.

[96] H.-J. Yun, D.-K. Jeong, H.-S. Kim, M. Kim, J.-W. Baek, J.-Y. Kim, and H.-J. Kim, "Implementation of a single-phase SST for the interface between a 13.2 kV MVAC network and a 750 V bipolar DC distribution," *Electronics*, vol. 7, no. 62, 2018.

[97] "ALigN - Project RWTH Aachen," https://www.isea.rwth-aachen.de/go/id/srwf?#aaaaaaaaaaasrwk.

[98] "Elektromobilität: Aufbau der ladeinfrastruktur nimmt fahrt auf, news article from the city of aachen," https://www.lebendiges-aachen.de/modules.php?name=News&file=article&sid=21019.

[99] SP Energy Networks, "LV engine NIC submission proposal," https://www.spenergynetworks.co.uk/ pages/lv_engine.aspx, 2017.

[100] K. Smith, D. Wang, R. Peña-Alzola, A. Burt, Graeme M.and Kazerooni, and M. Eves, "Approach to assessing the effective integration of solid-state transformers in LV networks," in *CIRED 2020 Berlin Workshop (CIRED 2020)*, vol. 2020, Berlin, Jan. 2020, pp. 182–185.

[101] V. Psaras, R. Peña-Alzola, I. Abdulhadi, G. Burt, A. Kazerooni, F. Shillitoe, M. Eves, and J. Yu, "Protection of lvdc networks integrating smart transformers: The case of lv engine falkirk trial site," in *The 17th International Conference on AC and DC Power Transmission (ACDC)*, 2021, pp. 204–209.

[102] Delta Electronics, "Delta demonstrates 400 kW solid-state transformer-based extreme fast EV charger to partners," https://www.deltaww.com/en-us/news/35766.

[103] FUNDRES, "Future unified dc railway electrification system," https://fundres-project.eu/.

[104] Kopernikus-Projekt ENSURE, "Diese fünf technologien will ENSURE in der praxis testen," https://www.kopernikus-projekte.de/aktuelles/news/ensure_ankuendigung_demonstratoren_ensure_phase_2.

[105] TIGON, "Towards intelligent DC-based hybrid grids optimizing the network performance," https://tigon-project.eu/.

[106] "Solid State Power LLC," https://solidstatepower.net/.

[107] "Resilient Power EV Charging Infrastructure," https://www.resilientpower.com.

[108] A. Anurag, S. Acharya, Y. Prabowo, V. Jakka, and S. Bhattacharya, "Mobile utility support equipment based solid state transformer (MUSE-SST) for MV grid interconnection with gen3 10 kV SiC mosfets," in *2018 IEEE Energy Conversion Congress and Exposition (ECCE)*, 2018, pp. 450–457.

[109] ——, "Design of a medium voltage mobile utilities support equipment based solid state transformer (MUSE-SST) with 10 kV SiC mosfets for grid interconnection," in *2018 9th IEEE International Symposium on Power Electronics for Distributed Generation Systems (PEDG)*, 2018, pp. 1–8.

[110] S. Rupp, G. Burt, U. Schichler, S. Brüske, A. Egea-Àlvarez, and G. Jambrich, "MVDC grids to facilitate the roll out of renewables," in *2023 27th International Conference on Electricity Distribution (CIRED)*, Jun. 2023.

[111] L. Zheng, X. Han, C. Xu, R. P. Kandula, L. Graber, M. Saeedifard, and D. Divan, "7.2 kV three-port SiC single-stage current-source solid-state transformer with 90 kV lightning protection," *IEEE Transactions on Power Electronics*, vol. 37, no. 10, pp. 12 080–12 094, Oct. 2022.

[112] P. Czyz, T. Guillod, F. Krismer, J. Huber, and J. W. Kolar, "Design and experimental analysis of 166 kW medium-voltage medium-frequency air-core transformer for 1:1-dcxapplications," *IEEE Journal of Emerging and Selected Topics in Power Electronics*, vol. 10, no. 4, pp. 3541–3560, Aug. 2022.

[113] P. Czyz, T. Guillod, D. Zhang, F. Krismer, J. Huber, R. Färber, C. M. Franck, and J. W. Kolar, "Analysis of the performance limits of 166 kW/7 kV air- and magnetic-core medium-voltage medium-frequency transformers for 1:1-DCX applications," *IEEE Journal of Emerging and Selected Topics in Power Electronics*, vol. 10, no. 3, pp. 2989–3012, Jun. 2022.

[114] SSTAR, "Innovative HV solid-state TrAnsformer for maximizing renewable energy penetration in energy distribution and transmission systems," https://sstar-project.eu/.

[115] "Super-HEART: A fault-tolerant and highly efficient energy hub with embedded short-term energy storage for high availability electric power delivery," CAU Kiel, Frauenhofer ISIT, Tech. Rep.

[116] "Amperesand - homepage," https://amperesand.io/.

[117] "Charge America | Advanced EV Charging Infrastructure Solutions," https://chargeamerica.us/.

[118] "The DG Matrix Power Router | The World's First Multi-port Solid-state Transformer," https://dgmatrix.com/power-router-technology.

[119] "Novos Power | Grid-Ready for AI Data Centers and Beyond," https://www.novospower.com.

[120] "Alderbuck," https://alderbuck.com/, Aug. 2025.

[121] "DC Grid," https://dcgrid.io/.

[122] "Heron Power | Built for the grid ahead," https://heronpower.com/.

[123] "Hyperscale Power," https://hyperscale-power.com/.

[124] Julia Matevosyan, "Frequency response."

[125] NERC Resources Subcommitte, "Balancing and frequency control," NERC, Tech. Rep., May 2021.

[126] Z. Ali, N. Christofides, L. Hadjidemetriou, E. Kyriakides, Y. Yang, and F. Blaabjerg, "Three-phase phase-locked loop synchronization algorithms for grid-connected renewable energy systems: A review," *Renewable and Sustainable Energy Reviews*, vol. 90, pp. 434–452, Jul. 2018.

[127] "FASS DASSA consultation," EirGrid, Tech. Rep., May 2024.

[128] "PJM - ancillary services," https://www.pjm.com/markets-and-operations/ancillary-services.aspx.

[129] TRANSNET BW, "Regelreserve," https://www.transnetbw.de/en/energy-market/ancillary-services/regelreserve.

[130] "Regelleistung > Grundlagen > Was ist Regelreserve?" https://www.regelleistung.net/de-de/Grundlagen/Was-ist-Regelreserve.

[131] D. P. Stojanović, L. M. Korunović, and J. V. Milanović, "Dynamic load modelling based on measurements in medium voltage distribution network," *Electric Power Systems Research*, vol. 78, no. 2, pp. 228–238, Feb. 2008.

[132] K. Bailey, "CLASS - customer load active system services second tier LCN fund project closedown report," Electricity North West, Tech. Rep., Sep. 2015.

[133] G. De Carne, M. Liserre, and C. Vournas, "On-line load sensitivity identification in LV distribution grids," *IEEE Transactions on Power Systems*, vol. 32, no. 2, pp. 1570–1571, Mar. 2017.

[134] A. Abur and A. G. Expósito, *Power System State Estimation: Theory and Implementation*. Boca Raton: CRC Press, Mar. 2004.

[135] G. De Carne, G. Buticchi, M. Liserre, and C. Vournas, "Load control using sensitivity identification by means of smart transformer," *IEEE Transactions on Smart Grid*, vol. 9, no. 4, pp. 2606–2615, Jan. 2018.

[136] Frauenhofer ISE - Energy Charts, "Measurement of grid voltage and frequency on 28.04.2025 (germany)," https://www.energy-charts.info/charts/frequency/chart.htm?l=en&c=DE&timeslider=1&hour=11&datetimepicker=28.04.2025, Apr. 2025.

[137] "Final rule order no. 755: Frequency regulation compensation in the organized wholesale power markets," Federal Energy Regulatory Commission, Order 137 FERC 61,064, Oct. 2011.

[138] "PJM - data miner 2 - real-time ancillary service market results," https://-dataminer2.pjm.com/feed/reserve_market_results.

[139] J. Campos, T. Serebrisky, and A. Suárez-Alemán, "Time goes by: Recent developments on the theory and practice of the discount rate," Inter-American Development Bank, Tech. Rep., Sep. 2015.

[140] J. E. Huber and J. W. Kolar, "Volume/weight/cost comparison of a 1MVA 10 kV/400 V solid-state against a conventional low-frequency distribution transformer," in *2014 IEEE Energy Conversion Congress and Exposition (ECCE)*, Sep. 2014, pp. 4545–4552.

[141] "Low-voltage fuses," IEC, Standard 60269-1, 2014.

[142] "Uninterruptible power systems (UPS) - part 1: Safety requirements," IEC, Standard 62040-1, 2022.

[143] "Safety requirements for power electronic converter systems and equipment - part 1: General," IEC, Standard 62477-1, 2022.

[144] C. Xu, J. Wei, L. Zheng, X. Han, M. Saeedifard, R. P. Kandula, K. Kandasamy, D. Divan, and L. Graber, "Insulation coordination design for grid-connected solid-state transformers," *IEEE Journal of Emerging and Selected Topics in Power Electronics*, vol. 10, no. 4, pp. 3746–3758, Aug. 2022.

[145] M. Tsili and S. Papathanassiou, "A review of grid code technical requirements for wind farms," *IET Renewable Power Generation*, vol. 3, no. 3, pp. 308–332, Sep. 2009.